`

The Dissertation Committee for Christopher Earl Carlton certifies that this is the approved version of the following dissertation:

DEFECTS AND DEFORMATION IN NANOSTRUCTURED METALS

Committee:

Paulo Ferreira

Desiderio Kovar

Llewellyn Rabenberg

Sheldon Landsberger

Ian Robertson

Miguel-Jose Yacaman

DEFECTS AND DEFORMATION IN NANOSTRUCTURED METALS

By

Christopher Earl Carlton, BS

Dissertation

Presented to the Faculty of the Graduate School of

The University of Texas at Austin

in Partial Fulfillment

of the Requirements

for the Degree of

Doctor of Philosophy

The University of Texas at Austin

December 2009

DEFECTS AND DEFORMATION IN NANOSTRUCTURED METALS

by

Christopher Earl Carlton, PhD

The University of Texas at Austin, 2009

Supervisor: Paulo J. Ferreira

A better understanding of how the nanoscale environment affects the mechanical properties of materials, in particular metallic nanoparticles and nanocrystalline metals is vital to the development of next generation materials. Of special interest is obtaining a fundamental understanding of the inverse Hall-Petch Effect in nanocrystalline metals, and nanoindentation in individual nanoparticles. Understanding these subjects is critical to understanding how the mechanical properties of materials are fundamentally affected by nanoscale dimensions.

These topics have been addressed by a combination of theoretical modeling and *in-situ* nanoindentation transmission electron microscopy (TEM) analysis. Specifically, the study of the inverse Hall-Petch effect in nanocrystalline metals will be investigated by a thorough review of the literature followed by a proposed novel theoretical model that better explains the experimentally observed behavior of nanocrystalline metals. On the other hand, the nanoindentation of individual nanoparticles is a very new research topic

that has yet to aggregate a large body of experimental data. In this context, *in-situ* TEM nanoindentation experiments on silver nanoparticles will be first performed to determine the mechanisms of deformation in these nanostructures. A theoretical explanation for the observed deformation mechanisms will be then developed and its implications will be discussed. In addition to nanoparticles, this study will also provide unique and valuable insight into the deformation mechanisms of nanopillars, a growing area of research despite much controversy and speculation about their actual mechanisms of deformation.

After studying the novel behavior of both nanocrystalline metals and nanoparticles, useful applications of both classes of materials will be explored. The discussion of applications will focus on utilizing the interesting behaviors explored in the dissertation. Of particular interest will be applications of nanoparticles and nanocrystalline materials to coatings, radiation resistance and super-plastic materials.

TABLE OF CONTENTS

CHAPTER 1: INTRODUCTION

1.1 MOTIVATION

Innovations in materials processing and characterization techniques have led to the development of a novel class of materials called nanomaterials; materials with characteristic lengths on the order of nanometers. Different kinds of nanomaterials are currently being investigated for use in a wide range of applications, from fuel cells to drug delivery. To properly understand and appreciate the diversity of nanomaterials, some form of categorization is required. Currently, the most common way to classify nanomaterials is to identify them according to their dimensions. Nanomaterials can be then classified as a) Zero-dimensional (0-D), b) One-dimensional (1-D), c) Two-dimensional (2-D) and d) Three-dimensional (3-D). This classification system is based on the number of dimensions which are not confined to the nanoscale (1-100 nm). The most common 0-D nanomaterials are nanoparticles. Nanowires, nanopillars, nanotubes, nanorods are all 1-D nanomaterials. 2-D and 3-D nanomaterials are somewhat more difficult to classify. For this dissertation, 2-D and 3-D nanomaterials will be defined as solids with macroscopic dimensions in two and three dimensions, respectively, but exhibiting a nanocrystalline grain structure.

While there are still many unanswered questions in the field of nanomaterials, it is clear that reducing the characteristic length of materials to the nanoscale has a significant impact on a material's behavior and properties. Of particular interest to this work is the effect of nanoscale dimensions on the mechanical behavior of materials, as well as how nanoscale dimensions influence the nucleation and motion of crystalline defects. Due to the scope of this dissertation, it is convenient to organize the nanomaterials into two groups. One group contains the 0-D and 1-D nanomaterials; the other contains the 2-D and 3-D nanomaterials. This distinction is convenient because in 0-D and 1-D materials, the free surfaces can be expected to dominate the mechanical properties, while for 2-D and 3-D nanomaterials the deformation will be greatly influenced by the large amount of grain boundaries.

In the case of 0-D and 1-D nanomaterials it has been shown that there is a conspicuous lack of dislocations, regardless of the materials processing history, even after significant deformation and radiation damage [1-5]. However an abundance of twins seems to exist, even in materials with high stacking fault energies (SFE) [6]. Because of these observations, it has been suggested that either dislocations cannot exist in nanoparticles, or that dislocations are unstable in nanoparticles. Additionally, much has been said about the nucleation of deformation twins [7-9] in 3-D nanomaterials, but very little work has been done on mechanical twinning in isolated nanoparticles.

Another interesting phenomenon observed in 0-D and 1-D nanomaterials occurs during mechanical compression testing of metals. In the case of 0-D nanomaterials, no compression experiments, to the author's knowledge, have been performed at the nanoscale. The experiment that has been the closest to the nanoscale was an *in-situ* TEM compression of ~200 nm Si particles [10]. However, the particles tested were too large to extract relevant information for the nanoscale and the mechanical deformation of Si is also expected to be different from that of metals. In the case of 1-D metallic materials, ranging in diameter from hundreds of nanometers to several micrometers, several compression experiments have been conducted *in-situ,* typically in an SEM, although several *in-situ* TEM experiments have been also carried out [11-15]. As the pillar size was decreased, the pillars exhibited increased strength. Additionally, dislocation slip bands could clearly be seen. Attempts to model and understand the mechanisms of deformation in these pillar nanocompression experiments have been made [16-19]. However, it has been difficult to experimentally validate these models due to the limitations of scanning electron microscopy. In fact, even the past *in-situ* TEM defromation experiments were unable to reveal details about the exact mechanisms of deformation, such as dislocation nucleation sites, because large sample sizes and fixed strain rates caused dislocations to move too rapidly to be easily monitored.

To address these aforementioned issues in 0-D and 1-D nanomaterials, this dissertation will first propose two models; one to explain the absence of perfect dislocations and the other to explain the presence of twins in 0-D and 1-D nanostructured metals. In addition, this dissertation will show how the model on the absence of dislocations can be applied to nanopillar compression experiments. This in turn will provide the first insights into the mechanical properties of metallic nanoparticles and it will help explain the enhanced strength of nanopillars.

In 2-D and 3-D materials, the issues are quite different from 0-D and 1-D nanomaterials. Many *in-situ* TEM deformation experiments have been performed [20-26]. The results show a far smaller numbers of mobile dislocations in nanomaterials when compared with conventional materials [20-23]. It is often claimed that the number of dislocations insufficient to accommodate the applied plastic deformation. Another persistent controversy concerning 2-D and 3-D nanomaterials has been the study of their yield strength. In particular, one would expect the yield strength to increase with smaller grain sizes, according to the empirical Hall-Petch equation [27, 28]. However, at very small grain sizes, this equation breaks down. This is expected at extremely small grain sizes where grains would be unable to support any dislocation pile-ups, but significant reductions in yield strength have been seen before this point. As shown experimentally in several systems such as copper [29-47], palladium and nickel [44-50,] the Hall-Petch slope is reduced or becomes negative below a certain grain size [29-33, 50-61, 55, 56]. This behavior is known as the inverse Hall-Petch Effect (IHPE). A large body of work has been done examining this problem, including mechanical testing [29-56], *in-situ* TEM analysis [20-26] and both analytical and computation theoretical modeling [57-78]. Despite the significant amount of work, there is very little agreement about the mechanisms associated with the IHPE in nanocrystalline materials. In this regard, the question of what causes the IHPE will be addressed in detail in this work, and the anomalous lack of dislocations will be explained.

1.2 OBJECTIVES AND MAIN CONTRIBUTIONS

1.2.1 Objectives

To address the aforementioned issues and develop a more complete understanding of the mechanical behavior of nanomaterials, as well as an understanding of the nucleation and motion of defects, particularly dislocations, the objectives of this dissertation are: 1) To model and understand the stability of dislocations and the presence of twins in 0-D nanomaterials. We expect the results to be applicable to 1-D nanomaterials also. 2) To model and understand the inverse Hall-Petch effect in nanocrystalline materials. 3) To perform *in-situ* nanoindentation TEM experiments in nanoparticles and image the response using both diffraction contrast and phase contrast techniques. These experiments will be used to test the models developed for 0-D nanomaterials and identify the role of dislocations in the deformation of individual nanoparticles.

1.2.2 Main Contributions

The main contributions of this dissertation are as follows:

1. Development of a model explaining dislocation instability in 0-D and 1-D nanomaterials. While previous models have attempted to explain dislocation instability in nanostructures based on the image stress alone [1], the model presented in this dissertation considers additional interactions between the free surface and the dislocations. The model shows why dislocations are absent from

0-D and 1-D nanomaterials and how dislocations may form in these nanostructures.

2. Development of a model explaining the formation of stacking faults and possible twins in 0-D and 1-D face centered cubic, FCC, nanomaterials exhibiting a wide range of SF energies. The model considers changes in the Gibbs free energy of formation for perfect and partial dislocation half-loops forming in nanoscale volumes. The model shows that at the nanoscale the Gibbs free energy of nucleation for partial dislocations is lowered considerably, especially in the case of high SFE materials such as Al. This provides an explanation for the anomalous presence of stacking fault and twins in nanostructured materials with high SFEs.

3. *In-situ* TEM nanoindentation of Ag nanoparticles and imaging the response in both diffraction contrast and phase contrast modes. In the later case, the experiments are carried out in both aberration-corrected and uncorrected TEMs. To the best knowledge of the author, the nanoparticles compressed in these experiments are the smallest nanoparticles ever compressed *in-situ* in a TEM. The results of these experiments show that dislocations can exist in nanoparticles, if significant strains are applied, while dislocations are ejected if the strain is removed. The phase contrast nanocompression experiments presented in this dissertation are the first *in-situ* TEM nanocompression experiments that show well resolved dislocations. Also, the small size of the particles tested and the well resolved dislocations allow dislocation sources to be determined.

4. Development of a model explaining the inverse Hall-Petch effect in nanocrystalline metals. The model explains the deviations from the classical Hall-Petch effect using a combined dislocation/diffusion approach. The model predicts that the IHPE is less active in FCC materials with high bond energies (such as nickel). Additionally, the model predicts a significant strain rate and temperature dependency for the IHPE.

1.3 ORGANIZATION OF THE DISSERTATION

In chapter 2, the current state of understanding of defects and deformation in nanomaterials is presented. The chapter starts by discussing the early work on nanoparticles, the yield strength of whiskers and the classical Hall-Petch effect. Subsequently, the chapter will focus on the current research related with defects and deformation in nanomaterials. The discussion is divided in two parts, namely 1) defects and deformation in 0-D and 1-D nanomaterials, and 2) defects and deformation in 2-D and 3-D nanomaterials.

Chapter 3 presents the models developed by the author on defects and deformation in 0-D and 1-D nanomaterials. This includes a model on the dislocation instability in 0-D and 1-D nanomaterials and a model on the Gibbs free energy of nucleation of perfect and partial dislocations in 0-D and 1-D nanomaterials. Additionally, this chapter also presents the *in-situ* TEM nanoindentation experiments performed on Ag nanoparticles. The experimental procedure, experimental equipment and experimental results are all discussed.

Chapter 4 discusses the Inverse-Hall-Petch model developed by the author for 2-D and 3-D nanomaterials, as well as a discussion on the results and implications of the model. Chapter 5 highlights the major findings of this dissertation and provides recommendations for future work.

CHAPTER 2: STATE OF UNDERSTANDING

2.1 INTRODUCTION

The study of size effects on the mechanical deformation of materials is a well established area of investigation with an extensive history. Though the fabrication of 0-D nanomaterials is often seen as a recent development in materials science, the study of nanoparticles has been conducted for a surprisingly long time. An early reference on the subject, dating back to one of the earliest observations of nanoparticles with a TEM contains nine different physical and chemical techniques for synthesizing nanoparticles, as well as studies on their size distributions [78]. This work, published in 1951, confirms that nanoparticles have been fabricated and studied for over fifty years. In fact, the chemistry of producing nanoparticles in solution (colloidal science), was quite advanced by the 1950s. However, physical scientists were unsatisfied with some aspects of nanoparticles generated via colloidal methods. In particular, they were looking for particles that were separated from one another both physically and electrically so they could study quantum confinement effects in actual materials [79]. To this end, a new technique for nanoparticle production was developed called *inert gas condensation*. This method had several advantages over older chemical methods, including higher yields, as well as the production of physically and chemically isolated particles. In many ways, the inert gas condensation technique ignited a large interest in 0-D nanomaterials. However, until this dissertation, no experiments had been done to study size effects on the mechanical properties of nanoparticles largely due to difficulties in instrumentation.

On the contrary, size effects on the mechanical properties of 1-D nanomaterials have been well studied. The precursor for these investigations was the study of metallic whiskers (wires with diameters of a few microns or less) starting around 1950. Since the first deformation experiments on whiskers, there has been a considerable interest in their behavior due to their increased resistance to yielding and fracture compared to conventional bulk form materials. In one of the first experiments, a Sn filament with a diameter of ~1.8μm was strained with a manipulator inside a SEM while images were captured *in-situ* [80]. A very high resistance to plastic deformation was reported, which led to a significant interest in the mechanical properties of whiskers [81]. Tension experiments on various metallic whiskers uniformly showed increasing yield and failure stresses with decreasing whisker size [81]. In the case of metallic whiskers, the ultimate tensile strength was found to be proportional to $d^{-0.6}$, where d is diameter of the whisker. The increased yield strength was attributed to an initial lack of dislocation defects, which could greatly increase the amount of stress required to generate new dislocations.

In many ways, the study of the mechanical properties of metallic whiskers set the precedent for the study of many modern nanostructures. Perhaps the most important aspect of the studies on metallic whiskers to this dissertation is that it has inspired the modern study of compression in focused ion beam (FIB)-machined micro and nanopillars. This technique offers several advantages, and a few disadvantages, when compared to the tension experiments of whiskers. Its largest advantage is that it is done *in-situ* in a SEM. However, compression tests are somewhat more difficult to interpret than tension tests.

Finally, with respect to 2-D and 3-D nanomaterials, the origins of interest started in the early 20th century, when Hall and Petch [27, 28] discovered an empirical relationship between the yield strength of a metal and its grain size. There were several unsuccessful attempts to theoretically model this behavior, until what is now known as the *Hall-Petch effect* was formulated independently by E.O Hall [27] and N.J Petch [28].

The explanation of the classical Hall-Petch effect (CHPE) was a major development in the history of metallurgy and dislocation theory. In Hall and Petch's classic papers, the authors discussed how dislocations can carry deformation across grain boundaries. The idea was that a pile-up of dislocations could form at a grain boundary and that the additional stress on the leading dislocation of the pile-up could help initiate slip in an adjacent grain. Additionally, as larger grains could accommodate larger dislocation pile-ups, higher stresses would be present on the leading dislocation. Thus, for larger grains, the higher stress at the leading dislocation would lower the applied stress required to activate slip in adjacent grains. Because the pile-up length is based on grain size, and the stress on the leading dislocation depends on the number of dislocations in the pile-up, a lower stress is needed to transfer slip between grains in coarser-grained materials. This means that materials with large grains are weaker. The converse is also true, i.e., small grains cannot support large dislocation pile-ups, which leads to less slip transfer to adjacent grains. In other words, a higher applied stress is required to promote deformation in finer grained materials, which leads to higher strengths.

Following the Hall-Petch model, a simple extrapolation predicts that extremely high yield strengths should be possible for very small grain sizes. This prediction has lead researchers to produce materials with finer and finer grain sizes in an effort to achieve high strengths. Interestingly, the production of 2-D and 3-D nanomaterials was initiated by the inert gas condensation method [29]. Mechanical specimens were made with compacted powder, allowing some of the first tests on 3-D nanomaterials. However, it was not until fairly recently that materials processing technology has been able to produce, in a systematic fashion, fully dense materials with grain sizes at the nanoscale.

2.2 DEFECTS AND DEFORMATION IN NANOPARTICLES

While there has been extensive work done examining defects in nanoparticles, especially twins, an experimental and theoretical understanding of deformation in metallic nanoparticles is very limited. It is unclear how the unique defect behavior of nanoparticles contributes to their deformation behavior, and vice-versa.

Planar defects were among the first defects to be studied in nanoparticles [82]. Starting in the later 1960s, TEM studies examining the structure of nanoparticle have showed interesting results. Namely, very regular highly twinned nanoparticles were observed [82]. These were dubbed multiply twinned particles (MTPs) and became the subject of a considerable amount of interest [82-89]. The original observation of MTPs was done by Ino and coworkers [82, 83]. The authors detected anomalous diffraction patterns in particles that were grown epitaxially on NaCl and KCl substrates. The authors observed 12 (111) spots in a single diffraction pattern, far more than could exist in a zone axis pattern for a single crystal. When dark field imaging was done using these (111) spots, the authors observed that only some sections of the crystal lit up for each dark field image, indicating that the nanoparticle was not a single crystal. To explain this observation, Ino and coworkers assembled structural models with multiple tetrahedral units with well defined twin relationships to one another to form decahedral and icosahedral nanoparticles.

These results were elaborated on by Yagi *et al*. [84], Marks *et al*. [85], and Johnson [86]. Yagi *et al.* grew gold nanoparticles on an MgO substrate *in-situ* in the TEM. They reported the formation of multiply twinned particles, especially at small sizes. The authors saw that MTPs were not formed by the agglomeration of multiple particles. Additionally, the authors observed nanoparticles that originally did not have twins transform into MTPs during particle growth. Marks *et al.* [85] conducted a phase contrast TEM examination of MTPs. This analysis did not reveal any new information about the twin defects themselves but they did observe dislocations in the MTPs. This is surprising, because dislocations are not typically seen in nanoparticles that are not multiply twinned. A more modern experiment was done by Johnson *et al.* [86]. The authors used phase contrast aberration corrected TEM of a decahedral MTP with geometrical phase analysis to attempt to assess the validity of the disclination model for decahedral MTPs. The geometrical phase analysis was highly successful at determining the rotations of the twinned crystal, but had more difficulty determining the strain. However, the authors showed that almost all of the ~7° gap in rotation could be accounted for by the geometrical phase analysis, supporting a disclination model.

In addition to these microscopy studies, various analytical models have been developed to help understand twins and MTPs. The geometry of MTPs is discussed by Yang and Yang *et al.* [87, 88]. In particular; the authors address the fact that it is not possible to make decahedra or icosahedra from unstrained FCC tetrahedra. The authors discuss the necessary distortions that a perfect material would have to undergo to become a MTP. Based on this analysis, they also predict diffraction patterns, bright field and dark field TEM images for MTPs. The strain inside MTPs is further discussed by Howe *et al.* [89, 90].

Aside from the case of MTPs, there have been other studies on the behavior of defects in nanoparticles. For instance, nanoparticles were subjected to radiation by energized particles and observed, either *in-situ* or ex-situ by TEM, to examine the defects structures that were generated. Nanoparticles were damaged by high energy ions *in-situ* in a TEM as reported by Ohtsuka *et al.* [91]. In this article, the authors irradiated Au nanoparticles with 35 keV ions. Bubble formation was seen, but no dislocations were reported. The lack of observation of dislocations could potentially be because of poor imaging conditions.

Gryaznov *et al.* developed a model to explain the lack of dislocations in single crystal nanoparticles that are observed after deformation or irradiation [1]. The authors consider a dislocation loop in the center of a spherical nanoparticle, and the effect of image stresses on this loop. In this way they calculate the minimum nanoparticle size that dislocations would be expected in. The method used by the authors is sound, but does not address all the possible interactions a dislocation can have with a surface.

While there have been several studies into the deformation behavior of nanoparticles, understanding of the deformation behavior of nanoparticles is still in its infancy. Nowak *et al.* performed an experiment were a Si nano/submicron particle that was compressed until fracture [92]. The particle was reported to be 216nm in diameter with an amorphous surface oxide of 5.4nm. The authors claimed the presence of bend contours during the deformation process, but no effort was taken to analyze the properties of the bend contours. It is possible that the contrast attributed to the bend contour in was actually caused by another diffraction contrast effect. The authors report that the particle was deformed to a 13% engineering strain, which is implausibly high. In addition, plastic deformation mechanisms were not discussed. The authors obtained the stress at fracture for the nanoparticle by extrapolating the results of another experiment on Si nanoparticle compression.

2.3 DEFECTS AND DEFORMATION OF MICRO-NANO PILLARS

2.3.1 Compression of Micro-Nano pillars

Some of the most important micro-nanopillar compression experiments investigating the fundamental strength of materials have been done on single-crystal FCC pure metals, such as Ni, Cu and Au. These materials provide an excellent opportunity to study the fundamental effects of dimensional constraints on the mechanical properties, at or approaching the nanoscale. In particular, complications caused by grain boundaries or secondary phases are expected to be absent in these materials, allowing pure size effects to be studied. Though many of the pillars tested were technically not at the nanoscale, the work has direct implications to the study of mechanical deformation in nanomaterials, and therefore should be considered.

It is instructive to begin our review of defects and deformation during compression of nanomaterials with a narrative description of the deformation process that occurs during the compression of a single crystal micro-nanopillar (Figure 2.1). As the pillar is initially loaded, it deforms in a linearly elastic fashion. Linear elastic deformation continues until a diameter-dependent, critical stress in is reached. This critical stress is usually very high when compared to the yield stress of conventional materials. After this critical stress is reached, the sample deforms perfectly plastically at the critical stress. The perfectly plastic deformation continues until some amount of strain is accommodated and then linear elastic deformation resumes. The new linear elastic regime continues until a new higher critical stress is reached, and then perfectly plastic deformation begins again. This cycle can repeat several times during deformation.

One of the most interesting characteristics regarding the deformation in micro/nanopillars is that they show increased yield strength as their diameters are decreased, similar to whiskers strained in tension. This effect was originally seen by Uchic *et al*. [11] in Ni and Ni_3Al-Ta pillars with sizes ranging from 40μm to 0.4μm in diameter. Later this effect was demonstrated in Ni by Dimiduk *et al*. for a similar size range [12]. Similar results were seen in Au by Greer *et al*. for gold pillars as small as 400nm [94] and by Volkert [14] for pillars with diameters as low as 200nm. These results seemed to be the same regardless of whether the samples were produced by FIB machining [11, 12, 14, 94] or by electrochemical methods [85], indicating that it is unlikely that the strengthening was caused by the processing methods. There is agreement in the literature that the yield strength increases substantially as micro/nanopillar size is reduced

It is known that that compressed pillars deform via a dislocation mechanism. During deformation, micro-nanopillars show slip bands that are associated with dislocation motion [11, 12, 14, 94]. However, because SEMs lack the ability to image the interior of the samples, the mechanisms of dislocation generation remain unknown. It has also been shown by Greer *et al*. [95] that dislocations do not accumulate in compressed nanopillars. Post mortem TEM examination of compressed nanopillars revealed very few dislocations, and those that it did reveal had Burgers vectors that were perpendicular with the direction of the compression. No dislocations that would have experienced shear stress due to the compression were seen. This indicates that micro-nanopillars are essentially dislocation free-structures.

Aside from dislocation defects, other defects can be produced by the FIB machining process that is often used to produce the micropillars. These effects were studied in by Kiener *et al*. [96]. In post mortem TEM analysis, it was shown that the FIB machining causes accumulation of a network of dislocation-like defects, amorphous regions and Ga ion implantation. Concerns about these FIB related defects has been so great that several models for nanopillar strengthening considered the effect of the FIB damaged layer as the cause of increasing yield strength in nano and micropillars [87]. This was serious enough concern that experiments were done on pillars fabricated by other electrochemical techniques [94]. The electrochemically produced samples behaved the same as the FIB machined samples. Though there is agreement that FIB machining causes defects in the samples, experiments on non FIB machined pillars show that these defects are not the cause of strengthening in nanopillars.

The general shape of the stress strain curve for compression of micropillars and nanopillars has been demonstrated in several different materials by many authors [11, 12, 14, 94]. Uchic *et al*. showed the elastic-plastic-repeat stress strain curve in Ni and Ni_3Al-Ta pillars [11]. These findings were repeated for gold [94, 14] by Volkert *et al*. and Greer *et al*. and for additional Ni samples by Dimiduk *et al*. [12]. There is, therefore, very good agreement on the shape of the stress strain curve for micropillar compression.

Theoretical models have also developed to explain the mechanical behavior of micropillars and nanopillars. The increase in yield stress that is associated with decreasing diameter in micropillars and nanopillars is typically explained by the limited number of dislocation sources available [11, 12, 14, 17, 94] or alternately, by FIB damage [96]. Micro-nanopillar strengthening due to the limited number of dislocations sources is analogous to strengthening in whiskers. Because of the limited number of dislocation sources in a micro-nanopillar, the strength of even the weakest source is expected to be quite high. It is typically assumed that for micropillars, Frank-Read sources are still operational. However, for nanopillars this becomes implausible, and dislocation nucleation at the surface of the pillar is considered [17]. In either case, the source of dislocations has not been imaged.

One major difference between deformation in micro/nanopillars and whiskers is their post-yielding behavior. Metallic whiskers show very little resistance to deformation after yielding, while nanopillars can show considerable hardening. This is attributed to dislocation escape and dislocation starvation [11, 12, 14, 17, 94]. In micro/nanopillar compression dislocations are generated from one source at a constant stress until the source is exhausted. These dislocations glide across the micro/nanopillar and escape at the free surface without a significant amount of dislocation multiplication occurring. This corresponds to the perfectly plastic portion of the stress strain curves discussed above. After exhaustion of the weakest source, linear elastic behavior resumes until the next weakest dislocation source is activated. This effect is also modeled by computational simulations, which are discussed in the next section.

In general, the literature on the deformation of FCC micropillars shows a high degree of consensus in several areas. Namely, it is well established that micropillars show an increasing resistance to deformation as their size is reduced. Additionally, for smaller micropillars, the stress-strain curve has a distinct shape, where the elastic regions are separated by perfectly plastic regions. On the other hand, scientific agreement on the mechanisms of pillar strengthening is less well established. The most popular theory is that mobile dislocations escape the micropillars before they can participate in dislocation multiplication process, such as double cross-slip. This effects has two implications; i) new dislocation sources are not generated, and ii) pre-existing dislocation sources become exhausted. The combined effects of i) and ii) lead to the elastic/plastic/elastic stress strain curves that characterize microcompression.

Additionally, the literature on the experimental compression of micropillars only begins to enter the nanometer range. Results on pillars <100nm are rare. Many authors realize that the dislocation starvation mechanism will break down as the diameter of the pillars is reduced from the micrometer scale to the nanometer scale. At this point, many authors predict that dislocations nucleating heterogeneously on the surface of the nanopillar will dominate deformation, but experimental evidence of this from literature is still lacking.

2.3.2 Computational Models

Despite the great success of the *in-situ* SEM compression experiments on micropillars, there are some issues that these experiments are simply unable to address. An example of this is the behavior of dislocations inside the crystal. Another aspect of dislocation motion that makes it difficult to assess is the very high speed of dislocations in crystals. Because of their quick motion, even if the dislocations are imaged via TEM, their motion is still very hard to track.

To address both of these points, computer numerical simulations of micropillar compression have been done using various methods. In this regard, dislocation dynamics simulations have been very important. Dislocation dynamics simulations consider dislocations in a material that is otherwise governed by the laws of continuum mechanics. The generation, propagation and motion is calculated in discrete steps and used to determine the mechanical properties of the simulated test material. Using this numerical method allows the simulated behavior of dislocations in materials to be studied, free from imaging and timescale constraints that limit their study via other mechanisms.

Two important dislocation dynamics simulations were performed by Deshpande *et al*. [16] and Tang *et al*. [96]. A simplified 2-D dislocation dynamics model was presented by Deshpande *et al*. to study the effect of size on micropillar strength [16]. A more complex 3-D simulation was conducted by Tang *et al*. [27]. Both simulations considered deformation occurring by the activation of a random array of Frank-Reed sources. The simulation does not consider the concentration of dislocations or sources to be a function of micro/nanopillar size. Both simulations showed that the yield strength increases as the pillar diameter decreases. This is explained stochastically; the smaller a pillar is the lower the probability it will have sources with low critical stresses. The simulations also show that dislocations do not participate in double cross slip or other dislocation generation activities during deformation. These simulation results are a confirmation of the analytical models for strengthening that are based on a low number of dislocation sources.

When viewed as a whole, the dislocation dynamics simulations in micropillar compression confirm that the dislocation starvation mechanism is a good explanation for the experimental results. However, because the dislocation dynamics simulations commonly assume that dislocations are generated at Frank-Read sources, extrapolation of these simulation results to the nanoscale would likely be problematic. Frank-Read sources are not expected to be active in 0-D and 1-D nanomaterials. Additionally, interactions between dislocations and the surface are often simplified or neglected in dislocation dynamics simulations. This means that dislocation dynamics experiments are less than an optimal tool for understanding pillar compression, as it enters the nanometer range and dislocations are expected to nucleate from the surface of a nanopillar. Therefore, molecular dynamics experiments on nanopillars are necessary to evaluate the deformation behavior on 1-D and 0-D nanomaterials.

Molecular dynamics simulations consider the behavior of each individual atom in the material. This means that these simulations can very accurately simulate materials behavior, but are extremely computationally intensive. The computational requirements of molecular dynamics simulations place several limitations on the experiments that can be simulated. For instance, molecular dynamics experiments on mechanical deformation often consider strain rates that are ten or more orders of magnitude larger than strain rates commonly used in experiments. Additionally, because every atom’s behavior is computed, the crystals simulated are often small. Despite these limitations, molecular dynamics simulations are a useful tool for understanding deformation. They are particularly useful for determining the plausibility of specific deformation mechanisms. Additionally, molecular dynamics simulations on nanocompression can study smaller crystals that have been studied experimentally or by dislocation dynamics. For these reasons, several molecular dynamics simulations have been done on FCC nanopillars.

Molecular dynamics (MD) simulations have been conducted for Cu and Au with diameters up to 30nm and very high strain rates, from 10^8-10^{14} s^{-1} [19, 97, 98]. Guo *et al*. conducted an MD simulation on Cu nanopillars. The simulations showed very high stress, likely due in part to the very high strain rates (10^8-10^{12} s^{-1}). Additionally, nucleation of partial dislocations from the free surface of the sample was also seen. MD simulations of Au nanomaterials were carried out by Rabkin *et al*. and Zepeda-Ruiz *et al*. [97, 98]. Significant strengthening was seen in the simulations. Likewise, the simulations in gold also showed generation of partial dislocations at free surfaces.

The molecular dynamics experiments show that heterogeneous nucleation of partial dislocations at the surface of nanopillars can occur during compression of nanopillars. Even though the simulations consider unrealistically high strain rates, the observation of partial dislocation nucleation at free surfaces is important. It shows that dislocations nucleation may be possible at the surface in compressed 1-D nanomaterials, though it has never been observed conclusively and directly.

Additionally, even though only partial dislocations are seen in the molecular dynamics simulations, their presence may indicate that perfect dislocations could form at realistic strain rates. Unfortunately, due to the computationally intensive nature of molecular dynamics, simulation of these lower strain rates and larger sample sizes are not practical. Therefore, other techniques are necessary, including *in-situ* TEM nanoindentation.

2.4 DEFECTS AND DEFORMATION IN 2-D AND 3-D NANOMATERIALS

2.4.1 The Inverse Hall-Petch Effect

One of the goals of developing nanomaterials is to provide high strength structural materials. However, it has been shown that metals with very small grain size become softer [33]. This is known as the inverse Hall-Petch effect. Through nanoindentation experiments, miniaturized tensile experiments and *in-situ* TEM experiments, it has been shown there are surprisingly few mobile dislocations and a lower than expected yield stress. These phenomena are believed to be linked, as the small amount of mobile dislocations is often cited in explanations for the lower yield stress. Understanding both of these phenomena is essential for an understanding of the mechanical behavior of 2-D and 3-D nanomaterials.

The most persistent controversy in the understanding of the deformation of 2D and 3D nanomaterials is the so-called inverse Hall-Petch effect (IHPE). The classical Hall-Petch effect is given by equation 2.1.

$$\sigma_y = \sigma_0 + kd^{-1/2} \tag{2.1}$$

where σ_y is the grain yield stress, σ_0 is the lattice friction, k is the grain boundary strengthening factor and d is the grain size. Equation 2.1 shows that yield strength should increase as grain size is decreased. However, in many experiments the yield strength actually decreased with increasing grain size. There have been a large number of experiments investigating this effect and a larger number of hypothetical explanations for this behavior have been offered [57-78], but theory has had trouble keeping pace with the advancing understanding of deformation in 2D and 3D nanomaterials.

2.4.2 Mechanical Testing Experiments on 2-D and 3-D Nanomaterials

Advances in material fabrication technology allowed for the mechanical testing of materials with grain sizes in the nanometer range. As mentioned above, many of the tests found yield strengths that were lower than predicted by the classical Hall-Petch effect. Experiments showing the IHPE are characterized by a lower than expected, or even negative, value for k from equation 2.1.

This section will discuss quantitative experiments done on the yield strength of nanocrystalline FCC metals, particularly Ni and Cu. The discussion will focus on FCC metals because they have been covered by the literature in the most depth. This is also the reason that the focus will be on Ni and Cu.

There has been a large volume of research conducted on the effect of grain size on the effect of grain size on the yield strength of Cu. In fact, the first hints of the IHPE were seen before the term “nanomaterials” was in common use. From that point, interest in IHPE has only grown. In this section, experiments investigating the IHPE in nanocrystalline Cu are discussed in detail.

Many experiments have been done on the Hall-Petch effect in Cu [29-35, 38, 39, 41, 44, 47, 99]. Early results investigating the CHPE in nanoscale and ultrafine grains was done by Merz *et al*. [41] and Hansen *et al*. [99]. Merz *et al*. tested sputtered films with mean grain sizes between 56nm and 2000nm. Tensile testing of the samples showed that CHPE was obeyed at all grain sizes tested. Hansen *et al*. evaluated Cu samples with grain sizes between 8.5 and 60µm. These samples were fabricated by recrystallization of high purity Cu. Tension tests confirmed that the CHPE was followed for these samples as well. Though these experiments did not show the IHPE, they are some of the first to examine the yield strength of 3-D nanocrystalline materials.

With the invention of inert gas condensation (IGC), investigation of nanomaterials with extremely small grain sizes became possible. As these materials started to be evaluated, IHPE behavior began to be reported [29-35]. Several different researchers studied Cu samples produced by IGC followed by powder compaction. Powder compaction typically led to samples with densities that were significantly lower than the theoretical density. Additionally, due to the low yield of the process, and difficulties of manufacturing tensile specimen, many of these experiments were evaluated by Vickers hardness tests. Nieman *et al*. [30], Chokshi *et al*. [29], Nieman *et al*. [31], and Fougere *et al*. [32] all conducted Vickers hardness tests on nano-grained Cu fabricated by compaction of IGC powder. None of these works reported fully dense materials, however all of them showed softening for at the lowest grain sizes, indicating the presence of the IHPE.

Not all of the mechanical tests done on compacted IGC nanocrystalline Cu powders used Vickers hardness testing. Gertsman *et al*. tested their nanocrystalline Cu samples by miniaturized disk bending [33], and they reported an IHPE as well. Sander *et al*. used tension tests to study the yield strength of nanocrystalline Cu, and they also found an IHPE. Iyer *et al*. tested an IGC powder that was hot pressed instead of cold pressed, increasing the solid's density [35]. Tension tests on the denser samples did not show the IHPE. Despite different testing techniques, the IHPE continues to be observed except, intriguingly, in the more dense samples.

Additionally, the Hall-Petch effect has been examined in Cu samples that were not fabricated by powder compaction. Vailiev *et al*. [39] and Haouaoi *et al*. [47] tested Cu samples that were fabricated using a severe plastic deformation technique known as equal channel angular extrusion (ECAE) and Chen *et al.* [44] tested nano-grained Cu samples produced by a surface metal attrition treatment (SMAT). All of the techniques produce fully dense samples, but the drawback of these techniques is that grains sizes tend to be fairly large (for nanomaterials). None of these authors reported results consistent with the IHPE. Additionally, the grain sizes of the samples that were tested in these experiments were significantly larger than the grain sizes that showed the IHPE in the previous literature.

Huang *et al.* tested nanocrystalline layered Cu and Ag samples [38]. The nanocrystalline samples were fabricated by electron beam evaporation. Instead of testing pure Cu or Ag films with nanoscale grain sizes, the deposition Cu and Ag was alternated, making multilayer structures with grain sizes comparable to the layer thickness. The samples were observed by electron microscopy, and the authors reported that no voids were seen. The elastic properties of the specimens were measured via tension testing with *in-situ* laser diffraction. The elastic values for Young's modulus measured were below the literature for coarse grained materials. The yield strengths were also measured. Ag/Cu multilayered composites with layer thicknesses as low as 3nm were tested. The authors report that the CHPE was followed. These results are intriguing, even if they are not directly comparable to the results for pure nanocrystalline Cu.

When viewed in its totality, the work on the IHPE in Cu is somewhat uncertain. Some experiments clearly show the IHPE, but these experiments were very often done on samples with significant porosity, which can significantly degrade mechanical processes. However, the majority of the work showing agreement with the CHPE was done on samples with grain sizes large enough that the IHPE would not be expected anyway. Because of these conflicting messages, it is difficult to determine if the IHPE is a real effect without additional analysis. Figure 2.2 shows compiled results from Cu yield stress vs. grain size experiments discussed above, with several additional experiments added. The curve fit was drawn in free-hand because the expected functional form of the IHPE is not known. From Figure 2.2, the reduction in the slope of the Cu yield stress indicates the presence of an IHPE. However, if the legend of figure 2.2 is examined, it is clear that the data supporting the IHPE was all from samples fabricated by consolidation of nanopowders.

There has also been a large amount of work done on the validity of the CHPE in nanocrystalline Ni. Some of this effort was inspired by reports of the IHPE in nanocrystalline Cu and Pd. In contrast to the work on IHPE in Cu, most of the work on yield stress on nanocrystalline Ni was done on samples produced by electrodeposition. This makes interpretation of the results significantly easier for a couple of important reasons. Namely, the effects of different fabrication techniques do not need to be considered and electrodeposited samples typically do not have any porosity.

The mechanical properties of electrodeposited nanocrystalline Ni have been evaluated by several different experiments using Vickers hardness tests and tension tests. Hughes *et al.* [49], and Xiao *et al.* [48] conducted mechanical testing on electrodeposited nanocrystalline Ni using Vickers hardness tests. Nickel samples with grain sizes as low as 12nm were tested by Hughes and grain sizes as low as 9nm were tested by Xiao *et al*. In both experiments the CHPE is followed. Tension tests on nanocrystalline Ni specimens fabricated by electrodeposition were done by Wang *et al.* [40] and Ebrahimi *et al.* [46]. In the experiment conducted by Wang *et al.*, the IHPE was seen, but only in the smallest sample, which had a grain size of 6nm. In Ebrahimi *et al.*'s experiment [46], the CHPE was followed, but only grain sizes between 45-300nm were tested.

Some other experiments were done to evaluate the properties of nanocrystalline Ni samples. Lu *et al.* used Vickers hardness tests to examine the mechanical properties of a Ni-P amorphous alloy that was recrystallized [100]. Using this method, they were able to test grain sizes as low as 7.5 nm. These nanocryastalline Ni-P samples showed IHPE behavior. Schuh *et al.* [51] tested electrodeposited Ni samples with grain sizes as low as 12nm using a nano-scratch technique. The results showed IHPE behavior for the smallest grain sizes. An experiment on an electrodeposited Ni-W alloy was done by Giga *et al.* [55]. The authors evaluated the yield strengths of nanocrystalline Ni-W with grain sizes as small as 2nm. This experiment also showed IHPE behavior at small grain sizes.

Taken collectively, the literature on the validity of the CHPE in nanocrystalline Ni is hard to interpret. Individual reports often claim to have found evidence of an IHPE, but when all the results are taken together, many of these findings appear inconclusive. Additionally, the best evidence for the IHPE in Ni which is, the work of Giga *et al.* [55], reports results for a Ni-W alloy, which is not directly comparable to pure Ni.

2.4.3 Ex-Situ TEM Deformation Experiments

Ex-situ TEM has been a frequently used tool for understanding deformation in nanostructured materials. TEM provides a large amount of information about the microstructures of nanocrystalline materials and is useful for determining changes in microstructures that undergo plastic deformation. In addition, the results of ex situ TEM observation have often helped the development of theoretical models for the IHPE.

When nanostructured materials are deformed and then later observed ex-situ by TEM, an increased density of dislocations is not typically seen. This has been shown by several ex-situ deformation experiments [37, 43, 46]. Ultrafine grained (100s of nm) Cu samples were tension tested and then observed by TEM by Ebrahimi *et al.* [46]. Dislocations were not seen in this experiment. Lu *et al.* conducted an experiment where nanocrystalline Cu with a grain size of 20nm was rolled to very large reductions [43]. The samples were cold rolled at room temperature up to fractional strains of 51. The dislocation density was studied by TEM and XRD, and it was seen to increase at first and then hold steady as a function of strain. Another experiment evaluating the effect of deformation on defect structures in nanomaterials was performed by Legros *et al.* [37]. This experiment was done on a nanocrystalline Ni sample fabricated by hot compaction of IGC powder that was tension tested and Vickers hardness tested before ex-situ TEM observation. In both cases, dislocations were not seen. These experiments show that dislocations are not seen in nanocrystalline 3-D metals that have been deformed at room temperature.

Low temperature deformation studies have also been done. Wu *et al.* [101] conducted two experiments. In one, nanocrystalline Ni was tension tested at room temperature, while in the other nanocrystalline Ni was tension tested at liquid nitrogen temperature. For both experiments, ex-situ TEM observations were made. For the room temperature experiment, deformation twins were observed. Very few dislocations were seen, except in the vicinity of the twins. The liquid nitrogen rolling experiments yielded a very different result. At these temperatures, there is a significant retention of dislocations. The contrast between the low temperature and the room temperature experiments is striking. Additionally, it implies that there is some sort of thermally activated process that either eliminates dislocations or accommodates plastic strain more easily than dislocation motion in nanocrystalline metals.

The most important finding from this research is that there are few retained dislocations after deformation in nanocrystalline metals. This could be because dislocation motion is never active in these materials, or because dislocations are unstable before they could be observed by TEM.

2.4.4 In-situ TEM Deformation Experiments

In-situ TEM deformation experiments have been critical to understanding the deformation of nanomaterials and IHPE. In particular, they are very valuable because they show deformation processes progressing in real time. Therefore *in-situ* experiments can reveal transient behavior that is invisible in post mortem studies.

Some of the first *in-situ* TEM experiments on nano-grained metallic films were done on nanomaterials that were deposited on top of another foil. Milligan *et al.* [20]

studied nanocrystalline Au that was sputtered onto an Al foil. During deformation, the Au was seen to deform plastically, but dislocations were not seen. Another *in-situ* TEM experiment on Au that was deposited on a polyvinalformal film was done by Ke *et al.* [102], and it produced similar results. In both experiments, the images were taken in the vicinity of a crack, complicating the stress state. Additionally, imaging was impeded by the presence of the Al and polyvinalformal films respectively. Regardless, it is still significant that these experiments showed a low level of dislocation activity in strained nanocrystalline materials.

Further *in-situ* TEM deformation experiments have shown dislocation motion, usually indirectly [23, 24, 26, 74, 103]. Youngdahl *et al*. [26] and Mitra *et al.* [103] did *in-situ* deformation experiments on nano-grained Cu with grain sizes of 20-500nm and 30-60nm respectively. In both cases rapid changes of contrast, which are commonly associated with dislocation motion, were seen even in very small grains. In Mitra *et al*.'s experiment, pauses in straining were used to image individual dislocations. Additionally, these observations were made far away from cracks, ensuring a more uniform stress state. *In-situ* TEM deformation experiments were done in Ni by Hugo *et al.* [24], and Kumar *et al.* [74]. Both of these experiments show dislocation motions as well, though in the later the dislocation motion was concentrated to the proximity of the crack tip. Additionally, Hatter *et al.* [23] performed an *in-situ* TEM straining experiment on an ultrafine grained Al specimen. In this experiment, dislocations were only seen in the vicinity of the crack. Despite the fact that many of the experiments only displayed dislocations in the vicinity of the crack, these *in-situ* experiments make it clear that dislocation can exist in nanocrystalline materials and imply that they may deform via a dislocation mechanism.

Another experiment on nanocrystalline Ni was done by Shan *et al.* [22]. The *in-situ* TEM nanodeformation experiment was performed on pulsed laser deposited Ni with a grain size of ~10nm. The authors report the same rapid changes in grain contrast as other the previously discussed reports, but attribute the changes to grain boundary rotation instead of dislocation motion. Because the evidence of both dislocations motion and grain rotation is indirect, it is unclear which is actually occurring.

In-situ deformation experiments on nanocrystalline metals show that dislocation motion is possible in nanocrystalline metals. The flashes of contrast that are seen and attributed to dislocation motion in the literature imply that dislocations are present nanocrystalline metals. However, it is somewhat unclear if dislocations exist in nanocrystalline materials with grain sizes small enough to expect the IHPE.

2.4.5 Theoretical and Computational Models for the IHPE

So far, most of the models proposed to explain the IHPE behavior fall into at least one of four categories, namely dislocation-based models, diffusion-based model, grain-boundary-shearing models and two-phase-based models. In this section, models for each of these four categories are introduced and discussed

In dislocation-based models, it is assumed that plastic strains in the nanomaterials are still carried by dislocations. The various models each contain different rationalizations that explain how grain sizes in the nanometer range can change the properties and/or behavior of dislocations. Dislocation-based models are somewhat controversial in the modern study of the IHPE because ex-situ deformation typically does not show the presence of accumulated dislocations. However, several *in-situ* TEM nanodeformation experiments have observed dislocation motion. Additionally accumulation of dislocations was seen in nanocrystalline materials deformed at 77K, implying that it is still appropriate to consider dislocation based models for the IHPE.

A variety of different dislocation-based models for the IHPE have been considered. The most conventional among them consider direct break-downs in CHPE deformation mechanisms. The models presented by Nieh *et al.* [56] and Scattergood *et al.* [57] fit this category well. Nieh *et al.* consider the operation of a dislocation pile-up mechanism in nano-grained materials, and how the mechanism might break down at very small grain sizes. Scattergood *et al.* consider a dislocation forest cutting model for the CHPE, and how the model would be affected if dislocation energies were lowered due to truncation of their strain field by nanoscale grains. Another fairly traditional model is considered by Lian *et al.* [58]. The authors of this work consider how changes in the stress that is required to bow out dislocations from Frank-Read sources in nanoscale grains could cause the IHPE. Unfortunately, these models do not represent the physical reality of deformation in nanomaterials very well. For instance, dislocations forests and Frank-Read sources are not seen in nano-grained materials.

Not all of the theoretical work supporting a dislocation mechanism for the IHPE has been analytical. A MD simulation performed by Yamakov *et al.* [60] simulated nanocrystalline Al undergoing deformation. Like all MD simulations, this experiment considered a very high stain rate, which limits its applicability to conventional experiments. Additionally, the yield strength of nanocrystalline Al has not frequently been used for studies on the IHPE. However, the simulation still had some interesting results. For instance, nucleation of perfect and partial dislocations from grain boundaries was very prevalent in the simulation. This is despite the fact that stacking faults are not expected in Al due to its high stacking fault energy.

In-diffusion based models, plastic deformation in nanomaterials is accommodated by a diffusion process. For example, one diffusion based model explains the IHPE using Coble creep of grain boundaries [29]. Other diffusion based IHPE modes consider diffusion-modified dislocation and grain boundary shearing processes. The key argument for many of these models is based on the large amount of grain boundaries. This, coupled with the fact that grain boundary diffusion is typically much faster than lattice diffusion, makes diffusion-based models seem very plausible. Experiments showing temperature dependence in the deformation mechanism for nanocrystalline metals [93], and experiments indicating strain-rate dependence of yield stress in nanocrystalline metals suggest a diffusion based model for the IHPE is appropriate.

Aside from the Coble creep suggested by Chokshi *et al.*, Masamura *et al.* present a diffusion based model for the IHPE [62]. The authors consider a combination of CHPE strengthening and conventional Coble creep as the source of the IHPE. The material’s behavior is supposed to be a combination of regions of material behaving according to the CHPE and regions of materials deforming purely by Coble creep. While the model is interesting, the treatment presented by the authors is somewhat empirical.

A more novel model was presented by Malygin [59]. This model uses a combination of dislocation and diffusion mechanisms to explain the IHPE. The author uses a mechanism where Coble creep at the grain boundary eliminates dislocations and where the CHPE is due to the dislocation forest cutting model. This model has some very intriguing features. Elimination of dislocations via a creep mechanism might help to explain the lack of retained dislocations in nanocrystalline materials that were deformed at room temperature. Additionally, it could account for the temperature dependence for the disappearance of dislocation, which had seen hinted at in reference [101]. However, the dislocation forest cutting model still remains unconfirmed for nanocrystalline materials.

Models that consider the IHPE to be the result of localized grain boundary plasticity have also been popular [63, 64, 66]. Different localized grain boundary plasticity models for IHPE use different mechanisms, such as grain boundary sliding, grain boundary shearing or grain rotation. These models also consider the large amount of grain boundaries in nanocrystalline materials which, they reason, can deform more easily than the lattice material. Support for grain boundary sliding models comes from Molecular dynamics simulations, which routinely show grain boundary sliding and application of Ashby diagrams to the results of creep experiments in nanocrystalline materials [40].

A grain boundary shearing based mode for the IHPE was proposed by Conrad *et al.* [63]. The authors consider a transition between the conventional dislocation mechanism of deformation and a proposed grain boundary shearing that occurs at a critical grain size. The grain boundary shearing activity is taken to be composed of independent thermally activated events taking place at the atomic scale. The authors determine the critical yield stress by equating the conventional yield stress from the Hall-Petch and the new yield stress from grain boundary shearing.

MD simulations have also supported grain boundary sliding explanation of the IHPE. Swygenhoven *et al.* [64] presented a MD simulation in Ni and Cu that showed significant strain accommodation by grain boundary sliding. Yamakov *et al.* [66] presented a MD simulation in Al with 7-30nm grain sizes. They report grain boundary sliding for the smallest grain sizes. These simulations have the same limitations as other MD simulations, namely very high strain rates.

Yet another class of models explaining the IHPE considers nanomaterials to be a combination of two or more different phases. A typical argument is that, in nanomaterials, grain boundaries are significantly different that in conventional materials, and therefore constitute a second phase. This argument is poorly supported, because TEM examination of nanocrystalline materials has shown that there is no amorphous region between the nanocrystalline grains [111]. Multiphase models will therefore only be treated briefly [69-72].

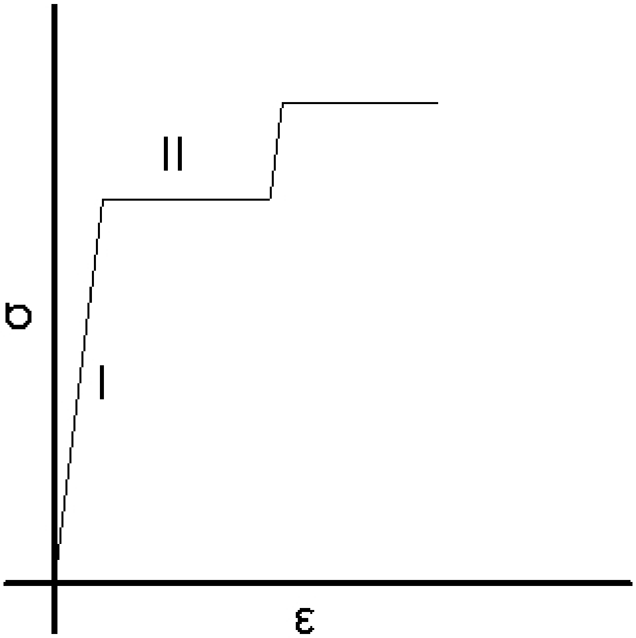

Figure 2.1: A schematic diagram of the mechanical response of a micro-nanopillar undergoing compression. In the area marked I, the pillar is deforming in a linear elastic fashion. When the applied stress on the particle exceeds the critical stress required to activate a dislocation source, the pillar begins to deform in a perfectly plastic manner. The region of perfectly plastic deformation is labeled II in the figure. Eventually, plastic deformation ceases and elastic deformation resumes. This second period of elastic deformation continues until another dislocation source is activated. This process can repeat several times.

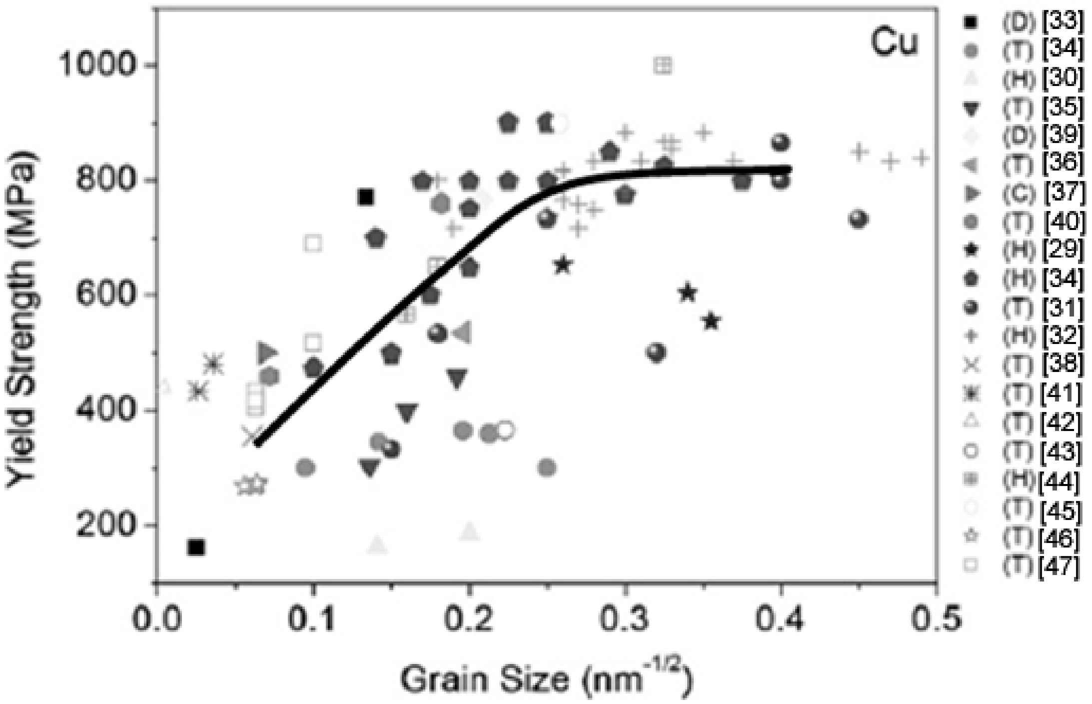

Figure 2.2: A plot of the reported yield strength vs grain size for Cu. The data points are from the literature. The curve was drawn free-hand, and implies the presence of the IHPE.

CHAPTER 3:

DEFORMATION OF SINGLE CRYSTAL 0-D AND 1-D NANOMATERIALS

3.1 INTRODUCTION

0-D and 1-D nanomaterials show a conspicuous lack of dislocations, regardless of the materials processing history, even after significant deformation and radiation damage [1, 91]. However an abundance of twins seems to exist, even in materials with high stacking fault energies [7]. Because of these observations, it has been suggested that either dislocations cannot exist, or that dislocations are unstable in nanoparticles. Additionally, much has been said about the nucleation of deformation twins [7-9] in 3-D nanomaterials, but very little work has been done on mechanical twinning in isolated nanoparticles.

Another phenomenon of interest related with 0-D and 1-D nanomaterials is associated with mechanical compression. In the case of 0-D nanomaterials no experiments, to the author's knowledge, have been performed at the nanoscale. The experiment that has been the closest to the nanoscale was an *in-situ* TEM compression of ~200 nm Si particles [92]. However, the particles tested were too large to extract relevant information at the nanoscale and the mechanical deformation of Si is also expected to be different from that of metals. In the case of 1-D metallic nanomaterials, ranging in diameter from hundreds of nanometers to several micrometers, several compression experiments have been conducted *in-situ,* typically in an SEM, although several *in-situ* TEM experiments have been carried out too [11, 12, 14, 94]. The experiments showed that as the pillar size was decreased, the pillars exhibited increased strength. Additionally, dislocation slip bands could clearly be seen. Attempts to model and understand the mechanisms of deformation in these pillar nanocompression experiments have been made [11, 12, 14, 17, 94, 96]. However, it has been difficult to experimentally validate these models due to the limitations of SEM microscopy. In fact, even the *in-situ* TEM experiments carried out so far have been unable to reveal details about the exact mechanisms of deformation, such as the identification of dislocation nucleation sites.

Finally, another important effect that is relevant for the deformation of 0-D and 1-D nanomaterials is the fact that as crystal dimensions approach the Burgers vector of a dislocation, the amount of strain a single dislocation carries can become very large.

To address these aforementioned issues in 0-D and 1-D nanomaterials, this dissertation will first propose three models: 1) a model explaining the absence of perfect dislocations in 0-D and 1-D nanomaterials, 2) a model explaining the presence of twins in 0-D and 1-D nanomaterials and 3) a model explaining the increasing amount of strain caused by the motion of individual dislocations as sample size is reduced. Secondly, this dissertation will show how the first model, developed to explain the absence of dislocations within a nanoscale crystal, can be applied to nano-compression experiments. This in turn will provide the first insights into the mechanical properties of metallic nanoparticles and it will help explain the enhanced strength of nanopillars.

3.2 THEORETICAL MODELS

3.2.1 Dislocation Behavior in 0-D and 1-D Nanomaterials

It is well known that dislocations are not observed in nanoparticles, even after deformation or irradiation [1, 91]. These observations led some researchers to believe that it is not possible for dislocations to exist in nanoparticles. The theoretical basis for this idea is the model proposed by Nieh *et al.* [56] for the IHPE in 3-D materials. This model considers the cases where the equilibrium spacing between dislocations in a pile-up is greater than the grain size. Though this is not technically applicable to single crystalline nanomaterials, the paper by Nieh *et al.* [56] is commonly referenced as the reason why dislocations are impossible in nanoparticles.

In order to understand the aforementioned behavior, this dissertation will consider the gradient in energy experienced by a dislocation present within a nanoparticle, as a function of distance from the surface of the nanoparticle. If the energy gradient is sufficiently large, the dislocation will be spontaneously ejected from the nanoparticle to reduce its elastic energy. This analysis can be also applied to 1-D nanomaterials because the slip plane is bounded on each side by free surfaces, as is the case for nanoparticles.

The model assumes a nanoparticle containing a perfectly straight edge dislocation located across its center (Fig.3.1), before deformation takes place. Subsequently, the model considers the change in Gibbs free energy of the edge dislocation as it moves through the nanoparticle. Upon reaching the nanoparticle's free surface, the dislocation will create discrete steps, which are one Burger's vector in length (Figure 3.1). These steps will increase the particle's surface area and thus, its surface energy. Simultaneously, as segments of the dislocation exit the particle and form steps, the total length of the dislocation within the particle decreases. Thus, the differential expression for the Gibb's free energy of an edge dislocation as it moves through the nanoparticle, assuming constant pressure and temperature, can be expressed as

$$dG = \gamma dA + U_{dis}^{l} dL \tag{3.1}$$

where γ is the surface energy per unit area A of the particle, L is the dislocation line length, and $\mathbf{U_{dis}^{l}}$. is the strain energy stored per unit length of dislocation, given in by

$$U_{dis}^{l} = \frac{b^2\mu}{4\pi(1-\nu)} ln\left(\frac{R}{r_0}\right) \tag{3.2}$$

where b is the Burgers vector, μ is the shear modulus, ν is Poisson's ratio, R is the distance from the dislocation to the free surface, and r_0 is the cut-off radius below which elasticity theory breaks down. The divergence with R shows that the strain energy of the dislocation depends on the size of the crystal, which can be represented by R.

On the basis of equation (3.1) we can calculate the force acting on the dislocation, as a function of dislocation position from the surface of the particles. This can be done by taking the derivative of the Gibbs free energy, expressed by equation (3.1), with respect to x, which represents the distance from the center of the nanoparticle to its surface along the dislocation's glide direction. In a mathematical form, we can write

$$-F = \frac{dG}{dx} = \frac{\gamma dA}{dx} + \frac{d\left(U_{dis}^{l} L\right)}{dx} = \gamma \frac{dA}{dx} + \frac{dL}{dx} U_{dis}^{l} + \frac{dU_{dis}^{l}}{dx} L \tag{3.3}$$

By dividing this force by the length of the dislocation and the dislocation's Burgers vector, the shear stress acting on the dislocation can be obtained, and is given by

$$\sigma_s = -\frac{1}{bL(x)} \left[\gamma \frac{dA}{dx} + \frac{dL}{dx} U_{dis}^{l} + \frac{dU_{dis}^{l}}{dx} L \right] \tag{3.4}$$

It is important to emphasize at this point that σ_S is a spontaneous pseudo-stress that acts on the dislocation due to the nanoscale environment. There are three distinct terms that define this spontaneous stress. They are referred in this dissertation as type I, type II and type III stresses and are given by equation 3.5, 3.6, and 3.7 respectively, in the form

$$\sigma_I = -\frac{1}{bL} \left[\gamma \frac{dA}{dx} \right] \tag{3.5}$$

$$\sigma_{II} = -\frac{1}{bL} \left[\frac{dL}{dx} U_{dis}^{l} \right] \tag{3.6}$$

$$\sigma_{III} = -\frac{1}{b}\left[\frac{dU_{dis}^{l}}{dx}\right] \tag{3.7}$$

Type I stress is associated with changes in the surface area of the particle. Depending on the geometry considered, the motion of a dislocation can either create or destroy surface area. For example, as a dislocation is being ejected at an atomically smooth surface, a surface step of length b is generated. On the other hand, a dislocation nucleating at a surface step will eliminate the same amount of surface area. The surface step created by the ejection of a dislocation at an atomically flat surface is shown by Figure 3.1. This means that Type I stress can either pull or push away a dislocation from a free surface, depending on whether it is creating or eliminating surface area.

Type II stresses (equation 3.6) are caused by changes in the line length of the dislocation. As the dislocation moves through a nanoparticle its line length may change (Figure 3.2). However, the change in line length can either be positive or negative. For instance, a dislocation half-loop nucleating at the surface of a nanoparticle increases in length as it glides through the nanoparticle. On the other hand, if a dislocation glides back to the original nucleation point, the line length will decrease. Type II stress always pulls the nanoparticle towards a free surface that is intersected by the dislocation.

Type III stresses (equation 3.7) are caused by the truncation of the dislocation's stress field by a free surface. Because the strain energy of a dislocation is greatest at its core, the crystal near the dislocation has higher energy than the crystal further away. By approaching a free surface, the dislocation is effectively replacing high energy crystal with low energy crystal, leading to a net drop in strain energy of the dislocation (Figure

3.3). Type III stress is equivalent to an image stress, and it always pulls the dislocation towards the free surface.

Now that the different sources of spontaneous stress have been defined, we may consider three different geometries. First, a straight dislocation in a nanoparticle is discussed. This geometry will provide a basic understanding of the behavior of dislocations in 0-D and 1-D nanomaterials. Next, a dislocation half-loop on the surface of a semi-infinite foil is considered. This geometry will show the general behavior of dislocations nucleating and expanding from a free surface. Finally, a half-loop dislocation nucleating heterogeneously at the surface of a nanoparticle is considered. This geometry is perhaps the most important, but also the most complex. It will combine the previous two geometries and demonstrate how nanoscale dimensions affect a dislocation expanding from a free surface. This geometry will be directly applicable to nanocompression experiments conducted in this dissertation.

Case 1: Straight Edge Dislocation in a Spherical Nanoparticle

In this section, a spherical nanoparticle with a straight edge dislocation across its center is considered. For this geometry, the origins of this dislocation will not be considered. Figure 3.4 schematically illustrates the geometry.

If a perfectly straight edge dislocation located in the center of a spherical nanoparticle glides in the direction of its Burgers vector, there are segments of the dislocation line that exit the nanoparticle. As this occurs, the line length decreases and a surface step created (Figure 3.5). The area of the surface step produced by dislocation motion can be readily found by extending the original surface profile of the nanoparticle along the Burgers vector. This area can be given by

$$A = \mathrm{A_0} + \int \mathrm{L(x-b) - L(x)dx} \tag{3.8}$$

where *A* is total surface area of the nanoparticle, A_o is the initial surface area, and L(x) is the length of the dislocation. For this geometry, L(x) is given by

$$L(x) = 2\sqrt{R^2 - x^2} \tag{3.9}$$

where R is the radius of the nanoparticle. Equations 3.8 and 3.9 can be substituted into equation 3.5 to give the expression for type I stress for this geometry, which can be expressed as

$$\sigma_I = \frac{\gamma}{b}\left[\sqrt{\frac{R^2 - (x-b)^2}{R^2 - x^2}} - 1\right] \tag{3.10}$$

Likewise, equation 3.9 can be substituted into equation 3.6 to obtain an expression for the type II stress, which is given by

$$\sigma_{II} = \frac{\mu b x}{4\pi(1-\nu)(R^2 - x^2)} ln\left(\frac{|x|}{r_0}\right) \tag{3.11}$$

Determining the type III stress is simplified greatly by considering the continuity condition. The continuity condition is an axiom in continuum theory that states that, in a solid, stress and strains are continuous at all points, including the surface. In nanoparticles a dislocation can cause a significant amount of stress at the surface. This means that in order to fulfill the continuity condition, there must be some stress acting on the surface of the nanoparticle. In the case of a free nanoparticle, the applied stresses on the surface are zero. The absence of the stress required to fulfill the equilibrium conditions causes a pseudo-stress that pulls the dislocation to the free surface. This is the source of the image stress. Therefore, we can substitute in equation 3.7 the value of the stress caused by the dislocation at the surface of the nanoparticle. Along the dislocation's slip plane, the stress field of an edge dislocation is given by

$$\tau = \frac{\mu b}{2\pi(1-\nu)x} \tag{3.12}$$

For this geometry, there are two free surfaces, one at x=+R and one at x=-R. Both of these surfaces exert a type III stress on the dislocation. Therefore, two x terms are needed for the type III stress. Thus, the type III stress is given by

$$\sigma_{III} = \frac{\mu b}{4\pi(1-\nu)}\left(\frac{1}{2R-x} - \frac{1}{2R+x}\right) \tag{3.13}$$

The aforementioned equations can be used to generate plots of the spontaneous stress vs. dislocation position for spherical nanoparticles of various sizes. These plots are shown in Figures 3.6a-c for nanoparticles with diameters of 10nm, 50nm and 500nm. Clearly, Figures 3.6a-c show that the total spontaneous stress acting on the dislocation increases as the dislocation approaches the nanoparticles surface.

Case 2: Half-Loop Dislocation in a Semi-Infinite Foil

The stresses acting on a dislocation half-loop, which nucleates on the free surface of a semi-infinite foil is also very important to understand deformation in 0-D and 1-D materials. A semi-infinite foil is defined as a solid that that extends infinitely in the +x, +y, and –y directions. The z-dimension is not relevant to this analysis, because the discontinuous stresses outside of the slip plane do not produce stresses on the slip plane. For this discussion, we will assume that the semi-infinite foil has a free surface at x=0. A schematic diagram of this geometry is shown in Figure 3.7. For this geometry, the effect of an applied stress on dislocation behavior is also considered. The surface area for this geometry is given by

$$A = A_0 \pm 2bx \tag{3.14}$$

where the symbols have the same meaning as before. As the dislocation loop expands, it either creates or destroys surface area, depending on whether the dislocation nucleated on a smooth surface or on a surface step. For this geometry, the line length of the dislocation is given by

$$L(x) = \pi x \tag{3.15}$$

Equations 3.14 and 3.15 can be substituted into equation 3.5 to arrive at an expression for the type I stress in this geometry, which is given by

$$\sigma_I = \frac{\pm 2\gamma}{\pi x} \tag{3.16}$$

where the sign depends on whether surface area is being created or destroyed. Type II stresses can be determined by substituting equations 3.15 and 3.2 into equation 3.6. This results in the following expression

$$\sigma_{II} = \frac{-b\mu \ln\left(\frac{x}{r_0}\right)}{8\pi(1-\nu)} \tag{3.17}$$

Type III stress can be calculated for this geometry, as for the previous geometry. This leads to the expression

$$\sigma_{III} = \frac{-b\mu}{4\pi(1-\nu)x} \tag{3.18}$$

The sum of the spontaneous stresses is shown in Figure 3.8. Note that all the forces are negative, which means that all the forces are pulling the dislocation back towards the free surface. The spontaneous stresses start out very high at the film's surface, but decrease as the dislocation is positioned away from the surface.

Case 3: Half-Loop Dislocation in a Spherical Nanoparticle

In this section we will combine portions from the previous two sections to determine the spontaneous forces acting on a dislocation half loop inside a spherical nanoparticle. This is the most complicated geometry considered so far, and a schematic diagram is presented in Figure 3.9.

Because of the difficult geometry it is easier to write the equations in terms of *t*, which is defined in Figure 3.9 as the distance between the center of the particle and the line perpendicular to the cord defined by the ends of the dislocation half loop. An equation for r in terms of t is given by

$$r(t) = \sqrt{R^2 - t^2} \tag{3.19}$$

Additionally, the equation for L in terms of *t* is given by

$$L(t) = \pi r = \pi\left(\sqrt{R^2 - t^2}\right) \tag{3.20}$$

while an expression for *x* in terms of *t* is given by

$$x(t) = t + r = t + \sqrt{R^2 - t^2} \tag{3.21}$$

Using trigonometry, an equation for the length of the surface step, l can be written as

$$l = Rarcsin\left(\frac{r}{R}\right) = Rarcsin\left(\frac{\sqrt{R^2 - t^2}}{R}\right) \tag{3.22}$$

In addition, the total area of the nanoparticle can be expressed as

$$A(t) = A_0 + bRarcsin\left(\frac{\sqrt{R^2 - t^2}}{R}\right) \tag{3.23}$$

Equation 3.23 can be differentiated with respect to *x* to find the type I stress; albeit this is procedure is less direct than the procedure for the previous examples. The first issue is that the geometry is much easier to express in term of *t* than *x*, but *x* remains the physically significant variable. This difficulty is solved by using the chain rule, from calculus. For this particular geometry, the chain rule can be used as follows

$$\frac{dA}{dx} = \frac{dA}{dt}\frac{dt}{dx} \tag{3.24}$$

where dt/dx is given by

$$\frac{dt}{dx} = {}^{1}\Big/_{\frac{dx}{dt}} = \frac{1}{1 - \frac{t}{\sqrt{R^2 - t^2}}} \tag{3.25}$$

If equation 3.23 is differentiated with respect to *t*, the following expression is obtained

$$\frac{dA}{dt} = \frac{-Rbt}{R\sqrt{R^2 - t^2}} \frac{1}{\sqrt{1 - \frac{R^2 - t^2}{R^2}}} \tag{3.26}$$

Equations 3.26 and 3.25 can be substituted into equation 3.24, which can then be substituted into equation 3.5 to determine the type I stress for this geometry. The type I stress for this geometry is thus given by

$$\sigma_I = \frac{\gamma t}{\sqrt{R^2 - t^2}\left(\sqrt{R^2 - t^2} - t\right)} \left[\frac{1}{\sqrt{1 - \frac{R^2 - t^2}{R^2}}}\right] \tag{3.27}$$

A simple expression can be achieved by substituting equation 3.19 into equation 3.27, which yields

$$\sigma_I = \frac{\gamma t}{r(r - t)} \left[\frac{1}{\sqrt{1 - \frac{R^2 - t^2}{R^2}}}\right] \tag{3.28}$$

The type II stress can be calculated is a similar manner. Equation 3.20 can be differentiated with respect to t to give

$$\frac{dL}{dt} = \frac{-\pi t}{\sqrt{R^2 - t^2}} \tag{3.29}$$

If equation 3.29 and equation 3.25 are substituted into equation 3.6, the following expression for the type II stress is obtained

$$\sigma_{II} = \frac{\mu bt}{4\pi(1-\nu)\left[(R^2-t^2)-t\sqrt{R^2-t^2}\right]} ln\left(\frac{R-\left|t+\sqrt{R^2-t^2}\right|}{R}\right) \tag{3.30}$$

Substituting now equation 3.25 into equation (3.30) leads to a simplified expression given by

$$\sigma_{II} = \frac{\mu bt}{4\pi(1-\nu)[r^2-tr]} ln\left(\frac{R-|t+r|}{R}\right) \tag{3.31}$$

The type III stress is the most simple of the three stresses to calculate in this geometry. The equation for the type III stress for this geometry is very similar in form to equation 3.14, but with a few changes to account for the new geometry. Once again, the two *t* terms in the denominator represent the distances between the dislocation and the two free surfaces at x=±R. The type III stress for this geometry is given by

$$\sigma_{III} = \frac{\mu b}{4\pi(1-\nu)}\left[\frac{1}{R+t+r}-\frac{1}{R-(t+r)}\right] \tag{3.32}$$

Equations 3.28, 3.31, and 3.33 can be combined to determine the spontaneous stress acting on the dislocation as a function of x for spherical nanoparticles with diameters of 20nm and 400nm (Figure 3.10). Figure 3.10 shows that the spontaneous stress on the dislocation starts as negative and then turns positive about two-thirds of the way through the nanoparticle. As expected, the largest spontaneous stresses are near the nanoparticle surface.

3.2.2 Deformation Twinning In Nanoparticles

One of the exciting developments in the field of nanocrystalline metals has been the discovery of novel deformation mechanisms that become active only at small grain or crystal sizes. In this regard, the deformation of high stacking fault energy (SFE) face-centered-cubic (FCC) nanomaterials, such as aluminum (Al), is an especially interesting case. Owing to the fact that Al has a high SFE (140 mJ/m^2), it is widely known that for microcrystalline Al perfect dislocation are prevented from dissociating. As a consequence, partial dislocations, stacking faults and deformation twins are typically absent in microcrystalline Al. Despite these predictions, Chen *et al*. [7] has recently shown high-resolution electron micrographs showing deformation twins in nanocrystalline Al. Furthermore, molecular dynamics simulations of deformation of nanocrystalline Al, by Yamakov *et al*. [60], also give evidence for the formation of deformation twins and stacking faults. Therefore, it seems that the fundamental mechanisms of deformation changes when Al crystals are reduced to the nanoscale.

Beyond this apparent mystery, a more detailed knowledge of deformation behavior in nanoscale materials is also relevant for addressing the nanoindentation of nanostructured pillars [11, 12, 14, 17, 94]. Interesting effects are seen in this length scale, in particular an increase in yield strength and novel plastic–elastic transitions. Evidence of dislocation motion is uniformly witnessed during submicron-compression experiments. In trying to understand these deformation experiments in nanopillars, molecular dynamics simulations have been performed, often showing evidence of Shockley partial dislocations gliding [19, 97, 98].

It is the purpose of this section to offer a plausible model for the increase in occurrence of stacking faults and deformation twins in nanoparticles of high SFE, such as Al. The ideas developed herein also provide an insight into the deformation of any FCC metallic nanoparticles and nanopillars. As a first approach, we will solely consider the case of metallic individual nanoparticles, free of oxides. Bulk nanocrystalline metals will not be considered in this analysis.

Heterogeneous Dislocation Nucleation in an Infinite Particle

Consider a dislocation-free semi-infinite crystal subjected to a large shear stress parallel to one of its slip systems. The shear stress τ acts as a driving force for dislocation nucleation. Although the homogeneous nucleation of perfect and partial dislocations in an infinite particle is conceivable, it is more likely that dislocation nucleation will occur at a pre-existing heterogeneity, such as a surface ledge or a surface without pre-existing steps or ledges. To address either situation, the simplest approach is to consider the nucleation of a half-loop of radius, r, at the heterogeneity. In the case of a surface ledge, the nucleation of the dislocation half-loop will reduce the length of the step, for which the change in Gibbs free energy for dislocation nucleation can be expressed as

$$\Delta G = \pi r W - \frac{\pi}{2} r^2 b_{perfect} \tau - 2r\eta \tag{3.33}$$

where $b_{perfect}$ is the Burgers vector of a perfect dislocation, η is the interfacial energy per unit length of the surface ledge, which is given by $\eta=\Phi b_{perfect}$, and Φ is the solid/vapor interfacial energy. W is the strain energy per unit length of dislocation given by [105]

$$W_{perfect} = \frac{2-\nu}{2(1-\nu)} \frac{\mu b_{perfect}^2}{4\pi} ln\left(\frac{r}{c}\right) \tag{3.34}$$

where ν is Poisson's ratio, μ is the shear modulus and c is the core cut-off parameter. In this case, r refers to the distance between the dislocation line and the particle's surface. Therefore, for the case of a half-loop heterogeneously nucleating on the surface, r is equal to the loop radius. Proximity to the surface of the crystal lowers the energy of the dislocation due to image stress interactions. The corresponding equation for the heterogeneous nucleation of a partial dislocation loop can be given as

$$\Delta G = \pi r W_{partial} - \frac{\pi}{2} r^2 b_{partial} \tau + \frac{\pi}{2} r^2 \gamma - 2r\eta_{partial} \tag{3.35}$$

where b_p is the Burgers vector of a partial dislocation, γ is the stacking fault energy and the other symbols have the same meaning as before. Note that there is no trailing partial; the leading partial moves into the crystal creating stacking fault over the entire area it sweeps. In the case of heterogeneous nucleation at a surface with no pre-existing steps or ledges, the nucleation of a dislocation half-loop involves the formation of a step of magnitude equal to the Burgers vector of the perfect or partial dislocation that nucleated. Thus, in this case, the terms $2r\eta$ and $2r\eta'$ in Equations (3.32) and (3.34) are positive. Equations 3.33 and 3.35 are used to evaluate the Gibbs free energy of nucleation of perfect and partial dislocations in Al and Cu infinite particles at various stresses (Figure 3.11).

Effect of Particle Size on the Heterogeneous Nucleation of Dislocations

If the crystal size is reduced to the nanometer scale, the nucleation of a dislocation half-loop will be increasingly affected by the presence of nearby surfaces. As a consequence, the assumption associated with an infinite crystal size becomes increasingly invalid. Therefore, in the nanoscale regime, it is vital to take into account the effect posed by the nearby free surfaces. In other words, there are image forces acting on the dislocation half-loop. As a crude approximation, the image force per unit length acting on the dislocation loop can be written as

$$\frac{F}{L} = \frac{\mu b^2(2-\nu)}{2\pi x(1-\nu)} \tag{3.36}$$

where x is the distance between the free surface and a unit length of the dislocation half-loop. In general, this force tends to move the dislocation line towards any nearby surface. If the nucleation of a half-dislocation loop occurs at the edge of the nanoparticle (i.e. the nucleation is heterogeneous), two image forces need to be considered: (i) the image force working against the growth of the loop associated with the surface where the dislocation nucleates (discussed above and represented by W and W_p for perfect and partial dislocation half-loops, respectively) and (ii) the image force associated with the surface away from the dislocation line, which attracts the half-loop towards the surface. In the case of nucleation at a surface ledge, the equations analogous to (3.32) and (3.34) are

$$\Delta G = \pi r W - \frac{\pi}{2} r^2 b\tau - 2r\eta - \frac{\mu b^2 (2-\nu)}{2\pi(1-\nu)} ln\left(\frac{R-r}{R}\right) \tag{3.37}$$

$$\Delta G = \pi r W_p - \frac{\pi}{2} r^2 b_p \tau + \frac{\pi}{2} r^2 \gamma - 2r\eta_p - \frac{\mu b^2 (2-\nu)}{2\pi(1-\nu)} ln\left(\frac{R-r}{R}\right) \tag{3.38}$$

As before, for the case of heterogeneous nucleation at a singular surface, the terms $2r\eta$ and $2r\eta'$ in Equations (3.37) and (3.38), respectively are positive. Although Equations (3.33-3.38) must be regarded as approximate solutions, they do lead to two conclusions: (i) for very small dislocation loop radius, the strain energy term dominates. As a result, a partial half-loop, with its lower strain energy, has a preferred advantage for nucleation and (ii) image forces present in nanoparticles reduce the energy barrier for nucleation of dislocations in surface ledges, in particular partial dislocations, while increasing the barrier for heterogeneous nucleation at particle surfaces. Equations 3.37 and 3.38 are used to evaluate the Gibbs free energy of nucleation of perfect and partial dislocations in Al and Cu particles with various sizes at different stresses (Figures 3.12, 3.13). By finding the maxima of Figures 3.12 and 3.13, the critical sizes for dislocation loops nucleating in Al and Cu nanoparticles are found (Figure 3.14).

3.3 *IN-SITU* TEM NANOINDENTATION EXPERIMENTS

3.3.1 Materials

Ag nanoparticles, provided by Novacentrix™ with a nominal size of 35nm, were used for the nanoindentation experiments for two reasons: 1) Ag does not readily form a native oxide. The absence of an oxide layer is very important because it can greatly affect the overall mechanical properties, particularly at the nanoscale, where the thickness of an oxide layer becomes a significant fraction of the overall sample dimensions. 2) Ag has an FCC structure. As most of the previous experiments and simulations done on the nanocompression of metals have focused on FCC materials, the use of Ag allows for a direct comparison between the experiments presented in this chapter and the results available in literature.

3.3.2 Methods

Sample Preparation

The Ag nanoparticles were affixed to a metal wire by dry dipping. Both W and Cu wires were used in dry dipping. In dry dipping, the wire is held by tweezers and dipped directly into a dry powder of nanoparticles. During this process, the particles adhere to the wire due to Van der Waals forces. The wire supporting the Ag powder is then inserted into the Nanofactory instruments holder (Figure 3.15), which is located opposite to the probe.

Experimental Equipment

Three different TEMs and two different sample holders were used for the experiments. The diffraction contrast experiments were done in a FEI Technai X-Twin 200 keV TEM equipped with an analytical pole piece and a Nanofactory Instruments TEM-Nanoindenter^{TM} sample holder. This instrument was used because the TEM-Nanoindenter^{TM} is too thick to be used in conjunction with an ultra high resolution pole piece (URP).

The TEM-Nanoindenter^{TM} sample holder has many attractive features for *in-situ* nanoindentation, including nano-Newton level force measurements. However, the most important features of this holder for the nanoindentation experiments are the diamond probe and sub-nanometer position controls. Force measurements were not taken during the experiments because the non-ideal shapes of the indenter and nanoparticle would make accurate estimates of the stress very difficult to determine, even if the forces were known.

The non-corrected phase contrast experiments were conducted in a JEOL 2010F 200 keV TEM equipped with an URP and a Nanofactory Instruments STM-TEM^{TM} specimen holder. The STM-TEM^{TM} holder is similar to the TEM-Nanoindenter^{TM} holder, except for the fact that does not have force measurement capabilities and it is thinner than the TEM-Nanoindenter^{TM}, thereby fitting an URP. The TEM-STM^{TM} holder uses a W wire instead of the diamond tip used by the Nanoindenter^{TM} (Figure 3.15) holder.

Probes for the specimen holder were made by electropolishing W wire. The electropolishing geometry is shown schematically in Figure 3.16. A tungsten wire was suspended vertically in a dish of KOH with a loop of gold wire in it. The tip of the wire was protected with a cap of nail polish and a DC current was run through the system. Close attention was paid to the nail polish cap, so that when the cap fell off, the current was immediately stopped. Subsequently, the probe was carefully removed.

Finally, aberration-corrected *in-situ* TEM nanoindentation experiments were conducted on a double-corrected JEMS 2200 200 keV microscope at Brookhaven National Laboratory. The JEMS 2200 microscope is equipped with a URP and therefore can accommodate the STM-TEM holder. Additionally, for the aberration-corrected nanocompression experiments, tungsten probes were purchased from Zyvex Instruments. The nanocompression experiments were conducted in TEM mode.

Experimental Procedure for In-situ Diffraction Contrast TEM Nanoindentation

For the diffraction contrast *in-situ* nanoindentation experiment, the transmitted beam was selected using the smallest available aperture. The probe and the sample were brought close to one another and the image wobbler was used to make sure the nanoparticle and the indenter were both in the focal plane. This is done by first making sure the nanoparticle is in focus using the TEM stage z-axis control and then using the probe z-axis controls to make sure the probe is in focus as well. Because the sample and the probe are both in the focal plane they are expected to make contact if the tip of the probe is translated toward the nanoparticle.

Upon contact, no effort was taken to measure the forces of contact or the strain rate, for the reasons that were discussed above. Instead, an image was captured on the CCD camera. The strain on the nanoparticle was incrementally increased by translating the probe into the sample. After each increment, an image was captured on the CCD camera. After the particle had undergone a significant amount of strain, the probe was translated away from the sample and an image was captured after the probe and the sample were no longer in contact.

Experimental Procedure for In-situ Phase Contrast TEM Nanoindentation

The probe and sample alignment procedure is identical to the phase contrast experiments. However, an additional concern for phase contrast nanoindentation experiments is the size of the particles. If the particle is too thick, the phase object assumption for high resolution imaging is violated, and imaging becomes more complex. Therefore, particles with diameter of less than 20nm are ideal.

The procedure for the actual nanoindentation in phase contrast mode is also very similar to the procedure for the diffraction contrast experiments. However, keeping the nanoparticle in focus is more important in the phase contrast experiment. After each strain increment the particle was re-focused and several images were taken, to ensure that an image at Scherzer defocus was captured. The probe was translated away from the sample following the phase contrast experiment, similar to the procedure used for the diffraction contrast experiment.

3.3.3 Experimental Results

In-situ Diffraction Contrast TEM Nanoindentation

First, the sample and the indenter were bought into mutual focus, and an image was captured (Figure 3.17). After the probe and the sample were brought into focus, the indenter was translated towards the sample until contact was made. At this point, another image was captured (Figure 3.18). Clearly, a contrast band appears in the nanoparticle (labeled A). Due to the ambiguities involved in diffraction contrast imaging, the source of the contrast band is unclear without more in-depth analysis. This analysis will be presented later in this chapter.

After the initial strain was applied, the probe was translated further into the sample to increase the strain on the nanoparticle, while another image was captured (Figure 3.19). Here, two contrast bands can be seen (labeled B and C). At this point, it is unclear if one of these contrast bands is A (shown in Figure 3.18), shifted to a new position, or if they are entirely new contrast bands. It was not possible to track the motion of the contrast bands while the strain was increased.

The probe was translated further into the sample, thereby increasing the applied strain, while another image was captured (Figure 3.20). Three contrast bands are seen in Figure 3.20, labeled E, F and G. Again, it is unclear if bands A, B or C moved to produce E, F or G, or if E, F, and G are entirely new contrast bands.

The strain on the nanoparticle was increased again, by continuing to translate the probe into the particle and another image was recorded (Figure 3.21). Three contrast bands labeled H, I and J can be seen. As before, the relationship of these new contrast bands to the contrast bands in the previous images is unknown.

After Figure 3.21 was recorded, the applied strain on the particle was removed by translating the probe away from the sample until there was no longer contact between the indenter and the sample (Figure 3.22). Under these conditions, there are no visible contrast bands in the nanoparticle.

The sequence of images shown in Figures 3.17-3.22 is compiled in Figure 3.23 to monitor the progression of the nanoindentation process. Though the motion of the contrast bands was not recorded, it appears from Figure 3.23 that the contrast bands originate at the point of contact between the nanoparticle and the indenter, and radiate outward.

Uncorrected In-situ Phase Contrast Nanoindentation

A 10nm Ag nanoparticle on a Cu support was selected for the uncorrected phase contrast nanoindentation experiments. The W probe and the Ag sample were brought into mutual focus several nanometers away from one another. Figure 3.24 shows the positions of the W probe, Ag sample and Cu support before nanoindentation. As shown in Figure 3.24, the tip of the W probe is quite thin, as evident by the presence of lattice fringes. Also, (111) lattice fringes corresponding to the Ag nanoparticle are readily visible, as confirmed by the fast Fourier transform (FFT) (inset in Figure 3.24). The streaks along the (111) direction in the FFT reveal the presence of a twin in the nanoparticle. This is better observed in Figure 3.25, which is a digitally magnified version of Figure 3.24.

Subsequently, the probe was translated towards the sample until contact was made. The image was re-focused and a micrograph was recorded (Figure 3.26). A digitally magnified version of the same image is presented in Figure 3.27, which shows a terminating lattice plane, highlighted in the inset image. This is clear evidence of the presence of a dislocation in the nanoparticle.

The strain on the nanoparticle was then incrementally increased by translating the probe further into the sample. At this point, the image was brought into focus again and another image was recorded (Figure 3.28). A digitally magnified version of this image is presented in Figure 3.29, which now shows two lattice planes terminating inside the crystal (highlighted in the inset image). Because of the overlap between the probe and the sample, a more detailed analysis is needed to determine if the terminating planes are caused by the presence of dislocations. This issue will be addressed in later in this chapter.

Subsequently, the W probe was translated away from the sample, such that the probe was no longer in contact with the nanoparticle. At this point, the image was focused and another micrograph was captured (Figure 3.30). A digitally magnified version of Figure 3.30 is presented in Figure 3.31. No terminating lattice planes are readily apparent.

Aberration-Corrected In-situ Phase Contrast Nanoindentation

A 17nm Ag nanoparticle was selected for aberration-corrected *in-situ* phase contrast nanocompression. This nanoparticle is shown in Figure 3.32. However, examination of Figure 3.32 reveals that there are actually two particles in the image. The rightmost particle was selected for compression due to its proximity to the probe. It will be referred to as the sample for the rest of this section. As the presence of the second particle complicates the image in the region where the two particles overlap, care is taken not to draw conclusions from those overlapping regions.

Figure 3.33 show a higher resolution image of the nanoparticle. The use of an aberration-corrected TEM greatly decreases the amount of surface delocalization that occurs compared to an uncorrected TEM, thereby allowing a better observation of the surface structure of the nanoparticle. A careful examination of Figures 3.32 and 3.33 shows that the lattice planes are continuous throughout the nanoparticle. This implies that there are no dislocations in the nanoparticle in its pristine state.

After careful focusing the sample and the probe, the latter was brought into contact with the Ag nanoparticle. An image was taken soon after contact (Figure 3.34). A digitally magnified image based on Figure 3.34 is shown in Figure 3.35. As shown in these two figures, the lattice fringes are continuous in the region where there is no particle overlapping, implying a lack of dislocations.

The probe was translated further towards the sample to increase the strain on the nanoparticle (Figure 3.36). A careful examination of Figure 3.36 indicates the presence of lattice fringes that terminate inside the nanoparticle, corresponding to two dislocations. In Figures 3.37 and 3.38, the regions of the nanoparticle containing the dislocations are highlighted and digitally magnified.

The strain was increased again, so that further changes in the microstructure could be observed. Subsequently, another image was captured (Figure 3.39). A digitally magnified version of the highlighted area is shown in Figure 3.40. The highlighted lattice fringes in figure 3.40 indicate the presence of a dislocation.

The strain was decreased by translating the probe away from the sample in order to examine the nanoparticles in a relaxed state after deformation (Figure 3.41). After the strain is removed the lattice planes of the sample show good registry, indicating the absence of dislocations. Additionally, the first monolayer of the nanoparticle increases in length between Figures 3.33 and 3.41, indicating that plastic deformation occurred.

3.4 DISCUSSION

3.4.1 Dislocation Instability in 0-D and 1-D Nanomaterials

Figure 3.6 show the spontaneous stress acting on a straight edge dislocation, present in a spherical nanoparticle. As the particle size is decreased, the spontaneous stress becomes greater that the yield stress at lower values of x. This indicates that the stability of dislocations decreases as the nanoparticles size decreases. It is important to note that the critically resolved shear stress for Ag is 0.05MPa [120]. This is lower than the spontaneous stress on the nanoparticles in Figure 3.6. This indicates that, in the absence of defects, dislocations are not stable in Ag particles. Figure 3.6 also shows that, for small nanoparticles, type II and type III stresses are close to one another in magnitude. However, this is an ideal configuration.

A more realistic representation is to consider the nucleation of a dislocation half-loop at a free surface of an infinite sample. The spontaneous stresses on a dislocation half loop in a semi-infinite foil are shown in Figure 3.8. Two curves are shown - one related with the creation of a surface step and the other one associated with the elimination of a surface step. The values of the two lines are fairly similar to one another, which imply that the type I stress is low compared to types II and III stresses for this material and geometry. The values shown in Figure 3.8 represent the stresses that must be overcome by the applied stress to nucleate and propagate a dislocation through a semi-infinite foil. In other words, a positive stress with a magnitude that is greater than the spontaneous stress is required to increase the size of the dislocation loop.

For a dislocation loop with radius zero (r=0), the applied stress can be thought of as the stress required to nucleate the dislocation at the free surface. It is important to notice that this is the highest stress required at any point in the foil. This means that if a constant stress high enough to cause dislocation nucleation is considered, a dislocation is expected to nucleate and glide away from the nucleation site. On the other hand, if a constant displacement is considered, large enough to induce enough stress to nucleate a dislocation, the expected behavior will be very different. In this case, as the dislocation glides, it accommodates the applied stress and strain that are causing its motion. Eventually, the strain is no longer enough to cause sufficient stress for the dislocation to continue gliding. At this point the dislocation will stop moving. As long as the initial displacement is held constant, the dislocation is expected to remain stable and stationary. In addition, if the indenter is removed, the dislocation will be subjected to a large spontaneous stress pulling it towards the surface of the semi-infinite foil. If the dislocation is somewhat close to the free surface, this stress is typically larger than the stress required to initiate glide. Therefore, the dislocation would move back to the free surface and annihilate there. This is an important result, because it indicates that dislocations can behave reversibly in certa*in-situ*ations. Furthermore, it implies that to use this reversible behavior as a way of distinguishing between bend contours and dislocations [104] is not appropriate because for some nanoparticle geometries, both dislocations and bend contours act reversibly.

Let us now address the spontaneous stresses acting on a dislocation half-loop present within a finite nanoparticle (Fig. 3.10). The results are somewhat similar to those exhibited by the semi-infinite foil (shown in Figure 3.8), except for the presence of positive stresses near the nanoparticle's free surface at x=+R. As the dislocation approaches the free surface at x=+R, the type III stress from the image force becomes sufficient to pull it to the surface where it is annihilated. It is instructive to consider the behavior of a half loop dislocation in a spherical nanoparticle under constant stress and constant strain. As in the case of the semi-infinite foil, the required stress for the dislocation loop to glide is highest at the surface. Therefore, if the constant stress is large enough to nucleate a dislocation, the dislocation will continue to glide across the nanoparticle, all the way to the other surface, and will be annihilated at the x=+R surface.

For the case of a constant displacement, the situation is less straightforward. In this case, the behavior of the dislocation depends on the magnitude of the displacement. There are three ranges, which are important to discuss: 1) the displacement is too small to nucleate a dislocation. In this case, the material responds elastically and no dislocations are generated. 2) The displacement is high enough to nucleate a dislocation, but not enough displacement to cause the dislocation to glide past the point where the spontaneous stresses become positive. In this case a dislocation is nucleated and glides until it accommodates the applied strain to the point were the stress on the dislocation is no longer sufficient to sustain glide. 3) The displacement is large enough to cause the dislocation to glide into the range where the surface of the nanoparticle, opposite to the surface where dislocation nucleation took place starts to dominate the total spontaneous stress. When this occurs, the spontaneous stress pulls the dislocation in the same direction as the applied stress. This causes the dislocation to become unstable, leading to its ejection towards the nanoparticle surface, opposite to where the dislocation nucleated.

In this fashion, the spontaneous ejection of dislocations can lower the stress, possibly leading to pop-in effects seen by some researchers [104].

Figure 3.10 also shows that the dominant spontaneous stress changes as the dislocation half-loop’s position changes. The figure shows that, very close to the surfaces, the type III stress dominates, but for much of nanoparticle it is the type II stress that is dominant.

On the basis of the above discussion on the behavior of dislocations in 0-D nanomaterials, can we now also answer how do dislocations behave in single-crystal 1-D nanomaterials? This issue can be easily addressed. The theoretical model and all three of the geometries considered above can be adapted to nanowires and nanopillars by changing the profile of the slip plane that is considered. For instance, if the indentation in a cylindrical nanopillar is considered, and the slip plane makes an angle of 45° with the normal of the cylinder, then the shape of the slip plane will be given by the cylindrical section of a plane intersecting the cylinder at 45°. If this profile is used instead of the circle used in case 1 and case 3 from section 3.2.1, then the spontaneous stresses for a cylindrical nanopi1lar can be found.

3.4.2 Deformation Twinning in 0-D and 1-D Nanomaterials

Calculations on the energy required to nucleate heterogeneously a perfect and a partial half-loop of various loop sizes (Equations 3.34 and 3.36) for infinite size particles were performed for the FCC metals Al and Cu. The material constants used for the calculations are given in Table 3.1. For the perfect and partial dislocations, a/2<110> and a/6<112> were used, respectively. The results of these calculations are shown in Figure 3.11 for two levels of applied stress, namely τ =800MPa and τ =1GPa. This range of stresses is selected because of its significance for mechanical tests and computer simulations.

Figure 3.11 considers a semi-infinite crystal that has a free surface but extends infinitely in the other direction. Figure 3.11 shows that, for a particular applied stress, perfect dislocation half-loops are more easily nucleated in Al than in Cu in this semi-infinite geometry. This trend is shown by the smaller critical loop radius and by the lower critical Gibbs free energy of nucleation in Al (Figure 3.11c and d) than in Cu (Figure 3.11a and b). For higher applied stresses, the critical loop radius and the critical Gibbs free energy of nucleation decreases for both metals, but the trend is conserved. An interesting result from these calculations regards the behavior of partial dislocation half-loops. As depicted in Figure 3.11a, equilibrium partial dislocation half-loops are unstable in aluminum for applied stresses of 800MPa. This is a consequence of the fact that Al has high-stacking fault energy and thus, partial dislocation loops collapse before reaching a critical size.

However, an increase in the stress level from 800MPa to 1GPa (Figure 3.11b), facilitates and enables the nucleation of partial dislocation loops with a critical loop radius r_c=17nm. Despite this fact, the nucleation of partial dislocation loops in Al is still less likely to occur than the nucleation of perfect dislocation loops, as confirmed by the smaller critical perfect dislocation loop radius and the lower Gibbs free energy of nucleation for perfect dislocations (Figure 3.9c and d). In contrast to the behavior of Al, the nucleation of partial dislocation loops in Cu, for stresses of 800 MPa, is likely to occur (Figure 3.11a). This is a direct result of the lower stacking fault energy of Cu. At 1 GPa, the critical radius for nucleation of partial and perfect dislocation loops in Cu is practically identical.

Let us now consider the effect of two free surfaces on the energy required to nucleate a perfect and a partial dislocation half-loop as a function of loop size and nanoparticle size. The calculations were performed for the FCC metals Al and Cu, using the same physical parameters described in the previous section and using Equations 3.38 and 3.39. Figures 3.12 and 3.13 show the results for nanoparticles of Al and Cu with sizes of 50, 25 and 10 nm, for applied stresses of 800MPa and 1 GPa, respectively. For both materials, partial dislocations nucleate more readily in smaller nanoparticles. Figures 3.12 and 3.13 also show that partial dislocation loops are much more readily nucleated in Cu than in Al for both regimes of stresses. A very different behavior is observed for the perfect dislocation loops. First, the barrier for nucleation of perfect dislocation loops in Al and Cu does not seem to change with reducing the particle size from 50 to 10 nm. In addition, the nucleation of perfect dislocation loops seem to occur more readily in nanoparticles of Al rather than Cu (Figures 3.12 and 3.13), a tendency observed earlier for semi-infinite size particles (Figure 3.11).

From all these calculations, the most striking result is associated with the metal Al. As shown in Figure 3.13, partial dislocation half-loops are unstable in large size particles. However, for nanoscale particles the critical dislocation radii and critical Gibbs free energy for partial dislocation loops to nucleate are significantly higher (Figure 3.12). This effect is more clearly seen in Figure 3.14, which shows the activation energy for nucleation in Cu and Al for the two levels of stress considered before. For both metals, the influence of downscaling particle size is to favor the nucleation of perfect and partial dislocations and reduce the difference in activation energy for nucleation between partial and perfect dislocations. For the case of aluminum the latter effect is very significant. While for large particle sizes, partial dislocations are unlikely to occur due to the high-activation energies required, for nanoparticles the activation energy for the nucleation of partial dislocations is substantially reduced allowing these defects to compete with the nucleation of perfect dislocations.

Although these calculations suggest that perfect dislocations should be more probable than partial dislocations in Al, any partials that do form are more likely to be noticed during TEM examinations. If a perfect loop is nucleated in a nanoparticle, it is very likely to move to a free surface where it will leave, at most, a step on the surface and remain effectively absent by conventional post-mortem TEM techniques. However, if a partial loop nucleates and sweeps across the crystal, it leaves behind a stacking fault that will be visible in TEM images. Once a single stacking fault is created, a constant stress is likely to nucleate (i) trailing partials or (ii) partials on adjacent planes. If a trailing partial nucleates, it will sweep the entire crystal and eliminate the stacking fault. On the other hand, partial dislocations on adjacent planes are likely to result in the growth of deformation twins. All this implies that if a polycrystalline body is deformed and then observed in a TEM, a few grains may be observed to contain stacking faults or twins, even though many more grains were actually deformed by the passage of perfect dislocations. This may explain the results of Chen *et al*. [7] and other researchers who have occasionally observed faults or twins in isolated grains within nanocrystalline aluminum.

The model developed above also provides significant insight into the behavior of materials during nanoindentation. In particular, molecular dynamics simulations commonly show the formation of Shockley partial dislocations during the nanoindentation process [19, 97, 98]. However, due to the intense computational requirements of MD simulation, the nanopillars simulated are much smaller than the ones tested. According to the model presented in this dissertation, these MD simulations seem to be correct, leading to the conclusion that partial dislocations are likely to occur for sample sizes used in the MD simulation and unlikely to occur for larger sample sizes used for mechanical testing.

Finally, it is important to emphasize that the calculations presented here are based on simplified models and cannot be expected to be truly quantitative. Simplifications include idealized geometries, continuum dislocation theory, and equilibrium energies. By simplifying the problem, it has been possible to identify several essential features and trends associated with dislocation nucleation and consequent plastic deformation of nanocrystalline metals.

3.4.3 TEM Nanoindentation Experiments

To further support the hypodissertation on dislocation instability and to test the analytical models developed earlier in this chapter, two types of TEM nanoindentation experiments were done, one using diffraction contrast and the other using phase contrast. The goal of these experiments was to induce dislocations in single crystal nanoparticles and observe their behavior *in-situ*. Specifically, we wanted to determine a) whether dislocations were able to nucleate in nanoparticles subjected to an applied stress and b) whether nucleated dislocations would be stable after the strain was removed.

Diffraction Contrast Experiment

The results of the diffraction contrast experiments were shown earlier in section 3.3.3. In order to understand these experiments it is crucial to determine the cause of the contrast bands, shown in Figures 3.18-3.21.

In diffraction contrast TEM, contrast bands can be caused by four different mechanisms, namely thickness fringes, stress contours, bend contours, and dislocations. The first three are artifacts based on the fact that elastic strains change the diffraction properties of the crystal lattice. Although some of these artifacts could be ruled out by setting the appropriate conditions in the TEM, the delicate nature of the experimental setup used in this dissertation did not allow such a procedure. In particular, it was not possible to tilt the sample, such that images of the dislocation under various g-conditions could be taken. The reason for this was that tilting caused far too much mechanical vibration in the instrument, which could destroy the probe or the sample, and/or translate the sample from the experimental area.

On this basis, each of the possible artifacts must be investigated and ruled out before it is possible to confirm the presence of dislocations. Let us start with the effect caused by thickness fringes, which are due to changes in the crystal thickness. Figure 3.42 shows a schematic diagram of how thickness fringes are formed. The fraction of electrons diverted to any reflection g is a function of the thickness of the sample. If the sample changes in thickness, changes in the fraction of electrons reflected to g can lead to bright-dark-bright contrast variations. This transition is characterized by the extinction length, which for g=111 in Ag at 200 keV is 35nm. This means that there is a change in thickness of 35nm for every contrast band seen. However, Figures 3.20 and 3.21 show three coexistent contrast bands within the nanoparticle. This requires a nanoparticle of at least 105nm thick. The particle tested in the diffraction contrast experiment was only 50nm in diameter, which confirms that thickness fringes could not be the cause of the contrast bands seen in the diffraction contrast experiment.

The second possibility for the presence of the contrast bands are stress contours caused by variations in spacing between planes due to deformation of these planes. For example, if a crystal is being compressed normal to the (111) plane, and the (111) reflection was nearly excited, the (111) reflection can become strongly excited when the crystal is compressively strained. This can happen under relatively small strains. However, to excite the next co-linear reflection, namely the (222) reflection, the particle would need to undergo a 50% elastic strain, which is not possible for a metal. Therefore, the existence of stress contours as the cause of the contrast bands can be ruled out.

We are now left with the possible effect caused by bend contours, which may occur when elastic bending of the lattice planes changes the diffraction conditions of the sample. A schematic diagram showing how bending contours are formed is given in Figure 3.43. Bending of the sample changes the angles between the bended planes and the electron beam, causing planes to go in and out of the Bragg condition. This causes bands of dark and light contrast. To calculate the total deflection required to produce three bend contours, a simple calculation can be done. Because the (111) planes of an FCC material have the smallest Bragg angle, bending of the line normal to a (111) plane is the optimal case for bend contour formation. It is assumed that this is the case. For a material to produce three contours, it must be bent through the Bragg diffraction angle three times. This angle can be calculated using Bragg's law, given by

$$\lambda n = dsin\theta \tag{3.39}$$

where n is an integer, λ is the wavelength, d is the planar spacing and θ is diffraction angle. Considering the (111) plane of Ag and an accelerating voltage of 200 keV, the amount of bending was found to be ~27.5mrad. To calculate the forces required to form bend contours caused by a 27.5 mrad bending, a cantilevered sphere was considered. However, as solving for the bending of a sphere analytically is difficult, a numerical solution was used. The sphere was approximated by a series of disks and the individual deflections were summed to determine the sphere's total deflection. A schematic diagram is shown in Figure 3.44. Mathematically, this can be expressed by a series of equations, given by

$$h(x) = \sqrt{\mathrm{R}^2 - (\mathrm{x} - \mathrm{R})^2} \tag{3.40}$$

$$I_{disk}(h) = \frac{\pi h^4}{4} \tag{3.41}$$

$$\theta_{disk} = \frac{Ft^2}{2EI} \tag{3.42}$$

$$\theta_{sphere} = \sum_{i=1}^{i=2R/t} \theta_{disk}\left(it - {}^{1}\!/_{2}\right) \tag{3.43}$$

where h(x) is the height (radius) of the disks, R is the nanoparticles radius and x is the distance along the central axis of the nanoparticle. Equation 3.41 gives the moment of inertia, I of a single disk. Equation 3.42 expresses the angle of deflection for a disk, where t is the thickness of the disk, F is the force on the disk and E is the modulus of elasticity. Finally, equation 3.43 gives the total angle of deflection for the sphere. The variable θ_{disk} is the amount of bending in a single disk and the variable i represents the number of disks.

Equation 3.44 was used to calculate the applied bending force required to cause three bend contours in a 50 nm nanoparticle. The result is ~890nN, which corresponds to a stress of ~0.45GPa. The direction of the stress causing the bending is normal to the plane of the TEM images, otherwise it would not change the angle between the (111) planes and the beam.

The required stress of 0.45GPa is high, but not completely unreasonable. The stress applied by the probe can be thought of as a combination of two components. One component is in the plane of the image and does not contribute to bend contours because it does not change the angle between the electron beam and the (111) planes. The second component is normal to the image plane and this contributes to the bend contours by bending the normal direction of the (111) planes causing changes in the angle between the planes and the electron beam.

The misorientation angle between these stresses can be calculated from the magnitudes of the two components. The stress applied is assumed to be between 2 and 6 GPa based on previous results of nanocompression experiments performed on Ag nanopillars [93]. For stresses in this range, the angle of misorientation is within 4-13°.

Assuming dislocation nucleation to occur at ~2.7GPa, as was seen in section 3.2.1, this means that the angle of misorientation should be closer to 13° for the three bend contours to form before a dislocation was nucleated. This misorientation angle is high, but still possible.

An entirely separate but important issue concerning the formation of bend contours in this experiment is the particles mechanical stability while it is subjected to the bending force. A large out of plane stress would be expected to cause the nanoparticle to slide or roll across the support. For our bending calculations, we have assumed that the nanoparticle was fixed firmly to the support at the point marked by x in Figure 3.44. However, this is not necessarily the case. Assuming Van der Waals bonding to exist between the nanoparticle and the support, the strength of the Van der Waals force can be calculated according to [106]:

$$F_{VdW} = -\frac{AR}{6D} \tag{3.45}$$

where A is the Hamaker constant, R is the radius of the nanoparticle and D is the separation between the nanoparticle and the support. Since the support and the nanoparticle are considered to be in contact, D is approximated to 2Å. The value of the Hamaker constant for condensed phases are in the range of 0.4-4 10^{-19}J. This gives Van der Waals forces within a range of 0.83-8.3 10^{-19}N, which correspond to stresses of 0.42-0.16 Pa. This calculation makes it very clear that Van der Waals bonds holding the particle to the support will be unable to withstand the bending forces required to form the bend contours. This finding was confirmed during some of the experiments. The probe was translated towards the support and moved laterally, causing the nanoparticle to move sidewise across the support.

These considerations imply that the formation of bending contours by the cantilever beam method is unlikely. However, it is possible to imagine a situation where the nanoparticle was somehow wedged in a ditch in the support, or something similar. Additionally, bend contours could have also arisen from a local rotation of the nanoparticle lattice caused by strain due to nanoindentation. In this case, the nanoindentation procedure has a similar geometry to a Hertzian contact. In Hertzian contact, the material experiences a highly anisotropic stress state that could lead to rotation of the solid element in the nanoparticle. The rotation of these solid elements could change their diffraction conditions and cause band contrast in the images. While elasticity theory can be used to calculate the rotations of individual parts of a solid, this requires a complete solution for the displacements in the solid. Unfortunately, Hertzian contact theory does not have a closed form analytical solution. The investigation of bending contours caused by this mechanism would require extensive original computational modeling. Calculations of this type are outside the scope of the dissertation.

Uncorrected Phase Contrast Experiment

Phase contrast nanoindentation experiments were done to eliminate the ambiguities associated with the diffraction contrast experiments shown earlier in this chapter. The results of these uncorrected phase contrast experiment are shown in Figures 3.24, 3.26, 3.28, and 3.30. Though the dislocations are readily apparent in the images, additional analysis is necessary. Because the indenter was also electron transparent, it is first necessary to confirm that the terminating lattice fringes seen in the micrographs are not due to Moiré fringes. This was done by Fourier filtering using the Gatan Digital Micrograph software. Two types of Fourier filtered images were created. One was created using only the prominent (111) spots from the image, while the other was made using a ring with a radius equal to g_{111}. In each case, special care was taken to exclude the g vector from the W probe. The results of Fourier filtering are shown in Figures 3.46-3.50.

The Fourier filtering images shows clearly that the terminating lattice fringes from Figures 3.46 and 3.47 are not Moiré fringes caused by the W indenter. This is an unambiguous confirmation of the presence of dislocations in a nanoparticle. The results of Fourier filtering of Figure 3.29 are a little more difficult to interpret. If the lattice planes shown in Figure 3.48 are traced from right to left, it can easily be seen that two of the planes terminate inside the crystal, indicating the presence of dislocations. However, if the planes neighboring these apparent dislocations are followed farther, a new plane can be seen. These are shown by the insets in 3.48 and 3.49. This may indicate that the apparent dislocations are actually continuous planes and that their apparent termination was caused by overlap with the W probe.

Because of this continuing ambiguity, a more advanced Fourier filtering process is used. In this procedure, a Fourier filtered image was produced from Figure 3.29 using an array of FFT spots (Figure 3.50). The rightmost apparent dislocation appears clearly in Figure 3.50, indicating the presence of an actual dislocation. The leftmost apparent dislocation from Figure 3.29 is associated with the terminating half plane in the opposite direction in the filtered image presented in Figure 3.50. This could indicate the presence of a third dislocation, but it could also indicate that the crystallographic plane associated with the leftmost terminating lattice fringe is continuous, and that the terminating lattice fringe seen in the image is an artifact.

Now that that the presence of dislocations has been confirmed in the nanoparticles subjected to nanoindentation, it is necessary to discuss the characteristics of these dislocations. Let us start by looking into (111) interplanar spacing seen in Figure 3.27 and Figure 3.29, which is 0.236nm. This would imply a Burgers vector of the type a/2(111) for the dislocations observed. However, FCC metals, such as silver are known to have Burgers vectors of type a/2(110) for perfect edge dislocations and a/6(112) for partial dislocations. What is the reason for this discrepancy? First, it is important to consider that in FCC crystals the (110) reflections violate the extinction conditions. Therefore, (110) fringes are not seen in FCC crystals. How would the a/2(110) Burgers vector be expressed in a FCC crystal? Figure 3.51 shows how an a/2(110) Burgers vector might affect (111) lattice fringes.

If a strong set of (111) fringes is imaged, the larger a/2(110) Burgers vector will be projected onto the (111) fringes. A terminating fringe will still be seen because the (110) interplanar spacing is larger than the (111) spacing. However, there will be several out of plane distortions associated with the terminating (111) fringe. Most notably, the (111) planes adjacent to the terminating (111) planes will be deformed in an asymmetric manner. To better understand this situation, let us define the following: the points where the two lattice fringes adjacent to the terminating lattice fringe begin to move towards one another will be referred to as the lattice fringe’s elbow for the purposes of this dissertation. These elbows are indicated in Figures 3.27 and 3.29. Thus, if the Burgers vector of the dislocation was on the (111) planes parallel to the electron beam (111 lattice fringes observed in the images), the elbows would be expected to be symmetric around the terminating lattice fringe. As shown in Figure 3.27 and Figure 3.29, this is clearly not the case. In fact, a close inspection of the dislocations in Figures 3.27 and 3.29 indicate that the deformed lattice fringes immediately around the dislocation core are not symmetrical.

The intersection of the slip plane and the image plane can be found by drawing a straight line through the dislocation core and the elbows of both neighboring lattice fringes. Consider the elbows to be the points where the lattice fringes begin to bend considerably. This is done for figures 3.27 and 3.29 and the results are shown in figures 3.52 and 3.53. Figures 3.52 and 3.53 clearly show that the slip planes of the dislocations are not at a right angle with the lattice fringes. Furthermore, the slip plane in the first image is at a different orientation with the slip planes of the dislocations in the second image.

Because the nanoindenter is shown in the images and the general direction of the nanoindenter motion is known, Figures 3.52 and 3.53 can be used to determine the direction of motion of the dislocations, as well as their origins. Thus, in Figure 3.52, which corresponds to Figure 3.27, the slip plane of the dislocation does not appear to intersect any crystalline defects besides the dislocation itself and the particle's surface. This implies that the dislocation nucleated either homogeneously inside the crystal, or heterogeneously at the nanoparticle surface. Of these two possibilities, the nucleation of the dislocation at the surface is believed to be more probable because of the excess energy available there. In Figure 3.53, which corresponds to Figure 3.29, the slip planes of the dislocations intersect the surface, the dislocation and the twin. Twin defects in Ag have been known to emit dislocations readily under applied stress [107, 108], so it is possible that the dislocations both originated at the twin. Proposed mechanisms for this behavior are similar to the mechanism for the CHPE proposed by Li on the nucleation of dislocations from surface steps [109].

These results are also very significant to the nanocompression of nanopillars. The mechanism of deformation remains elusive in the study of nanocompression in nanostructured pillars because of the inability to resolve and study individual dislocations. Therefore, there has been an inability to determine the source of dislocations in these experiments, a flaw that has made theoretical modeling of the nanocompression experiments very difficult. The above discussion demonstrates that, at least in nanoparticles, dislocations can be generated from free surfaces and twins in the absence of Frank-Read sources.

Aberration-Corrected Phase Contrast Experiments

The aberration-corrected phase contrast experiments allow easier imaging of multiple lattice fringes and surface structure. As a result, the structure and behavior of dislocations caused by nanoindentation could be studied in greater detail.

In order to better understand the structure of the dislocations in Figures 3.36 and 3.39 the use of Fourier filtering is helpful. The Fourier filtered images of all three (111) planes shown in Figures 3.36 and 3.39 were created using the Gatan Digital Micrograph program (Figures 3.54 and 3.55). For example, if dislocation 1 in Figure 3.54 is examined in the Fourier filtered images 3.54B-3.54D; an interesting observation can be made. Despite the differing directions of the lattice fringes, both Figures 3.54C and 3.55D show terminating lattice planes in the same location. In each case the terminating fringes are associated with dislocation 1. However, the lattice fringes in figure 3.54B do not show any deformation in the vicinity of dislocation one. This implies that the Burgers vector is parallel to that (200) lattice plane.

This triple Fourier filtering technique makes the dislocation’s origin easy to determine, because edge dislocations are expected to move in the direction of the Burgers vector. In the case of dislocation 1 in figures 3.54A-D, it is readily apparent that the dislocation originated at the interface between the probe and the particle because this interface is intersected by the (200) lattice plane that the dislocation’s Burgers vector is on.

The same procedure can be done for dislocations 2 and 3 in Figures 3.54 and 3.55. For dislocation 2, the terminating lattice planes appear in Figures 3.54C and 3.54D, but not in Figure 3.54B. This indicates that the Burgers vector of dislocation 2 is also on the (111) planes shown in figure 3.54B. The direction of the Burgers vector indicates that this dislocation also originated at the interface between the sample and the probe. If dislocation 3 in Figures 3.55A-D is examined, a similar conclusion can be reached. Terminating lattice fringes associated with dislocation 3 are seen in Figures 3.55C-D, but not in Figure 3.55B. This shows that the Burgers vector is parallel to the fringes in Figure 3.35B. By tracing the lattice fringe in Figure 3.55B that intersects the terminating lattice fringes in Figures 3.55C and 3.55D, it can be concluded that the dislocations originated at the interface between the probe and the sample.

In section 3.2.1 it was stated that the pristine particle did not show any dislocation defects (Figure 3.56A). In order to support this assertion, Fourier filtering imaging corresponding to the pristine particle was done. Figures 3.56B-D confirms the lack of dislocations. Overall, the lattice fringes in Figures 3.56B-D have very good registry in the area where the particles do not overlap. There are however a few cases where one image shows an apparent dislocation, but the same dislocation is not seen in any of the other images. Because three sets of fringes were examined, any deformation should be seen in at least 2 of the sets of fringes. This suggests that the terminating fringe is not caused by a dislocation. For instance, increases in particle thickness can cause phase advancement of the exit waveform, which can lead to inversion of light and dark fringes. Because the terminating fringes in Figure 3.56 occur exclusively in regions were the two particles overlap, this is quite likely.

Fourier filtering was also used to analyze the nanoparticle after nanoindentation, which is shown in Figure 3.57. The lack of dislocations helps to confirm the theory that dislocations are ejected from nanoparticles spontaneously. In general, the results of the aberration-corrected phase contrast experiments are clear. Pristine nanoparticles do not contain dislocations, but dislocation nucleation can occur by an applied strain. These dislocations tend to nucleate at the interface between the indenter and the nanoparticle. When the applied strain is removed, the dislocations become unstable and are ejected from the nanoparticle.

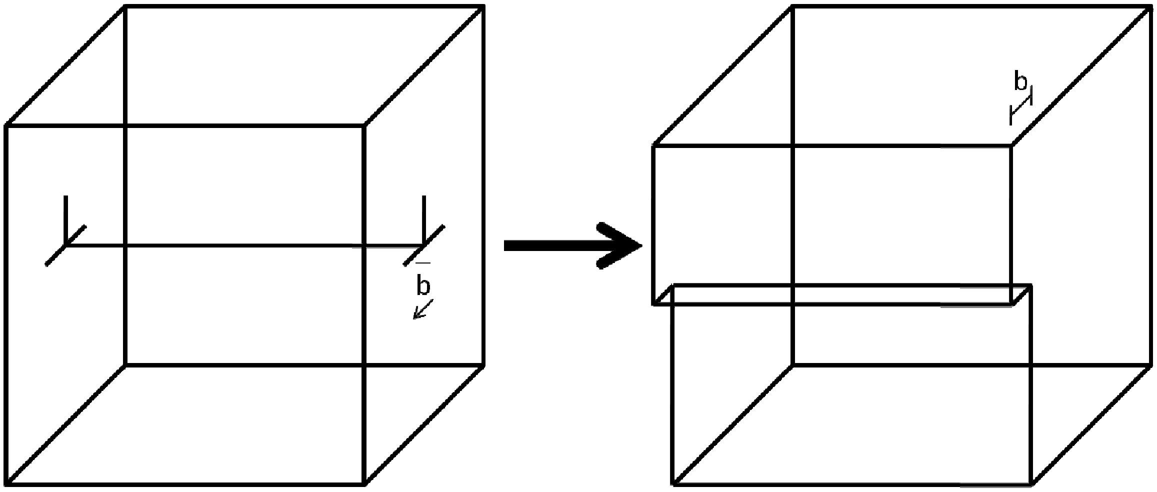

Figure 3.1: A schematic diagram of the ejection of an edge dislocation at an atomically smooth free surface. The dislocation leaves a surface step with a width equal to the Burgers vector.

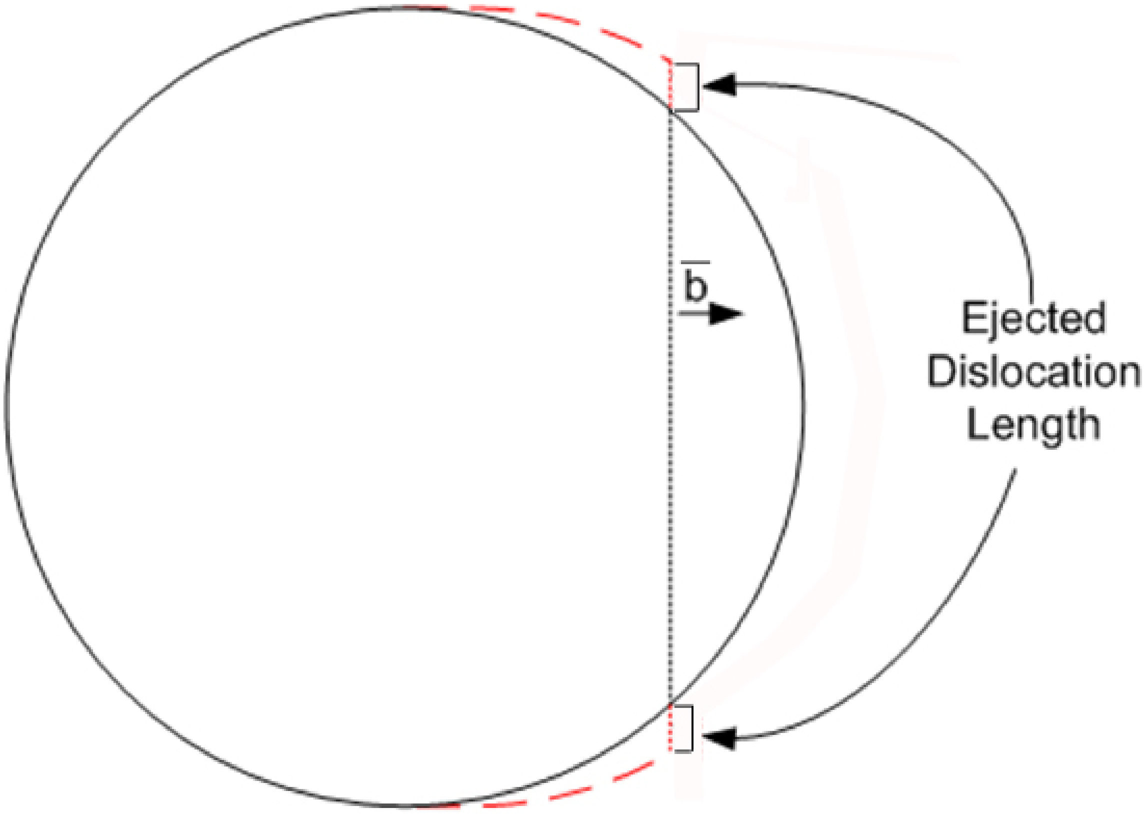

Figure 3.2: A schematic diagram of a dislocation's line length changing as it glides across a nanoparticle. As segments of the dislocation leave the crystal, the energy of the dislocation is reduced.

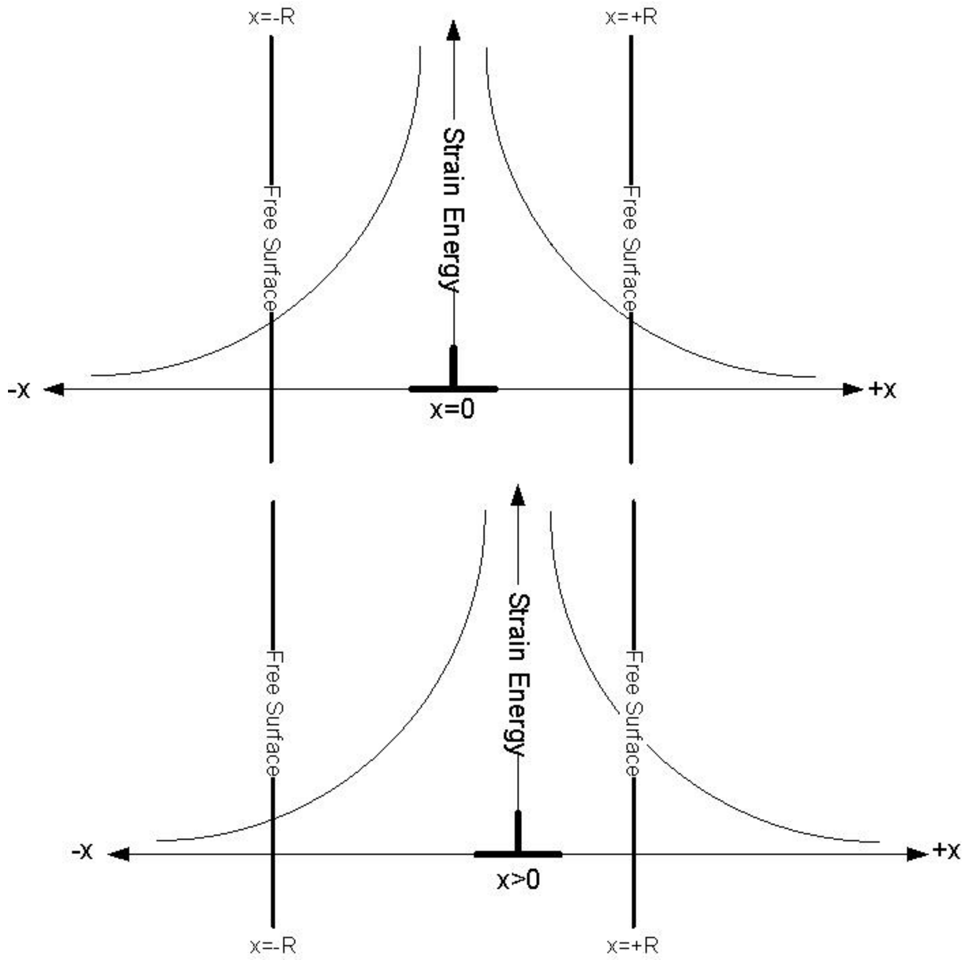

Figure 3.3: A schematic diagram showing how a dislocation can lower its strain energy by moving towards a free surface. As the dislocation approaches the grain boundary going from x=0 to x>0, its total strain energy is reduced because highly strained crystal near the dislocation is being replaced by low strain crystal farther away from the dislocation.

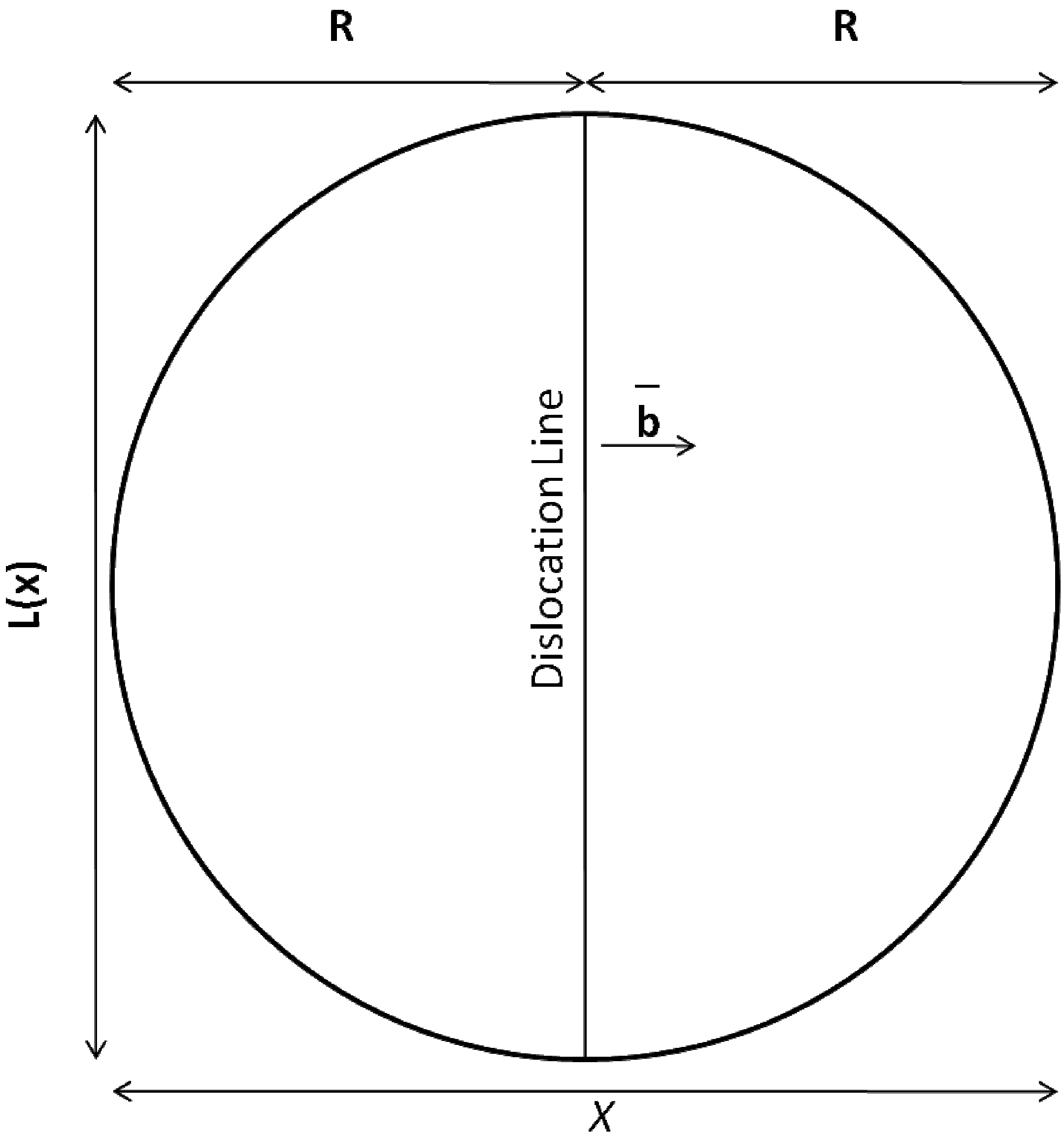

Figure 3.4: Schematic of a nanoparticle with a dislocation bisecting its cross-section. R is the nanoparticle's radius, and b is the Burgers vector. The direction x is defined in the direction of the Burgers vector.

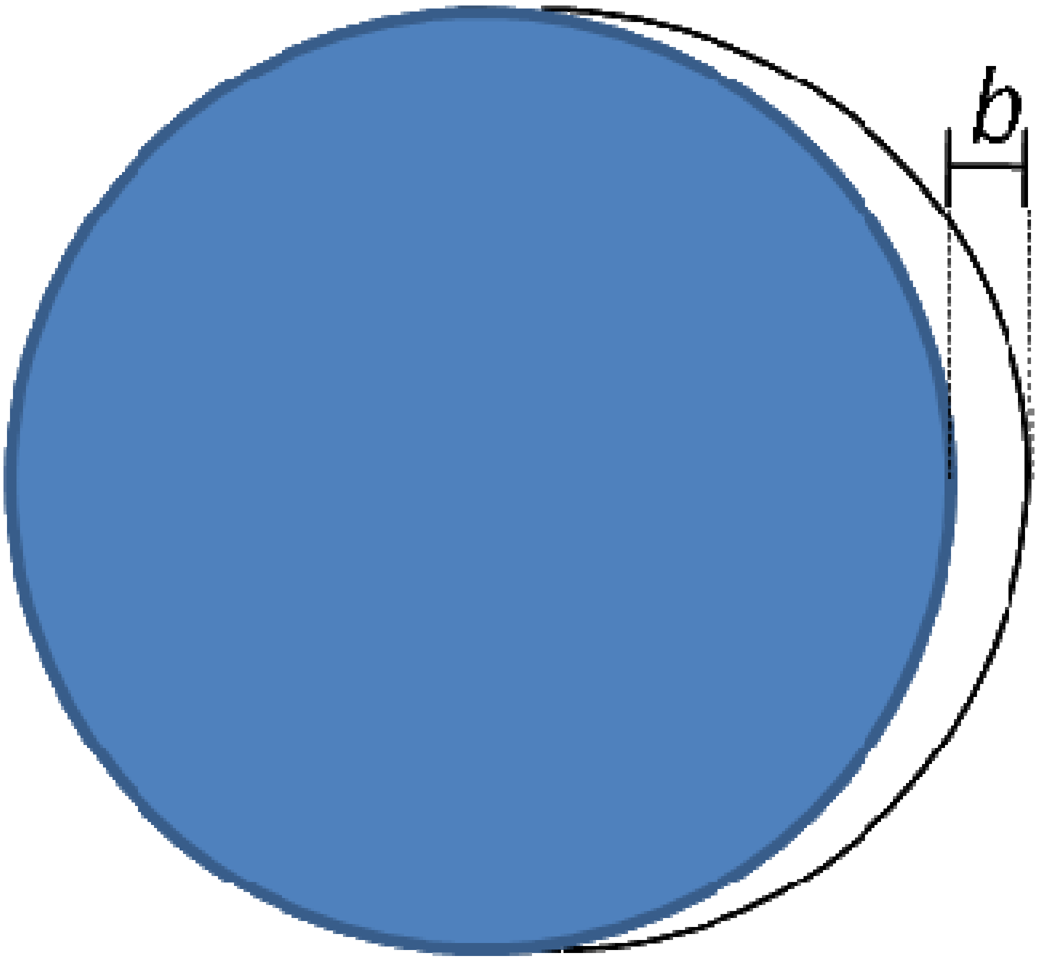

Figure 3.5: A schematic diagram of the surface step for a nanoparticle that just ejected an edge dislocation. The shaded area is the nanoparticle and the white area is the surface step. The surface step has the same profile as the non-deformed particle.

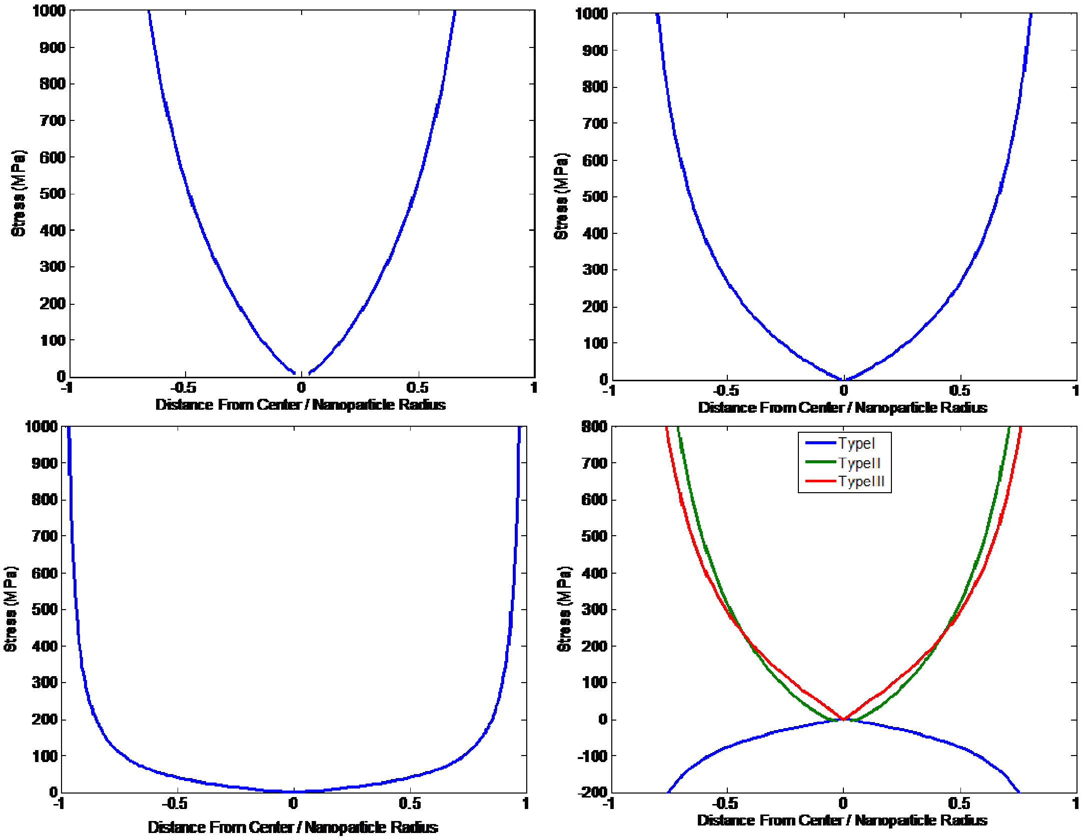

Figure 3.6: Spontaneous stress vs. distance of a dislocation from the nanoparticle center for several spherical Ag nanoparticles with diameters of 20, 50 and 500nm. The center of the nanoparticle is x=0. The horizontal line represents the yield stress of Ag. When the spontaneous stress is greater than the yield stress, we expect the dislocation to be spontaneously ejected from the nanoparticle. The last figure shows the values for Type I, II and III stresses in a 20nm nanoparticle. Type II and III stress are approximately the same, in this case.

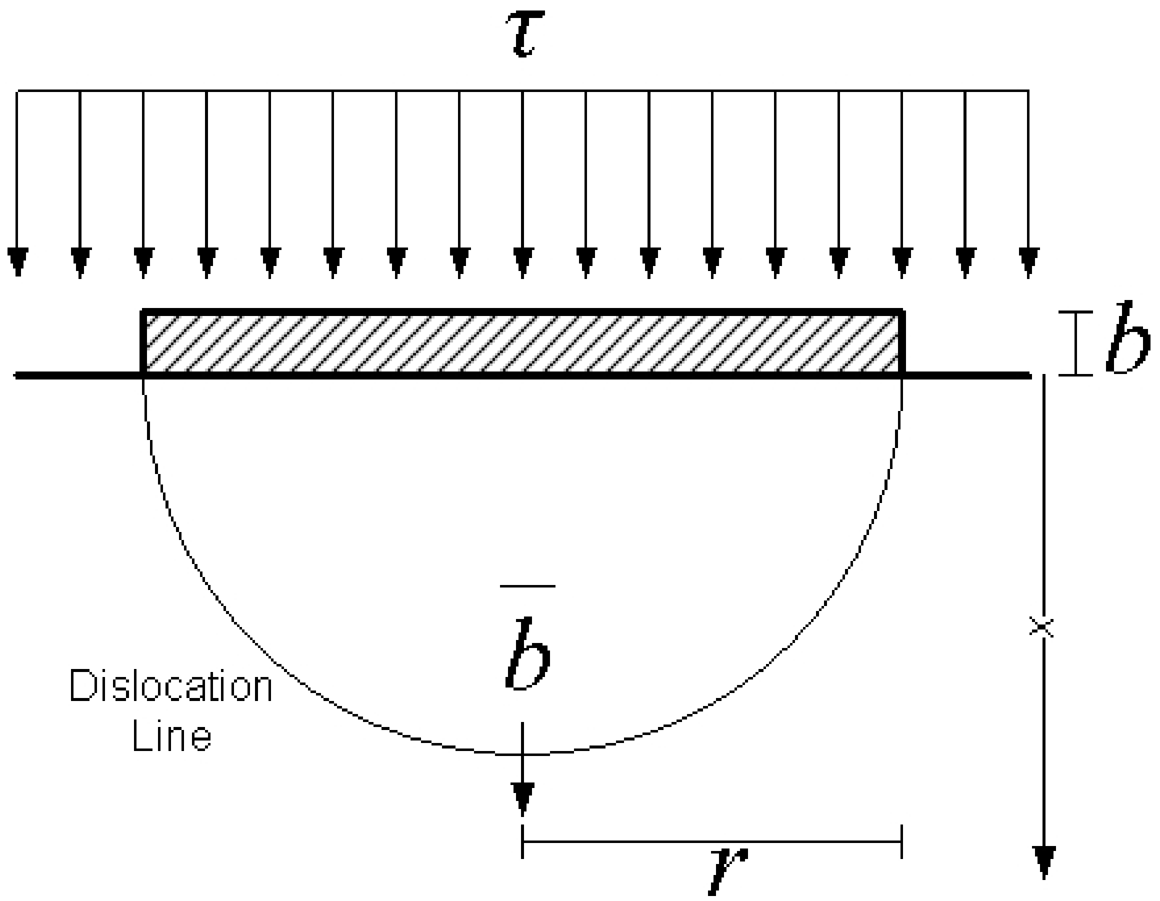

Figure 3.7: A schematic diagram of a dislocation in a semi-infinite foil. The variable τ is the applied stress, and r is the radius of the dislocation loop, b is the Burgers vector. The direction x is parallel to the Burgers vector. The cross-hatched area is the surface step created by the dislocation.

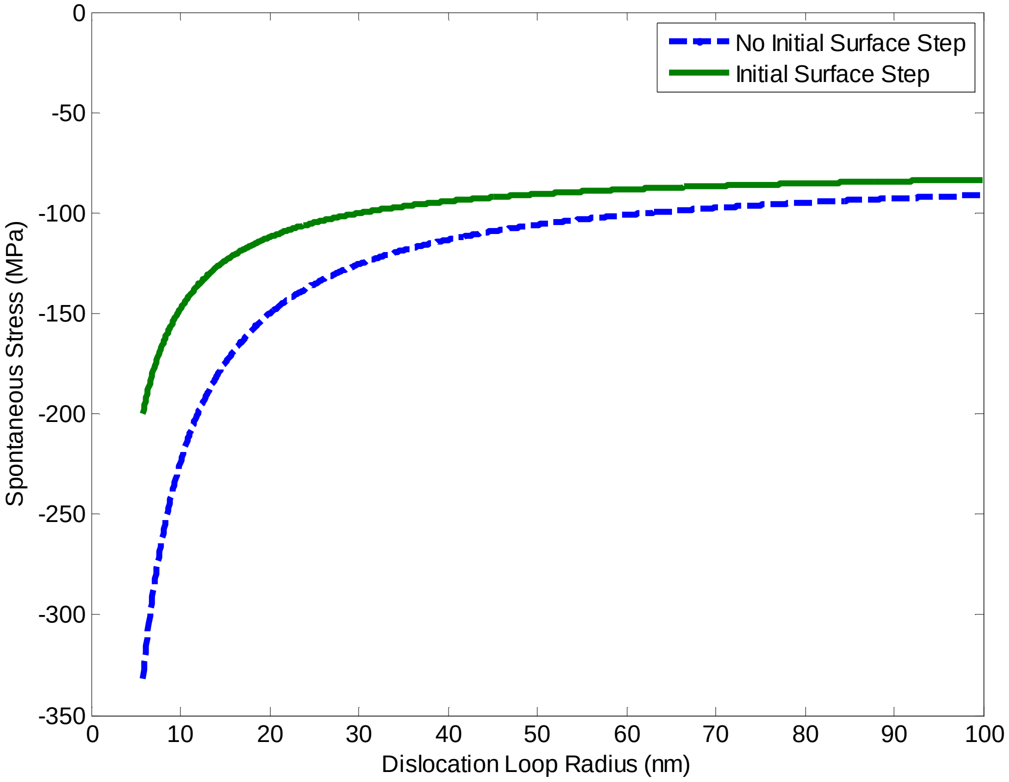

Figure 3.8: Spontaneous stress on a dislocation half loop in a semi-infinite silver foil for the cases were the dislocation nucleates in the absence or presence of a surface step. The negative sign indicates a stress pulling the dislocation towards the free surface.

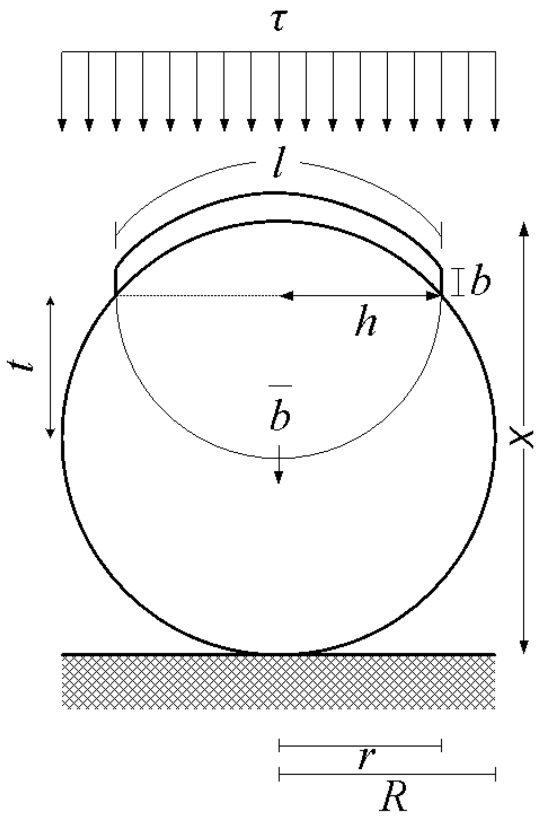

Figure 3.9: A schematic diagram of a dislocation half loop in a spherical nanoparticle. R is the nanoparticle radius, b is the Burgers vector, τ is applied stress, x is the slip direction of the dislocation, r is the radius of the dislocation, l is the length of the surface step, and t is the distance between the nucleation site and the base of the semicircle formed by the dislocation. The variable *h* is radius of the dislocation half-loop and *t* is distance from the center of the nanoparticle line defined by h.

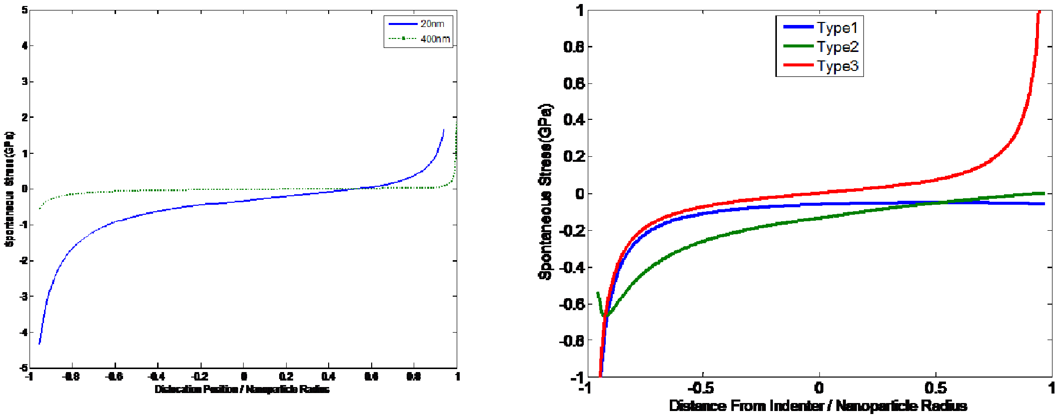

Figure 3.10: Spontaneous stress vs. position for two nanoparticles, one with a 20nm and a 400nm diameter nanoparticle. The position is normalized by dividing by the nanoparticle's radius. The second plot shows the type I, II and III stresses. The type III stress is clearly dominant for most of the deformation process.

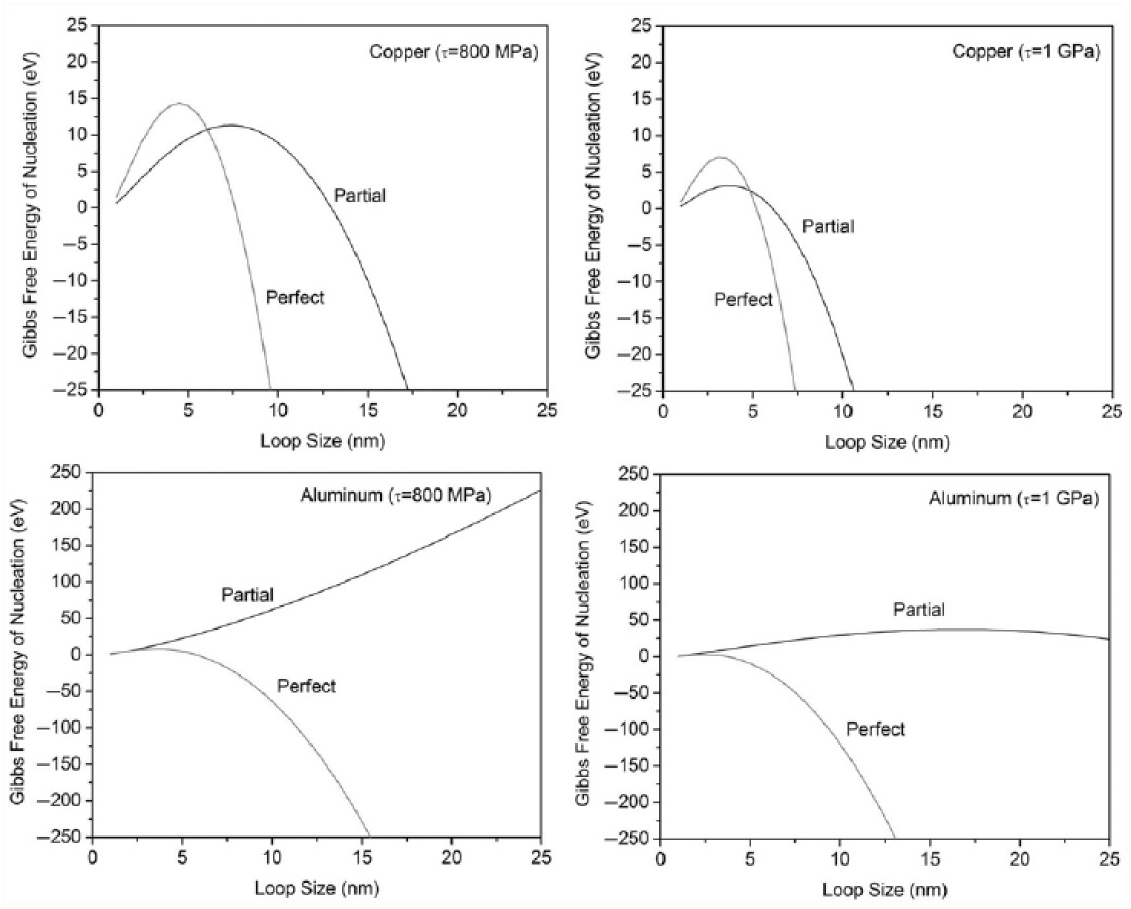

Figure 3.11: Gibbs free energy of nucleation for perfect and partial dislocation loops in infinite size particles of Cu and Al when subject to applied stresses of 800MPa and 1 GPa.

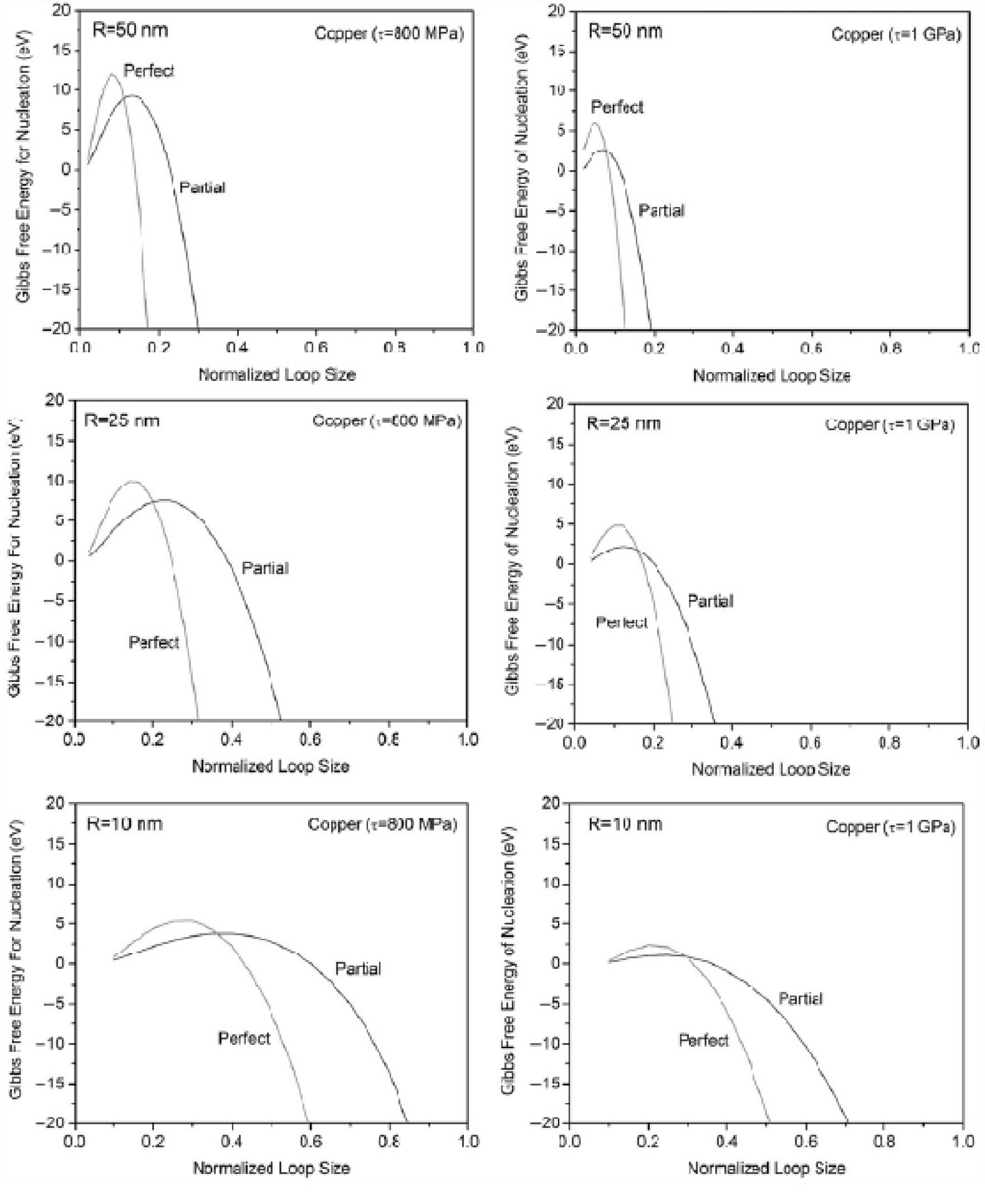

Figure 3.12: Gibbs free energy of nucleation for perfect and partial dislocation loops in nanoparticles of Cu ranging from 50 (a, b), 25 (c, d) to 10nm (e, f), when subject to an applied stresses of 800MPa and 1 GPa.

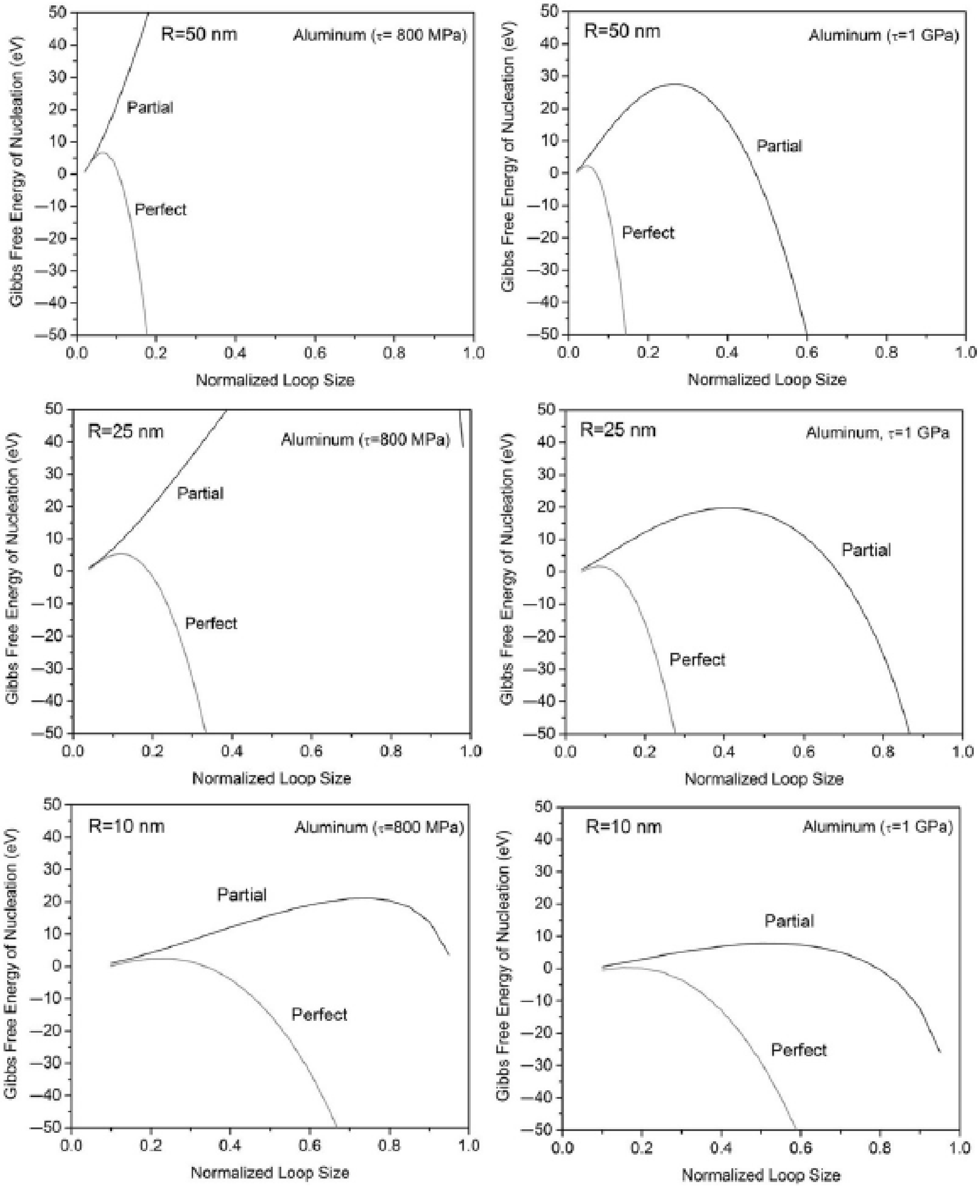

Figure 3.13: Gibbs free energy of nucleation for perfect and partial dislocation loops in nanoparticles of Al ranging from 50 (a, b), 25 (c, d) to 10nm (e, f), when subject to an applied stresses of 800MPa and 1 GPa.

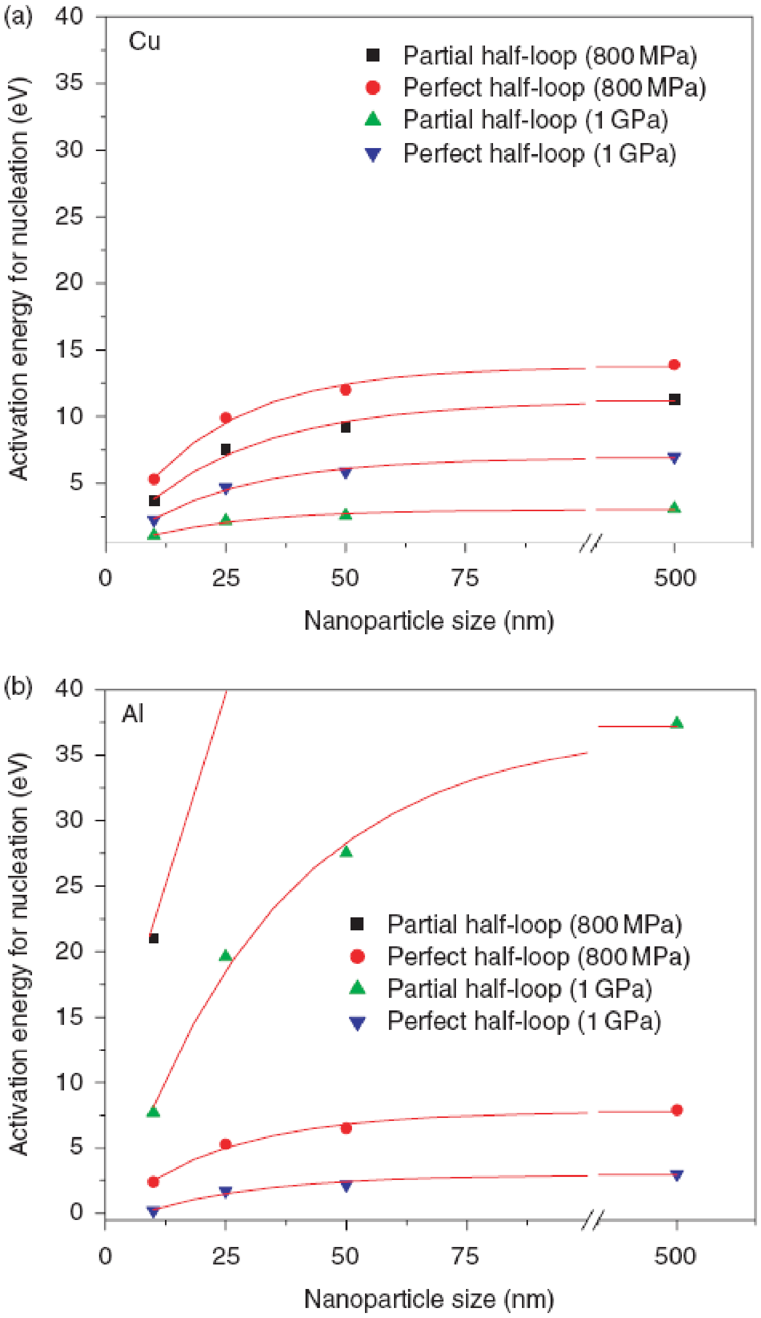

Figure 3.14: Activation energy for nucleation of critical size dislocation loops in Cu and Al for applied stresses of 800MPa and 1 GPa.

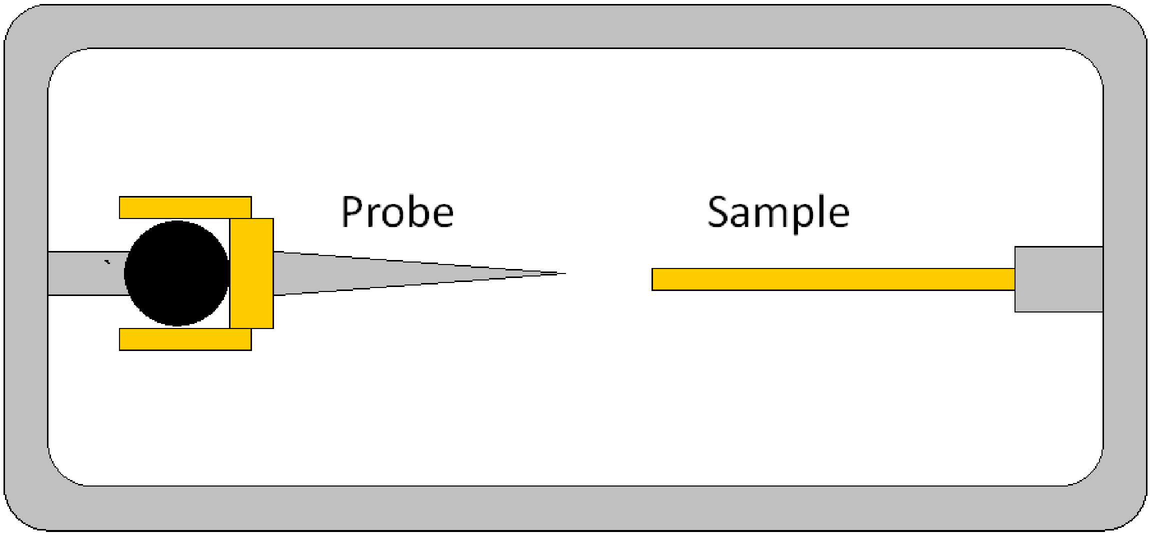

Figure 3.15: A schematic diagram of the Nanofactory instruments type stage used for phase contrast nanoindentation experiments. The stage consists of an electropolished W probe (left) and a C wire (right) that was dry dipped in Ag nanoparticles. The Nanofactory instruments holder can be supplied with a diamond tip (Nanoindentation holder) or a W tip (STM holder).

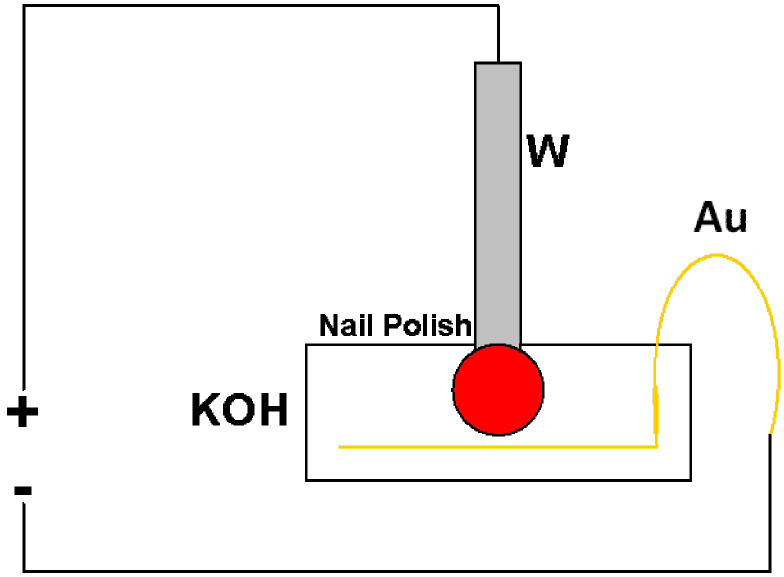

Figure 3.16: Setup used for electropolishing the W probe. First, the W wire is suspended vertically in a bath of KOH. Subsequently, a current is passed through the W to a loop of gold wire at the bottom of the bath. As the wire is electropolished, the area that is directly above the nail polish but still in the bath is thinned. Eventually, the W in the KOH not covered by nail polish is electropolished, and the ball of nail polish falls off. At this point the current is stopped and the wire is removed.

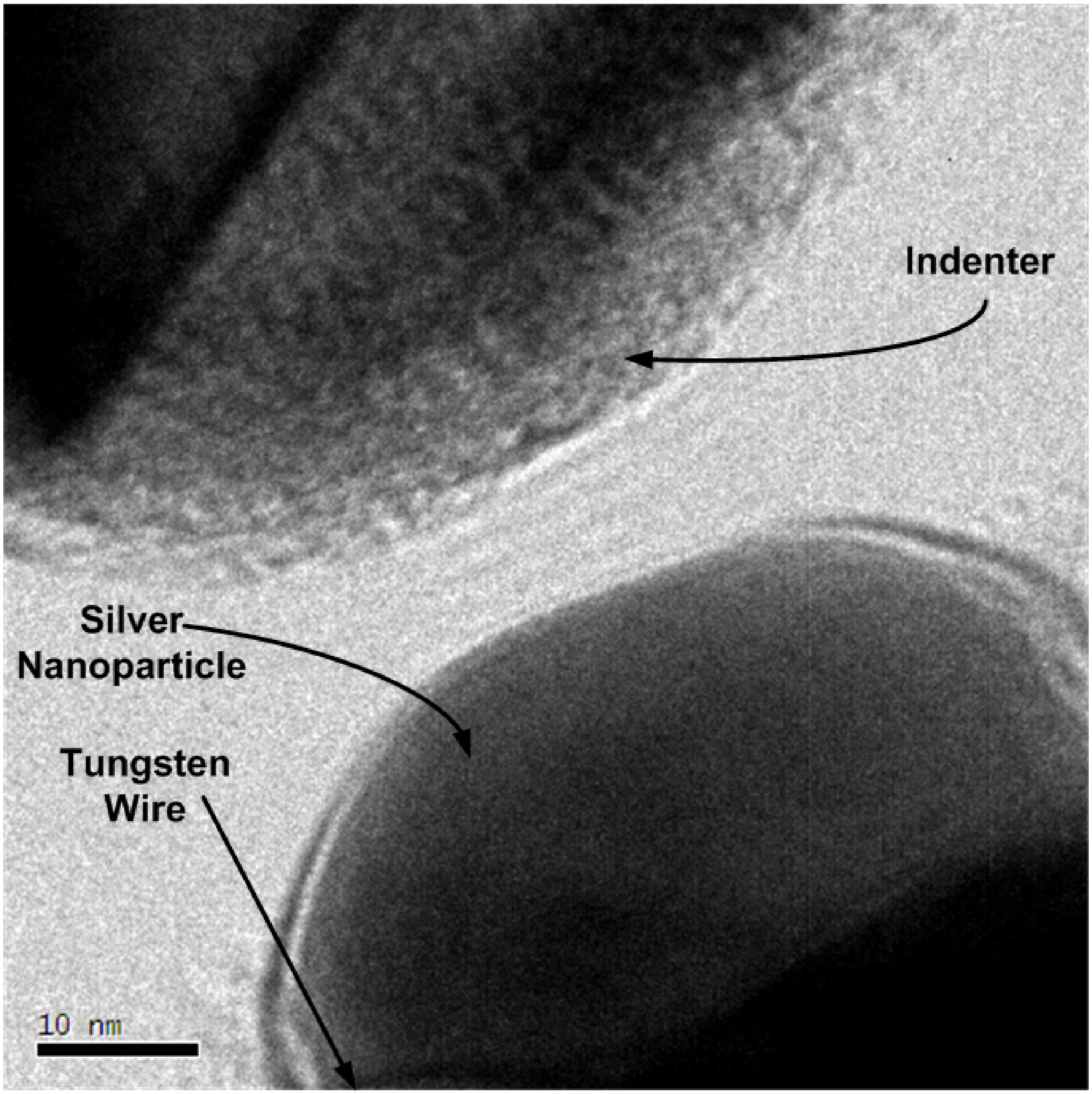

Figure 3.17: Diffraction contrast TEM image of the, W support and the Ag particle before indentation.

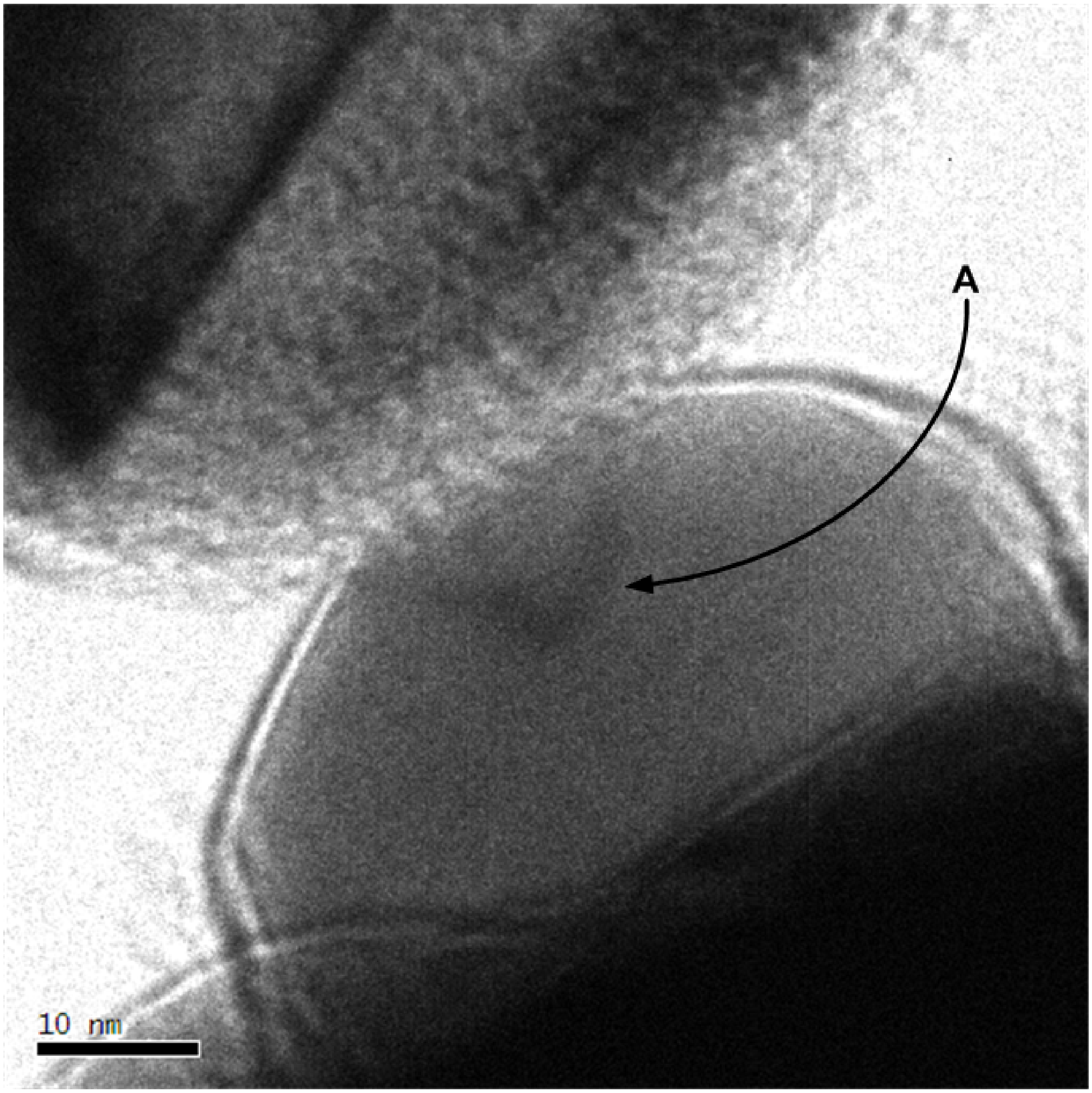

Figure 3.18: TEM image during initial contact with the particle. Note the contrast band (labeled A) that appears in the particle.

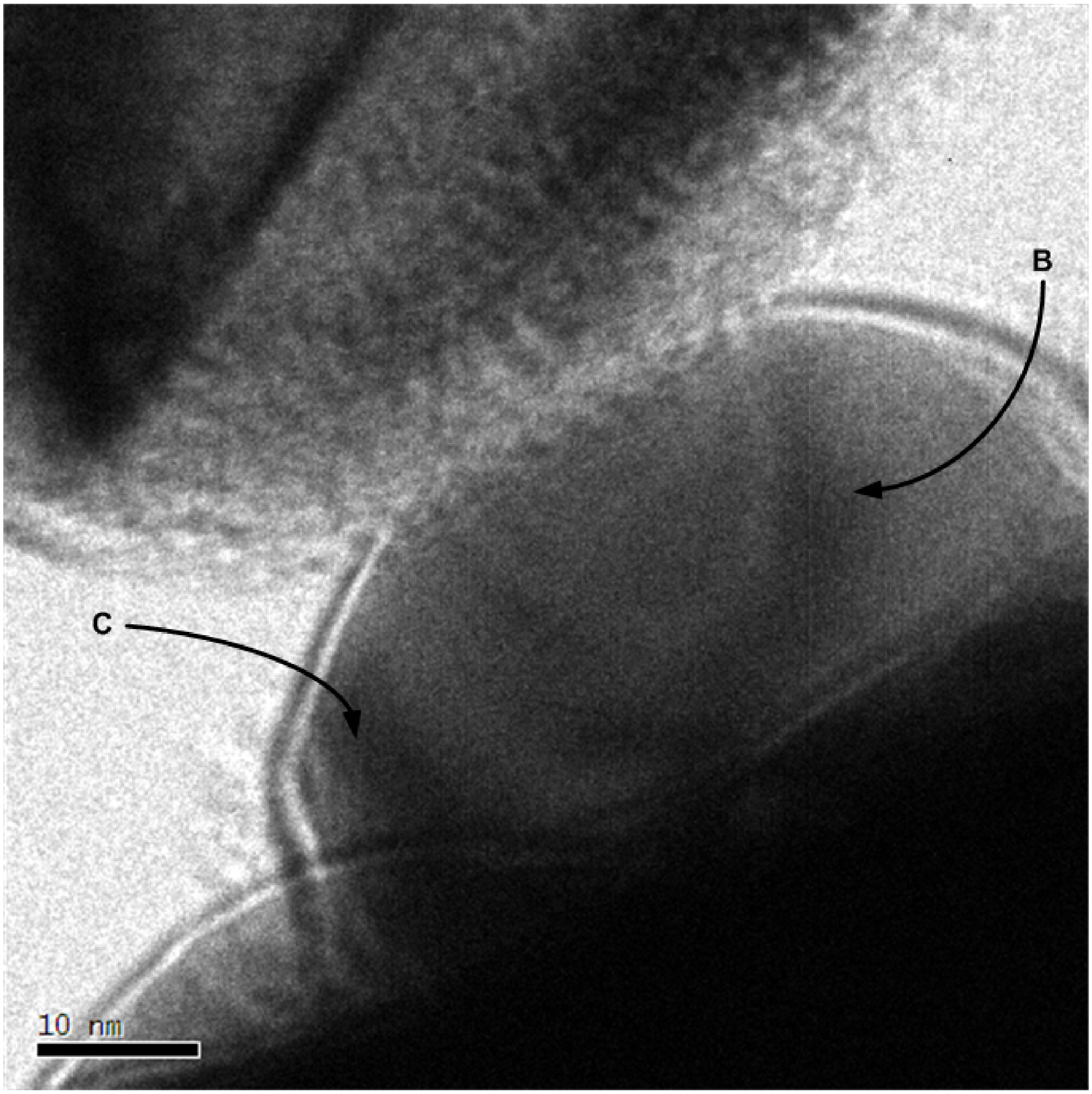

Figure 3.19: TEM image captured after the probe was translated further toward the particle. Two contrast bands (labeled B and C) are now seen.

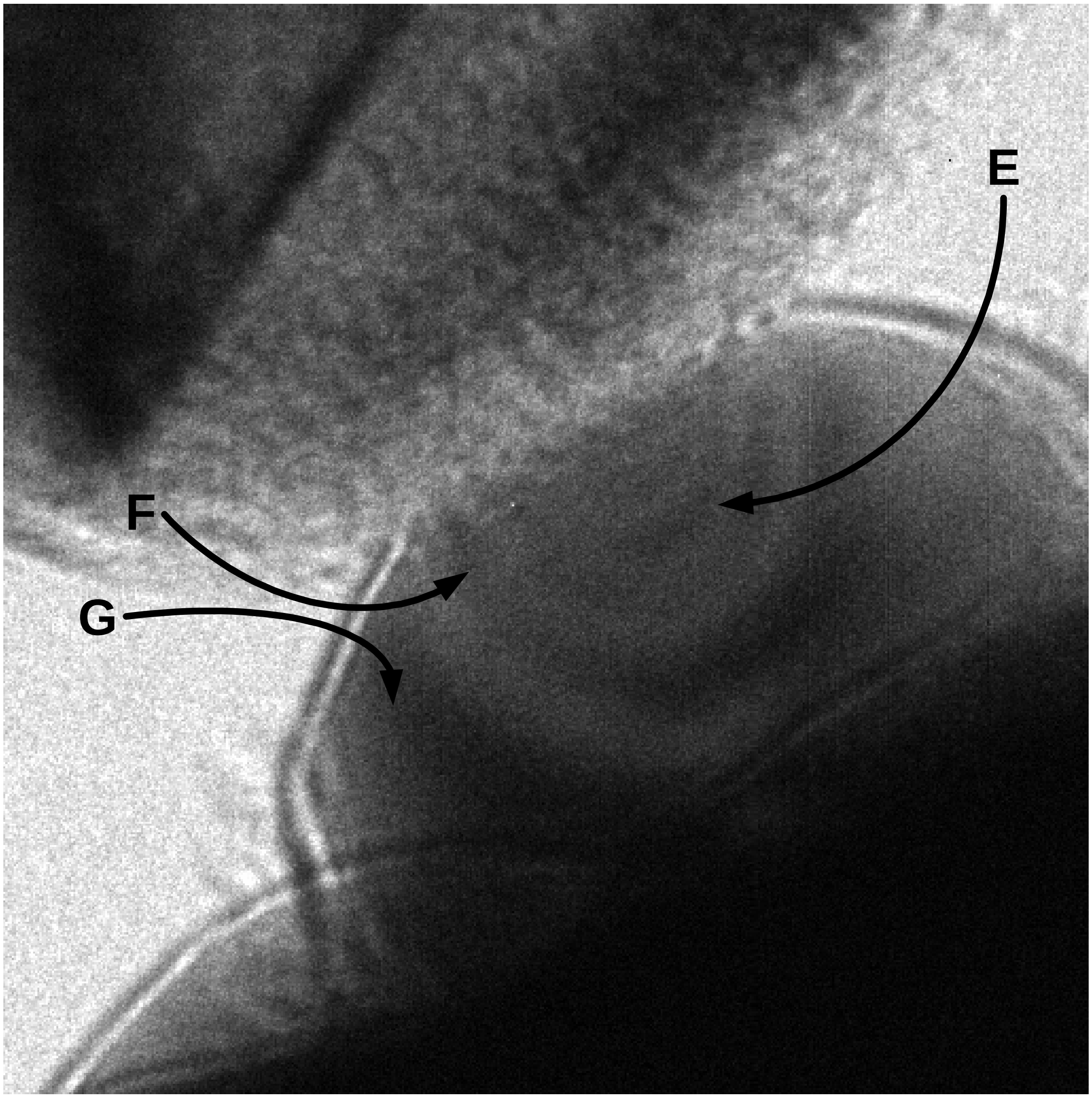

Figure 3.20: TEM image captured after the probe was translated further towards the particle further. Three contrast bands (labeled by E, F and G) are shown in this image.

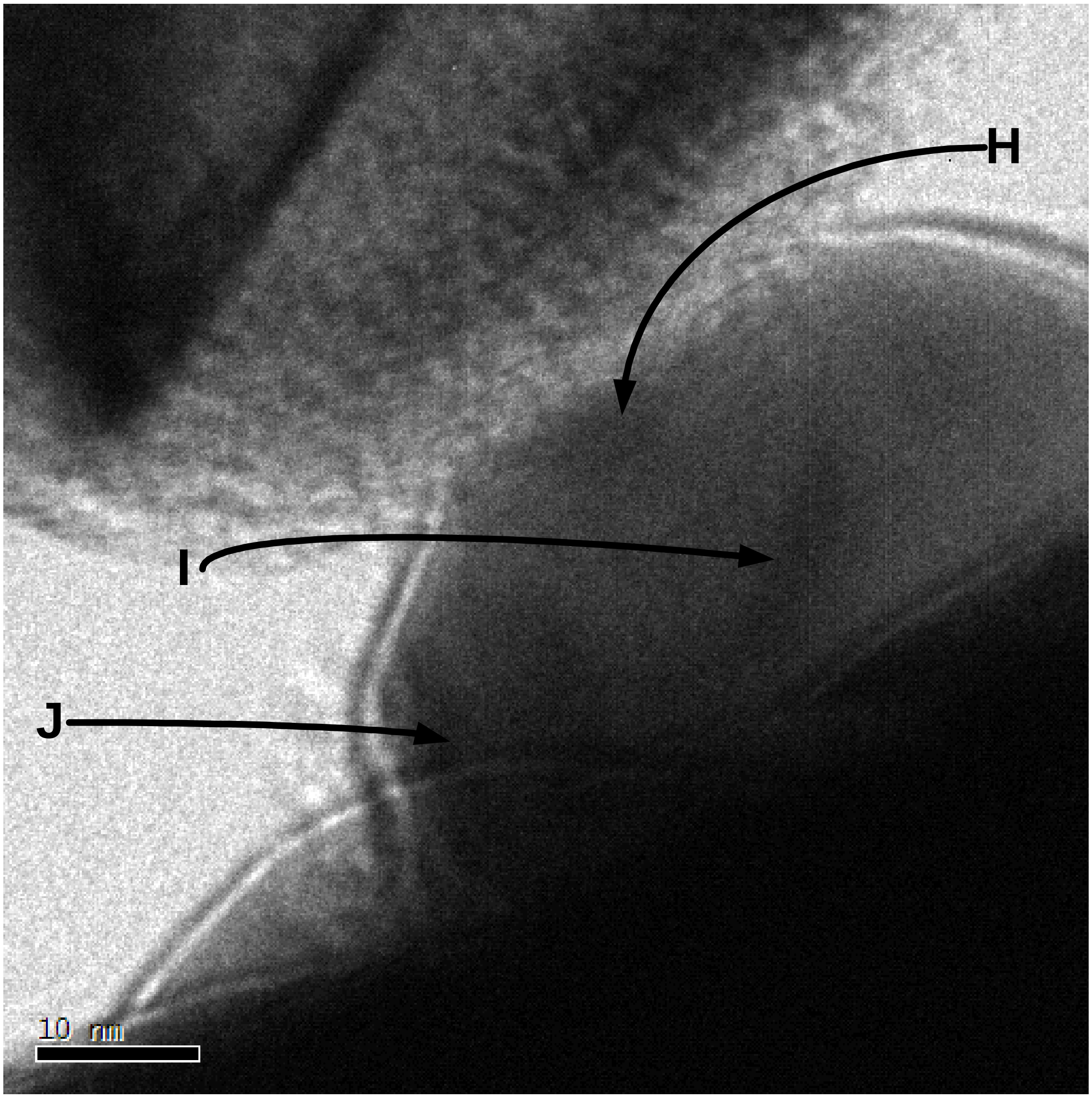

Figure 3.21: TEM image taken after the strain was further increased. Three contrast bands (labeled H, I, J) are shown.

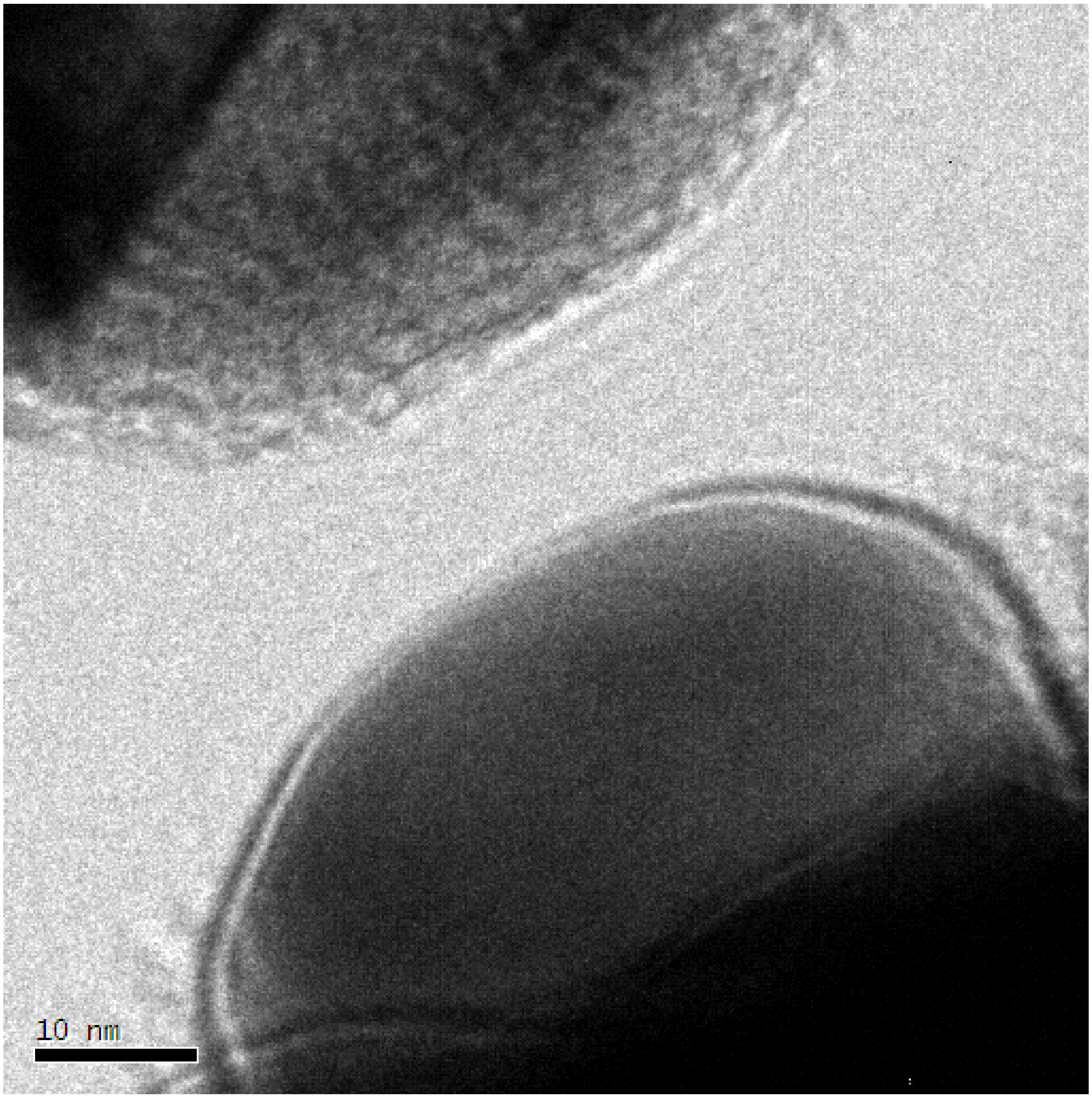

Figure 3.22: TEM image captured after the indenter was translated away from the nanoparticle until they were no longer in contact. Note the absence of contrast bands inside the particle.

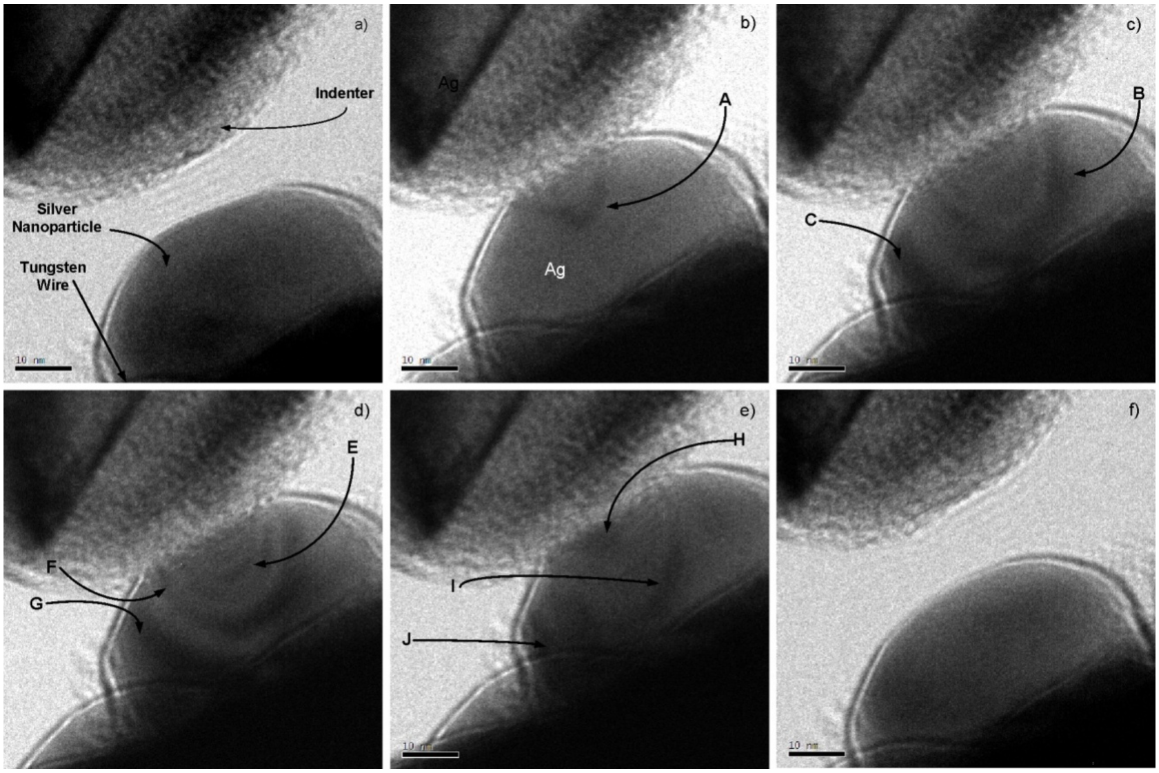

Figure 3.23: Sequence of images showing the development of contrast bands during the nanoindentation experiment.

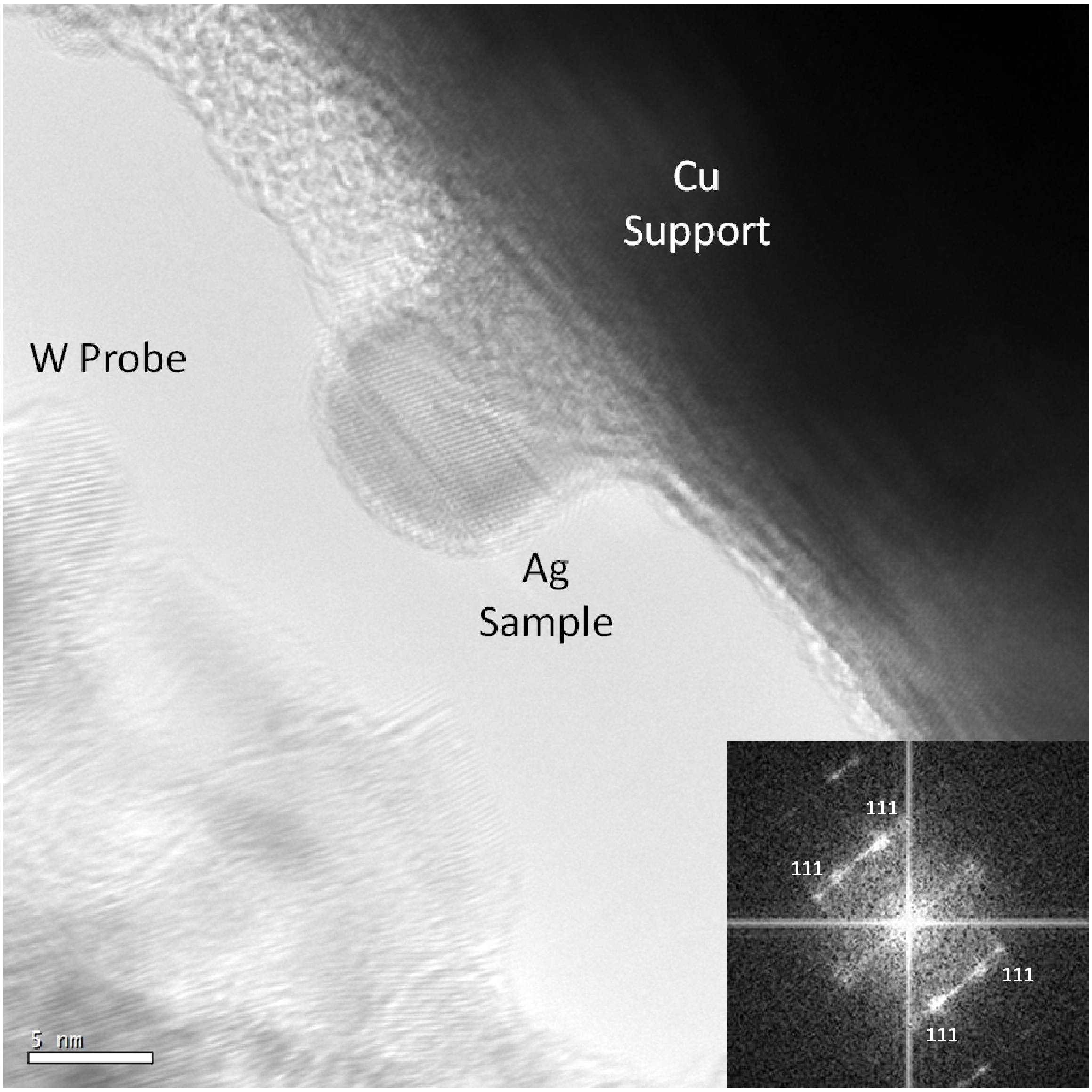

Figure 3.24: High resolution image captured before the start of the phase contrast nanoindentation experiment. An indexed FFT of the nanoparticle is shown in the lower right.

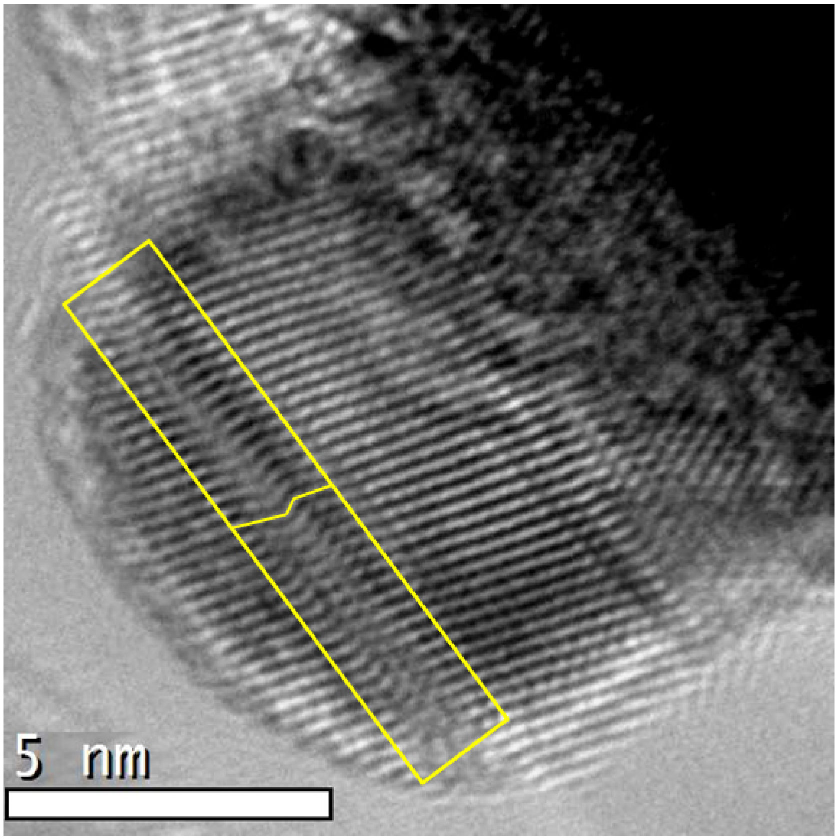

Figure 3.25: High-resolution TEM image of the Ag nanoparticle shown in Figure 3.24. Notice the twin inside the rectangle. Twin boundaries are two dimensional defects between two regions of crystal that have rotated such that they have reflection symmetry about the twin plane. This can be seen from the distortion in the lattice planes that are highlighted. Also, notice that, aside from this defect the planes have very good registry, which is an indication of a lack of dislocations.

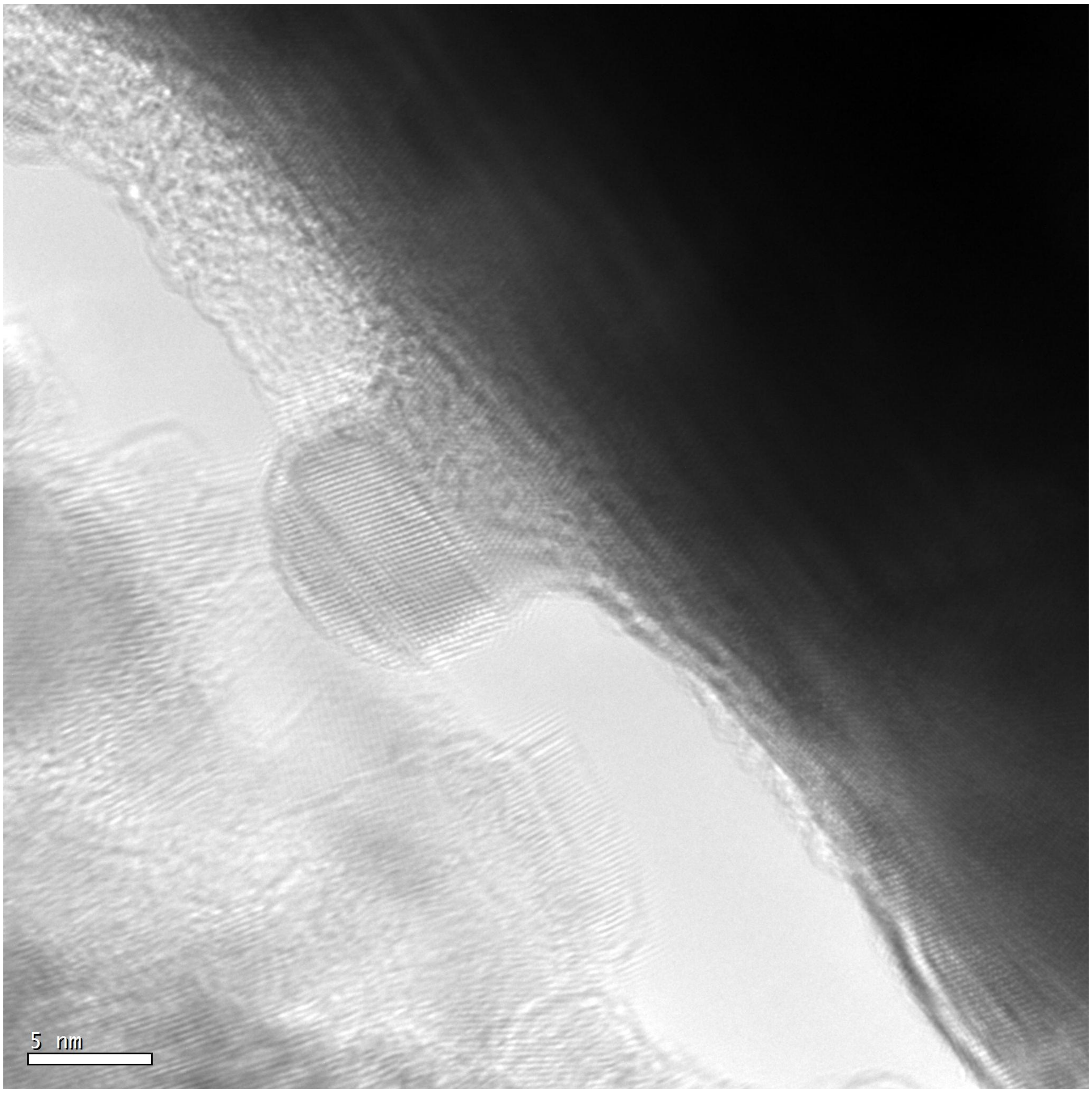

Figure 3.26: High-resolution TEM image taken just after the probe was brought into contact with the nanoparticle.

`

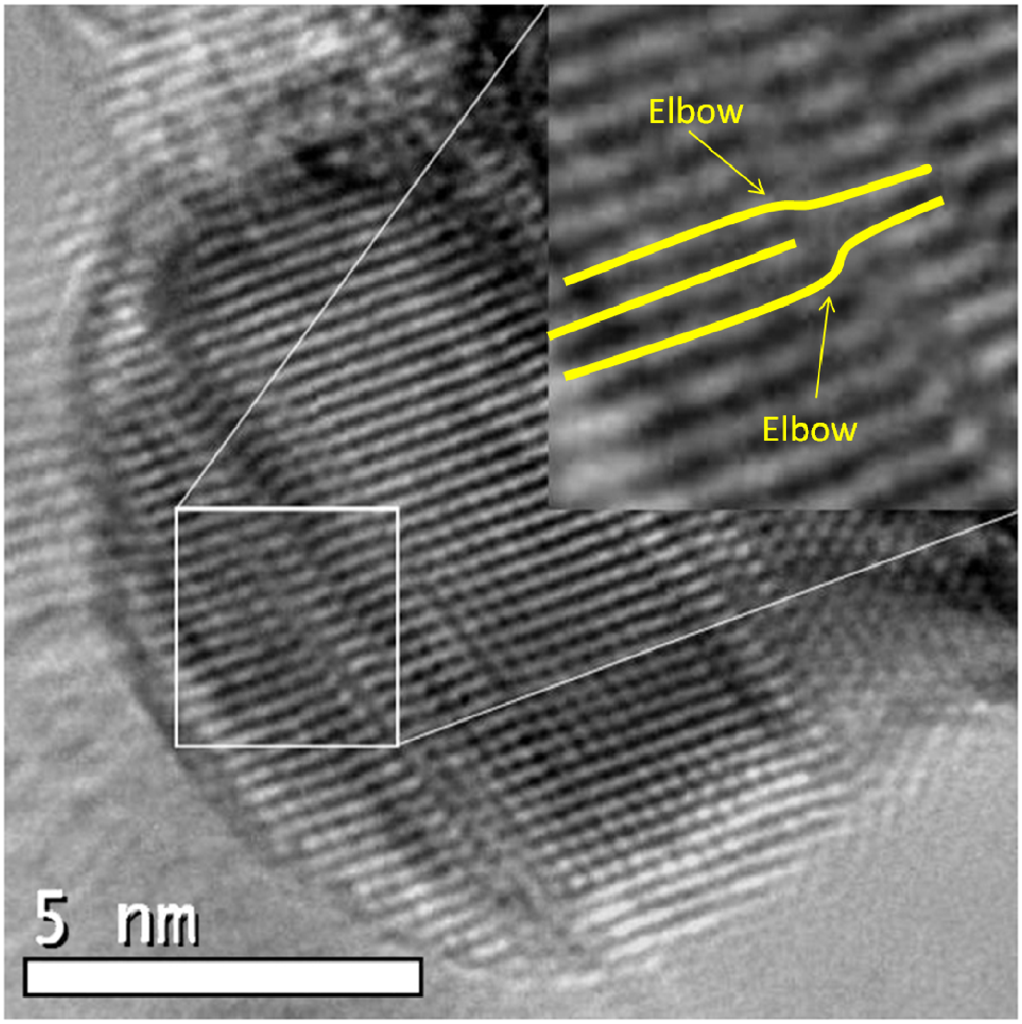

Figure 3.27: High resolution image of the Ag nanoparticle shown in figure 3.26. The inset image shows the presence of a lattice fringe that terminates inside the crystal, which indicates the presence of a dislocation. The points were the lattices fringes adjacent to the dislocation begin to deform appreciably are indicated as "elbows" and are important to the analysis of the dislocations Burgers vector.

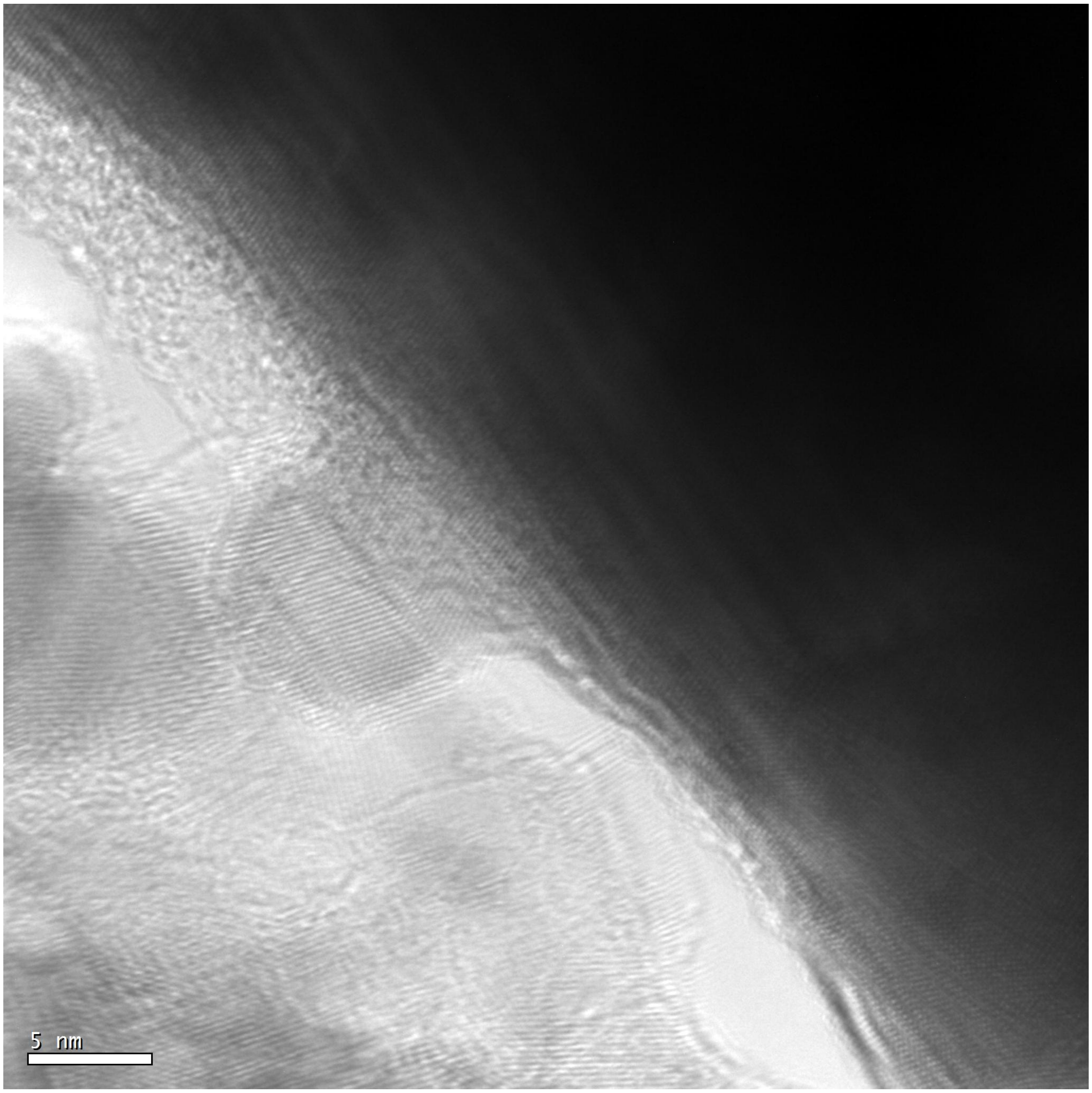

Figure 3.28: High resolution TEM image captured after the probe was translated further towards the sample.

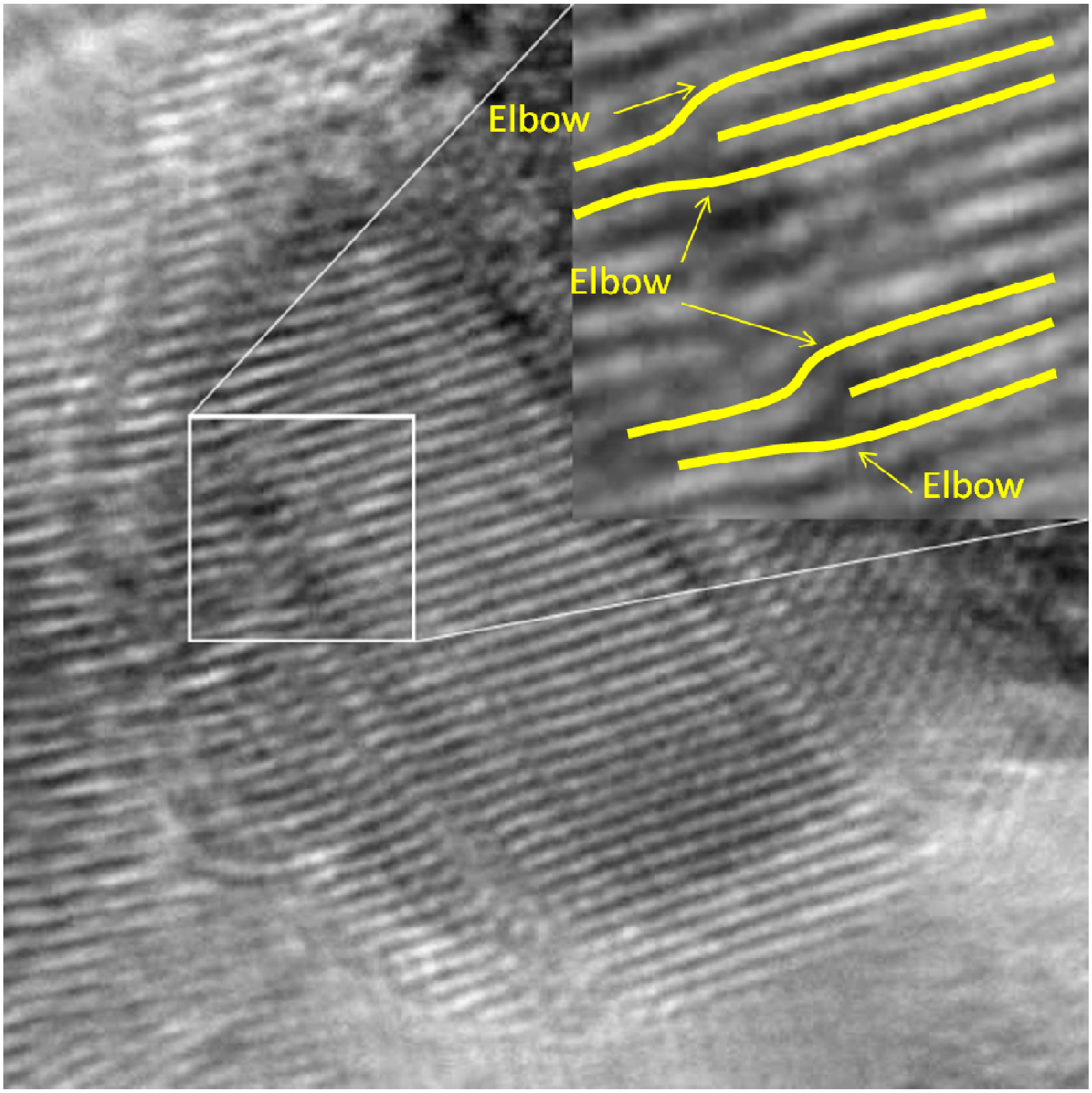

Figure 3.29: High-resolution image of Figure 3.28 that was digitally magnified. The inset shows a pair of terminating lattice planes indicating the presence of two dislocations.

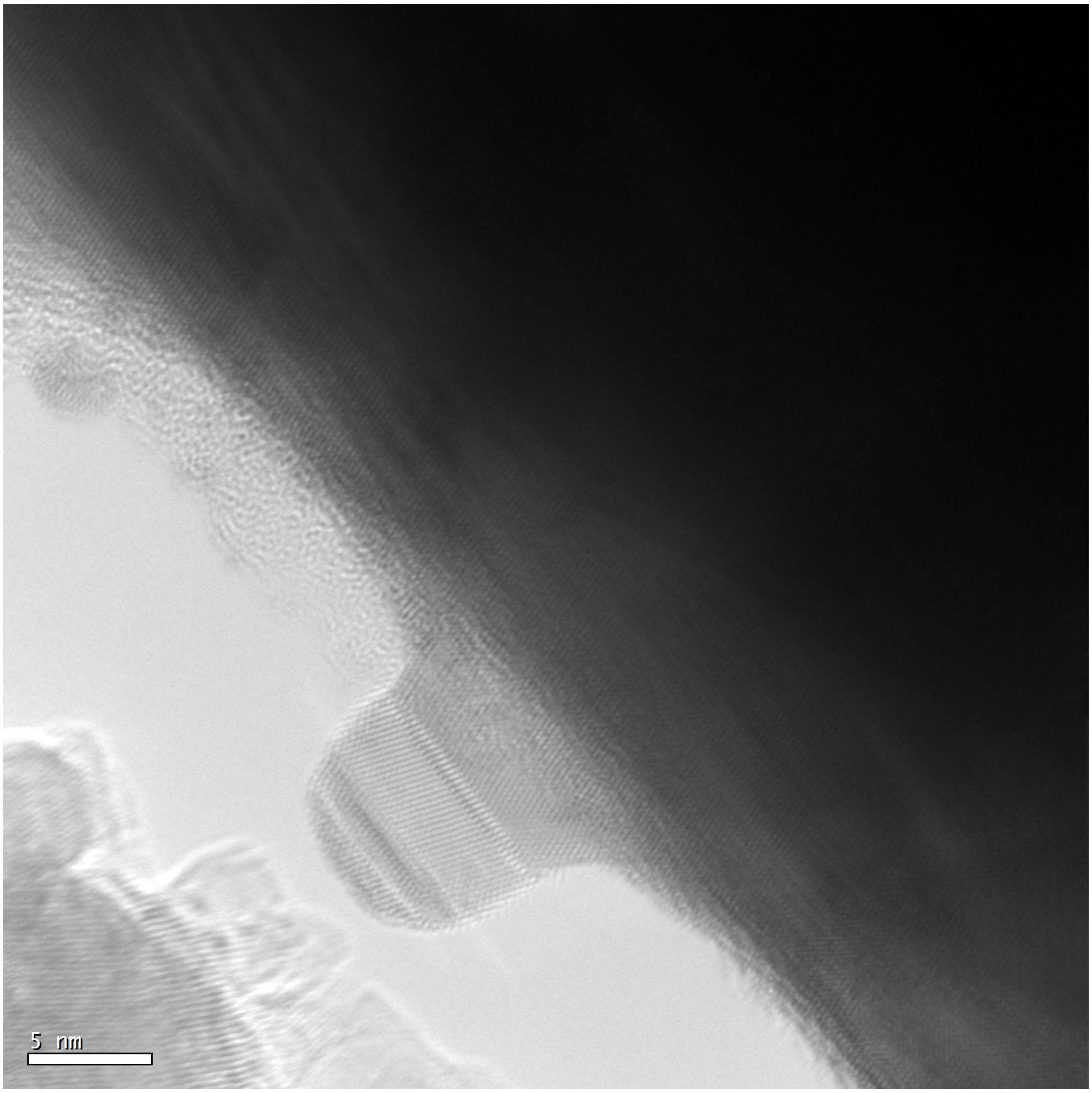

Figure 3.30: High –resolution TEM image captured after the probe was translated away from the nanoparticle until they were no longer in contact.

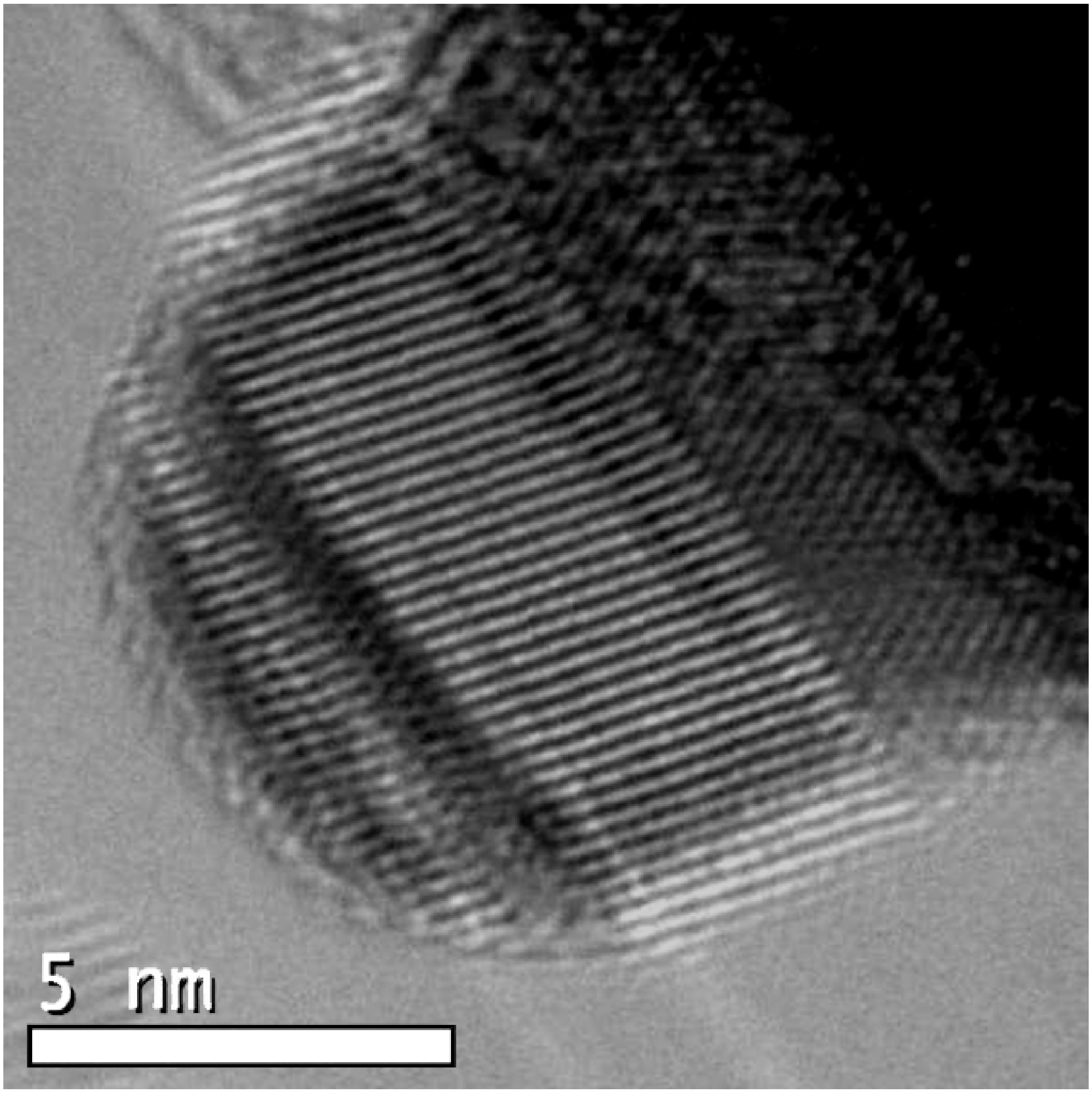

Figure 3.31: High resolution image of figure 3.30 that was digitally magnified. No terminating lattice planes are readily apparent, indicating an absence of dislocations.

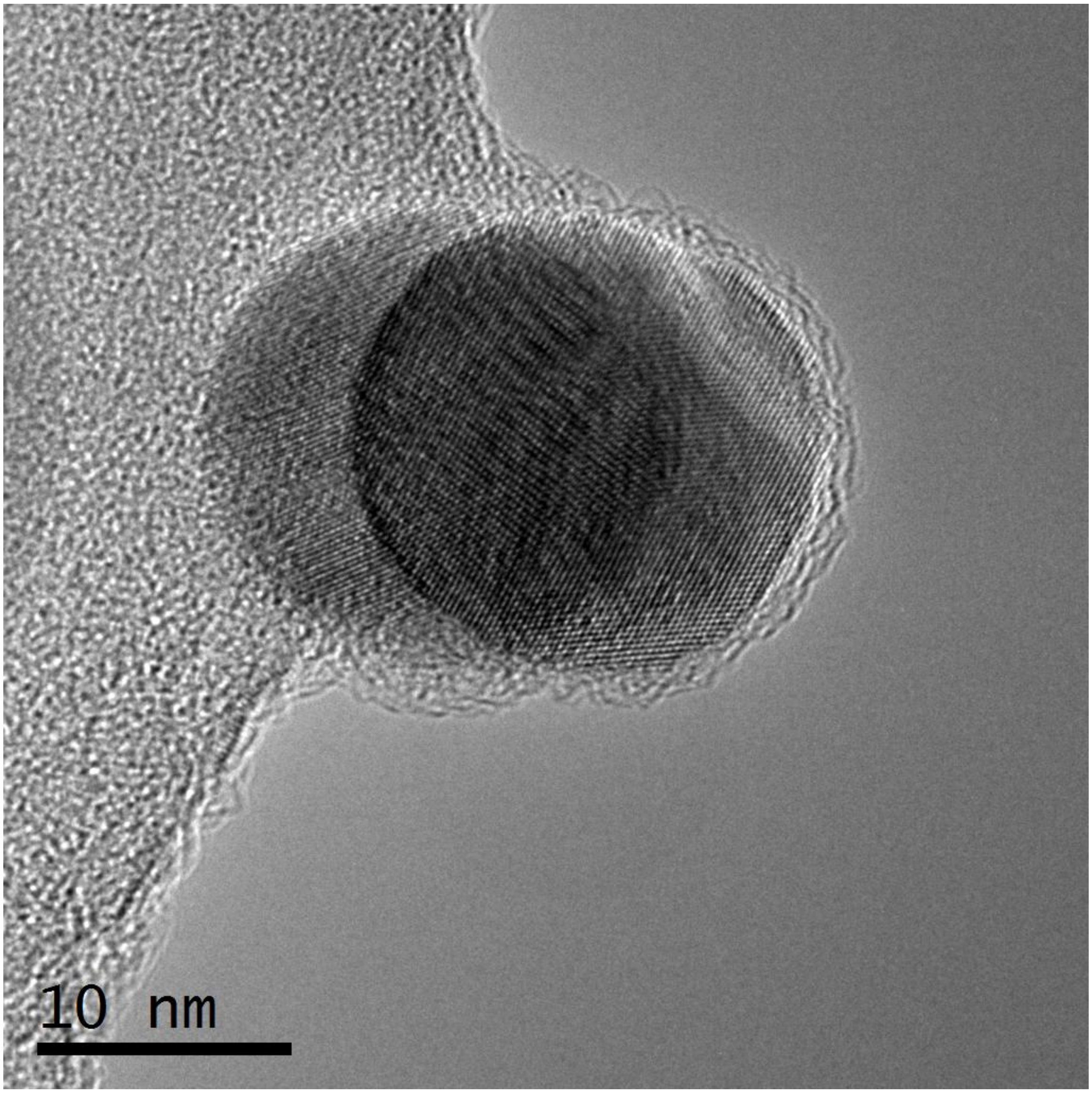

Figure 3.32: Aberration corrected high-resolution TEM image of a 17 nm Ag nanoparticle. This image was taken before the onset of nanocompression. The darker area in the center of the image is where the two particles overlap

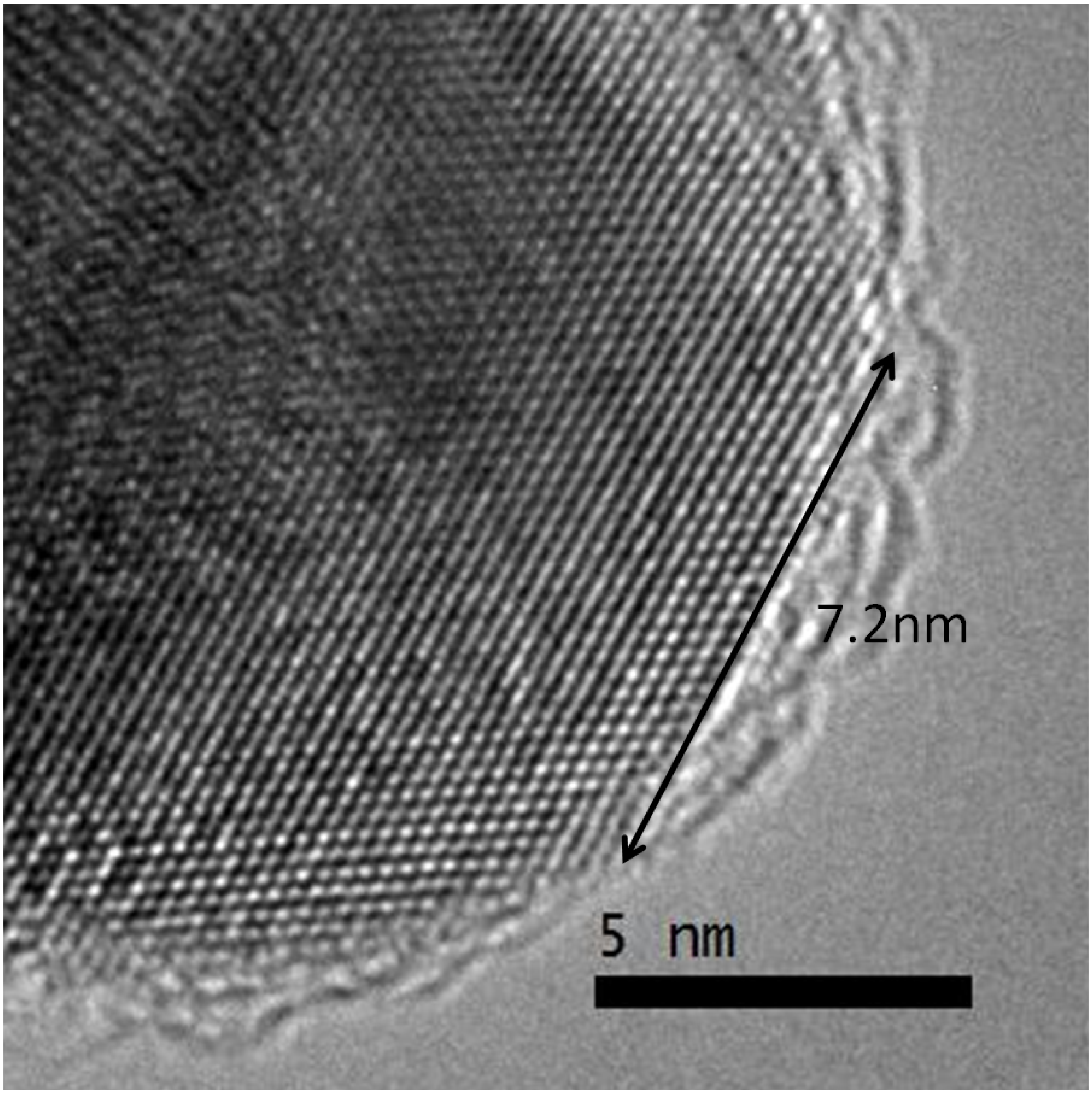

Figure 3.33: Aberration-corrected TEM image of Figure 3.32 at higher magnification. The figure also shows that the length of the first monolayer on the nanoparticle is 7.2nm long.

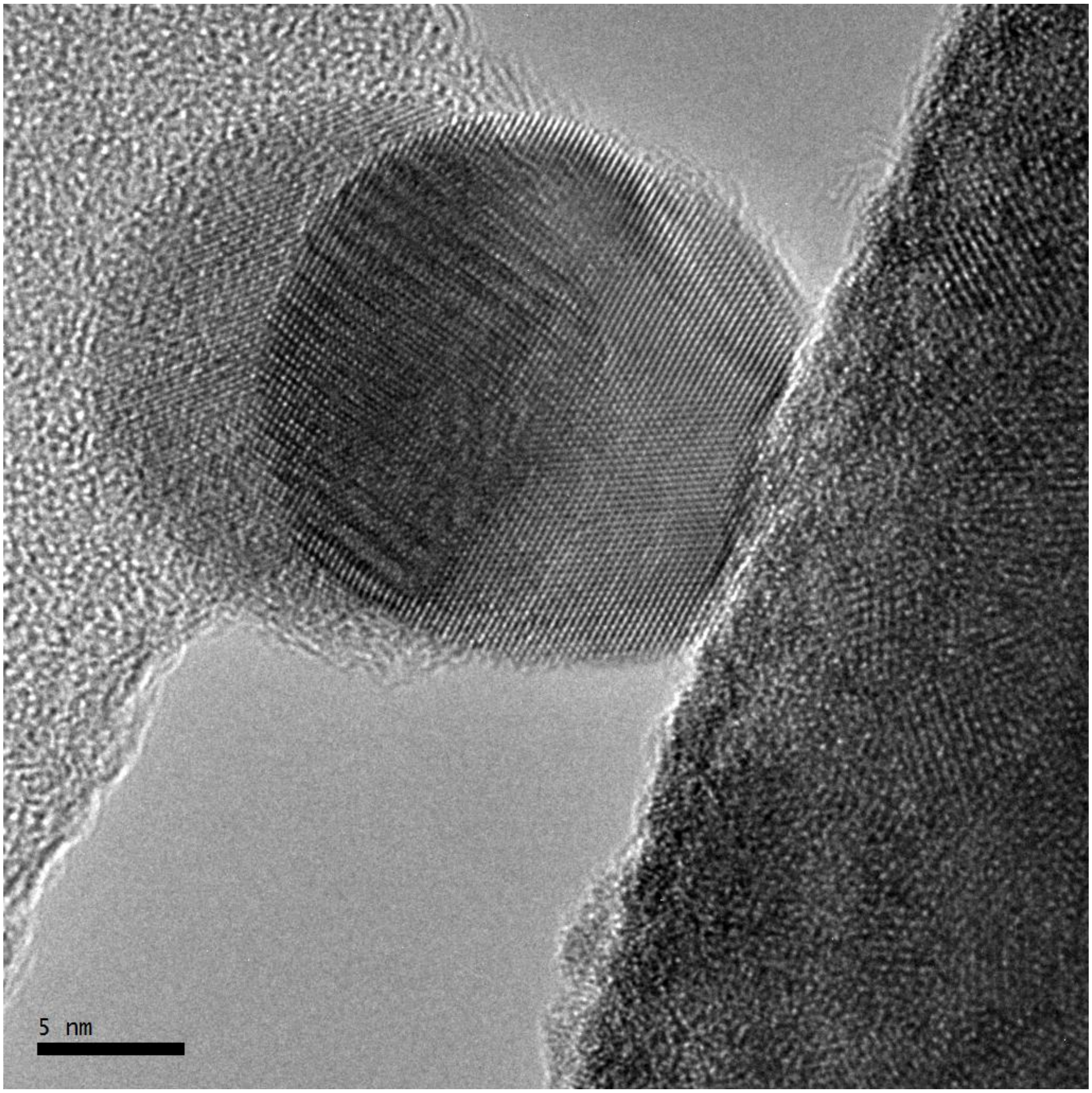

Figure 3.34: Aberration-corrected TEM image captured upon contact between the W probe and the Ag nanoparticle.

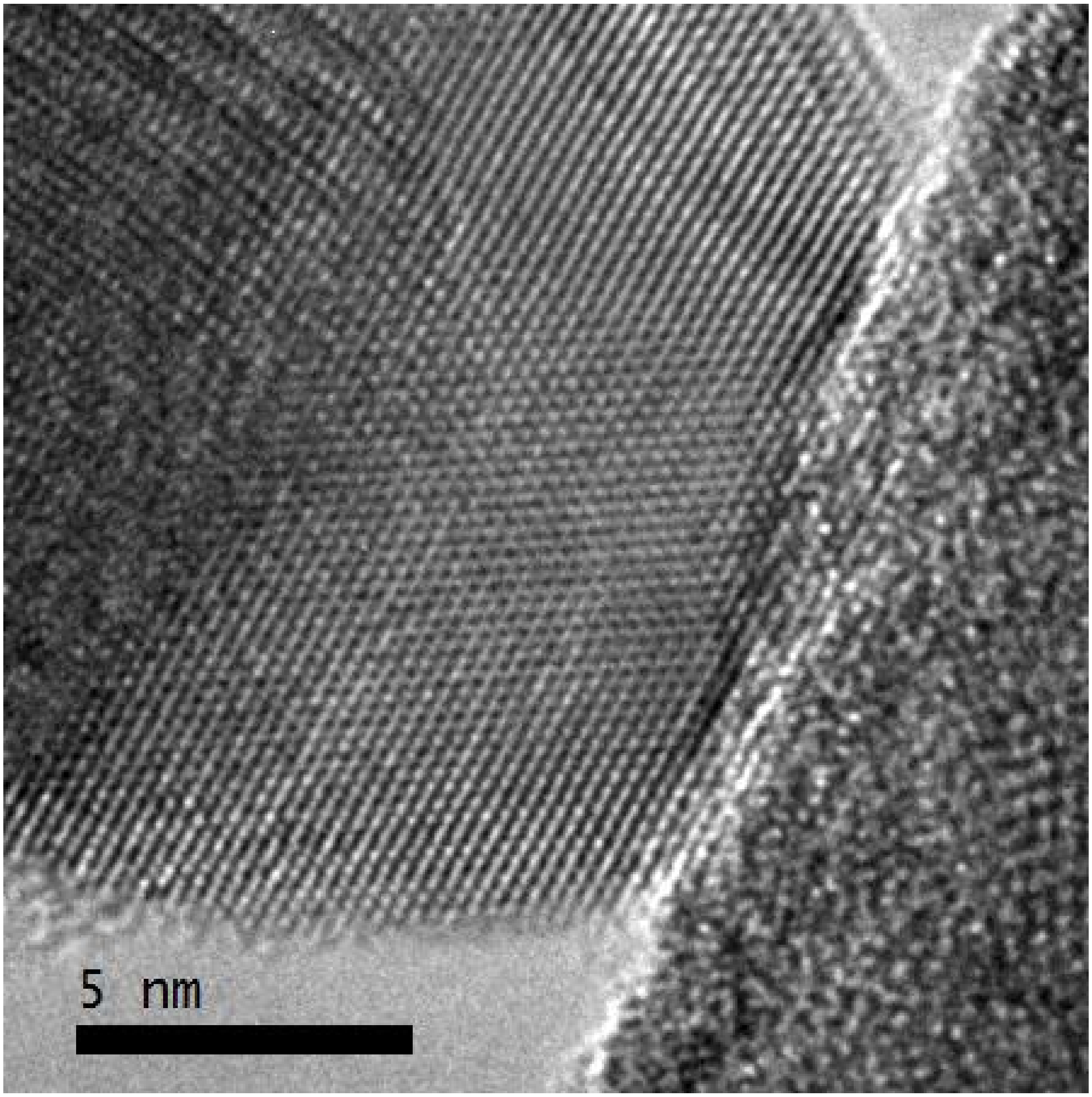

Figure 3.35: Aberration-corrected TEM image of Figure 3.34 that has been digitally magnified

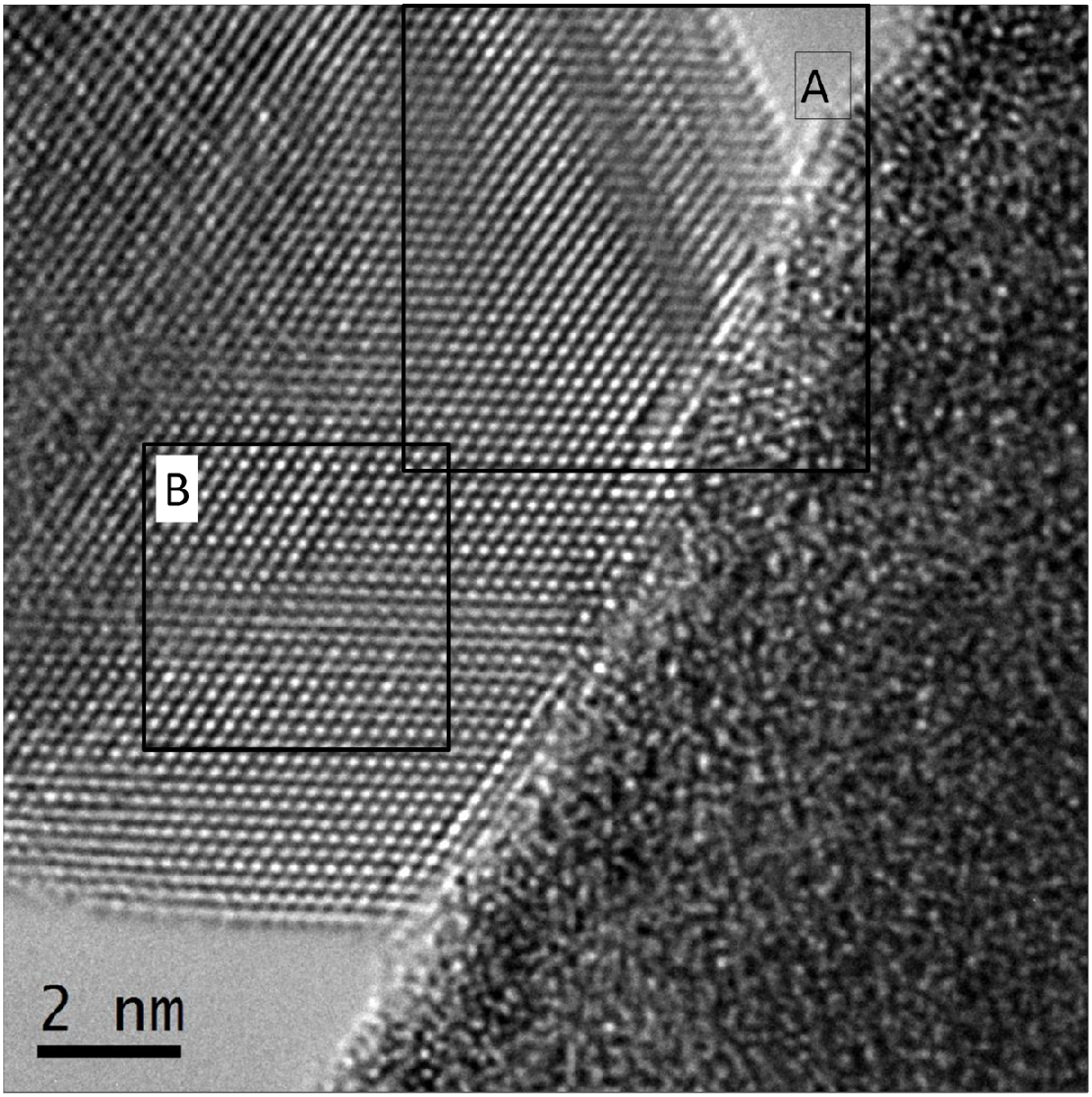

Figure 3.36: Aberration-TEM image captured after the indenter was translated further into the sample. Two areas that show the presence of dislocations, marked A and B respectively have been highlighted.

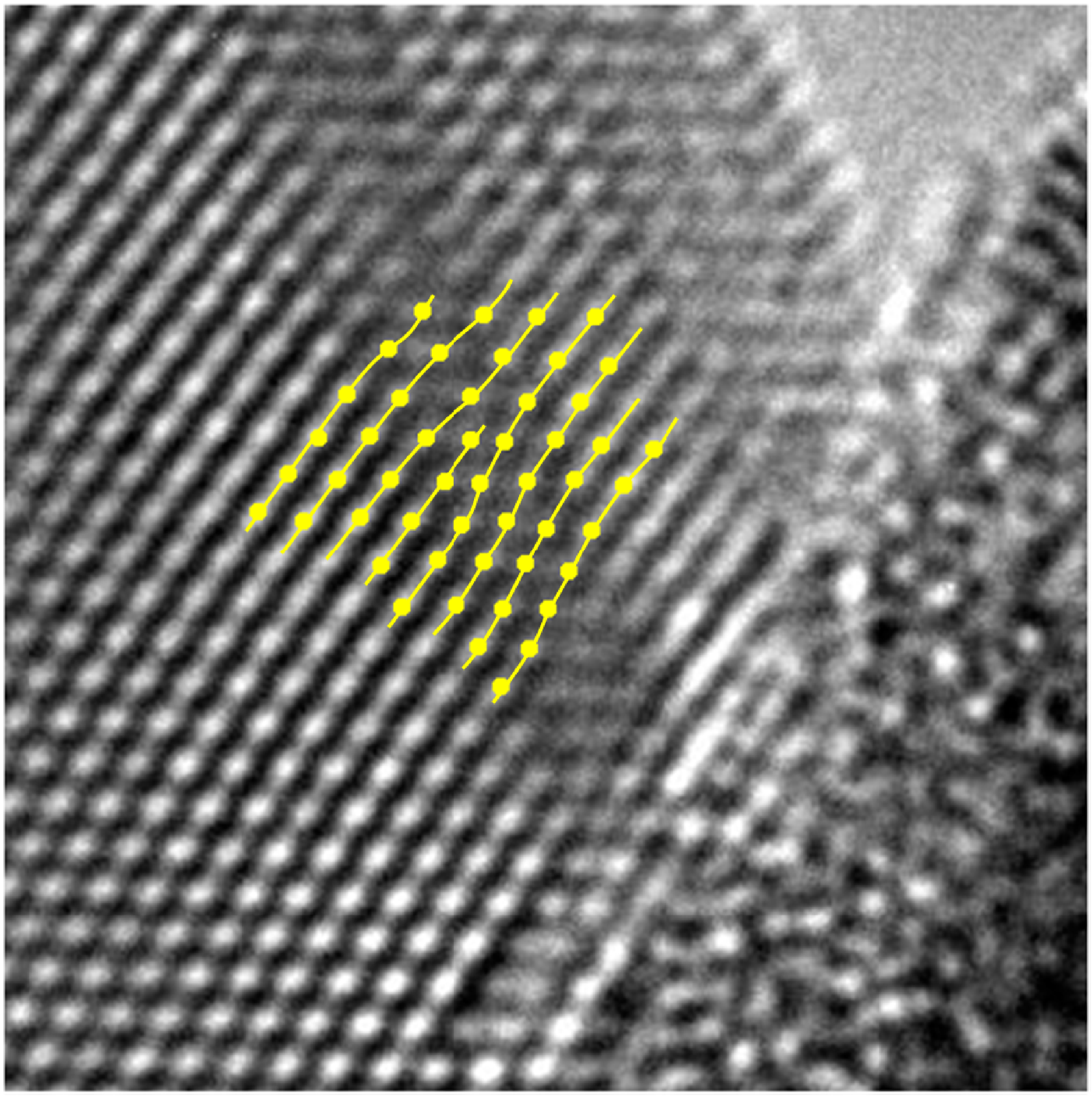

Figure 3.37: Digitally magnified view of area A from Figure 3.36. The lattice fringe that terminates in the crystal indicates the presence of a dislocation.

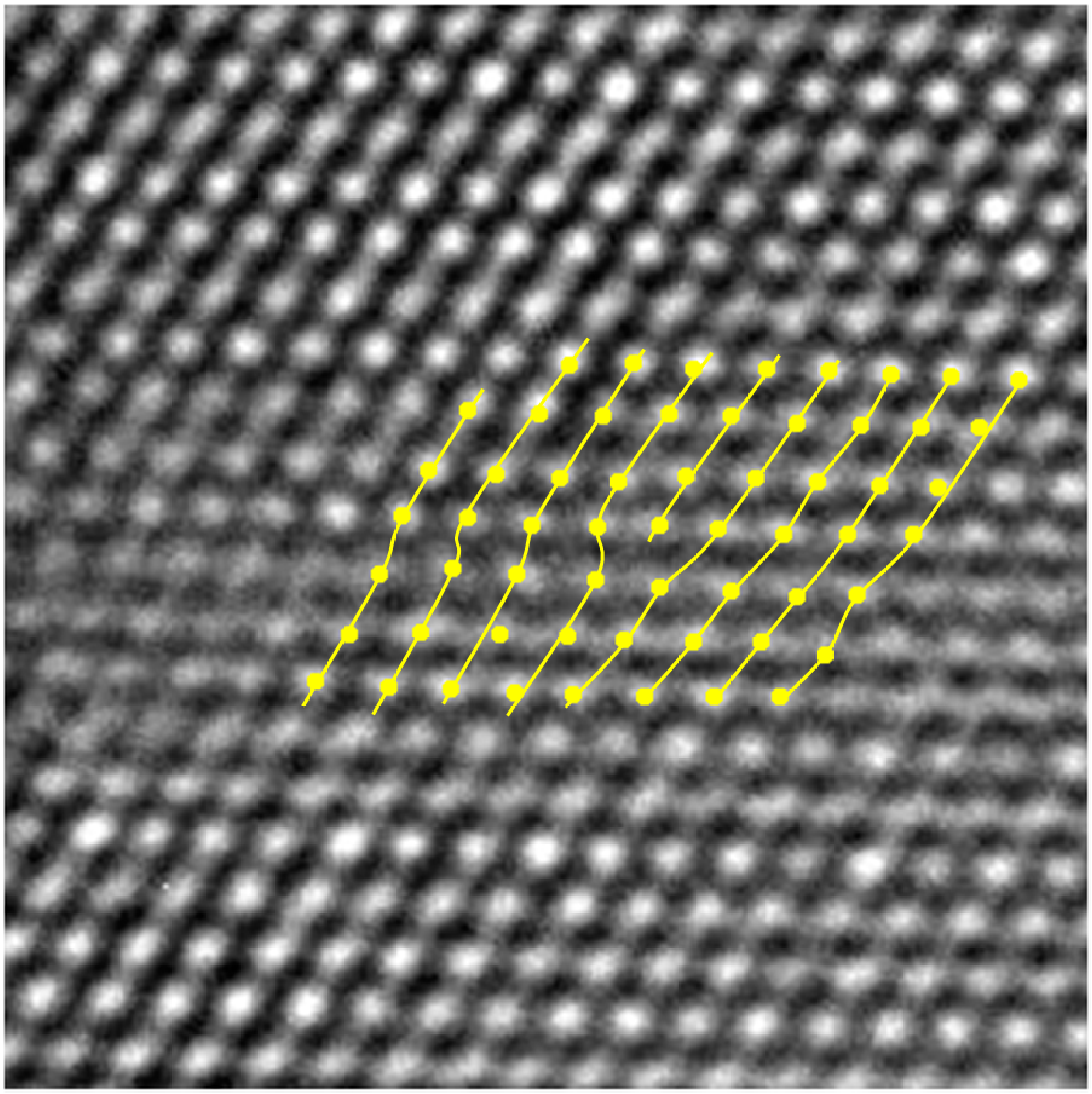

Figure 3.38: Digitally magnified view of area B from Figure 3.36. Certain lattice fringes are highlighted for emphasis. The lattice fringe that terminates in the crystal indicates the presence of a dislocation.

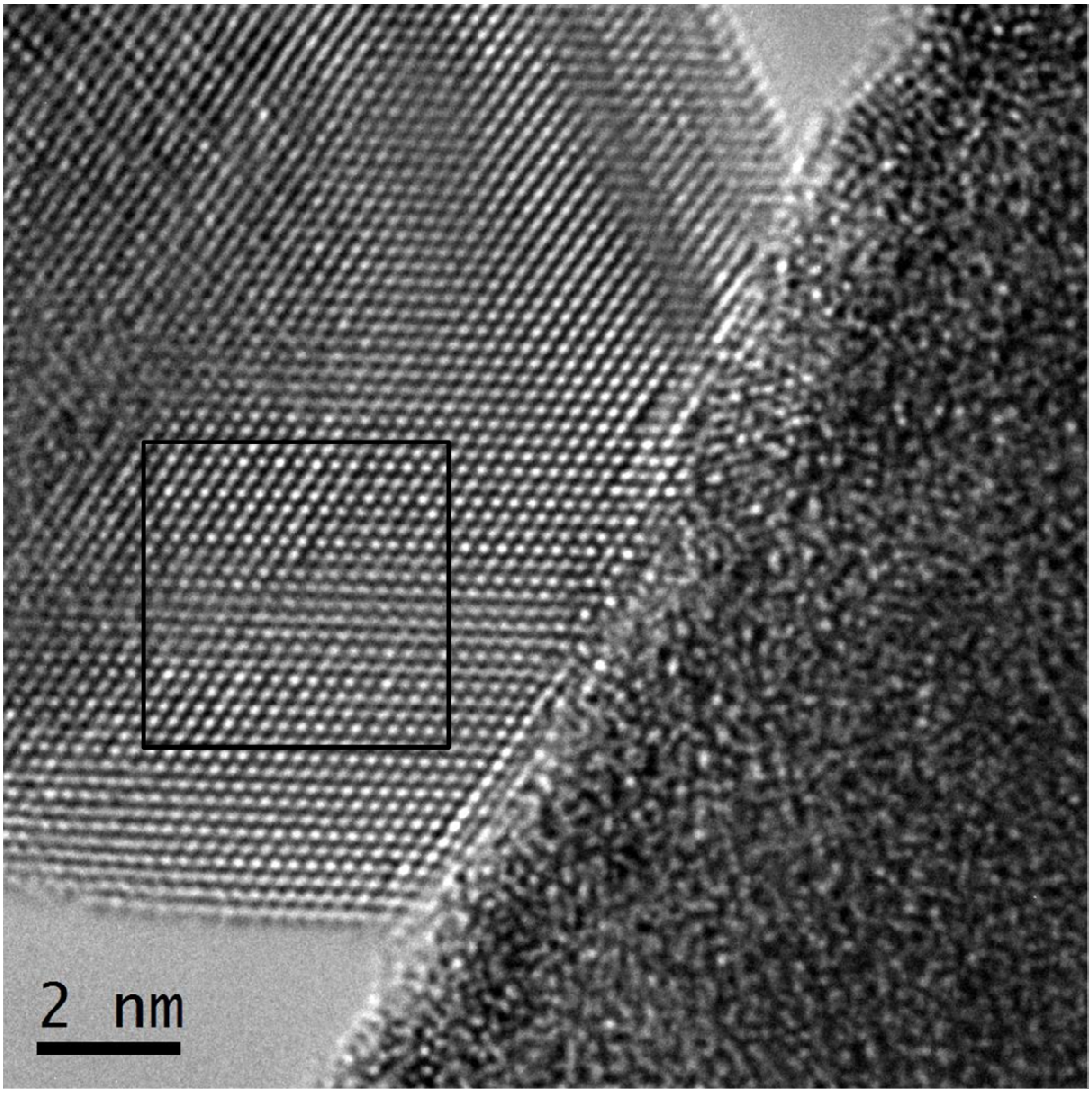

Figure 3.39: Aberration corrected TEM image captured after the indenter was translated further towards the sample. An area containing a dislocation is highlighted.

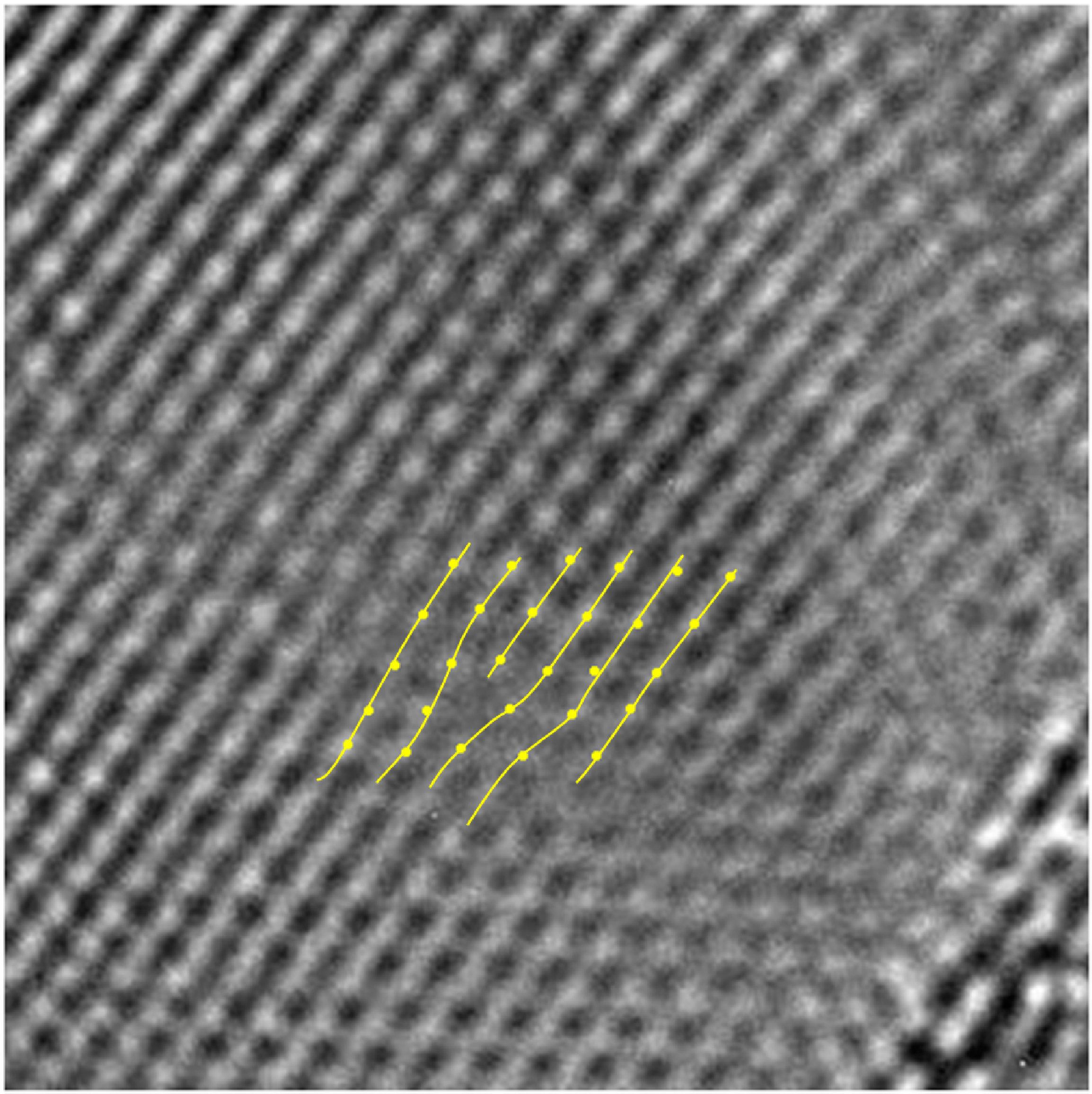

Figure 3.40: A digitally magnified of image of the highlighted area of Figure 3.39. The lattice fringe that terminates in the crystal indicates the presence of a dislocation.

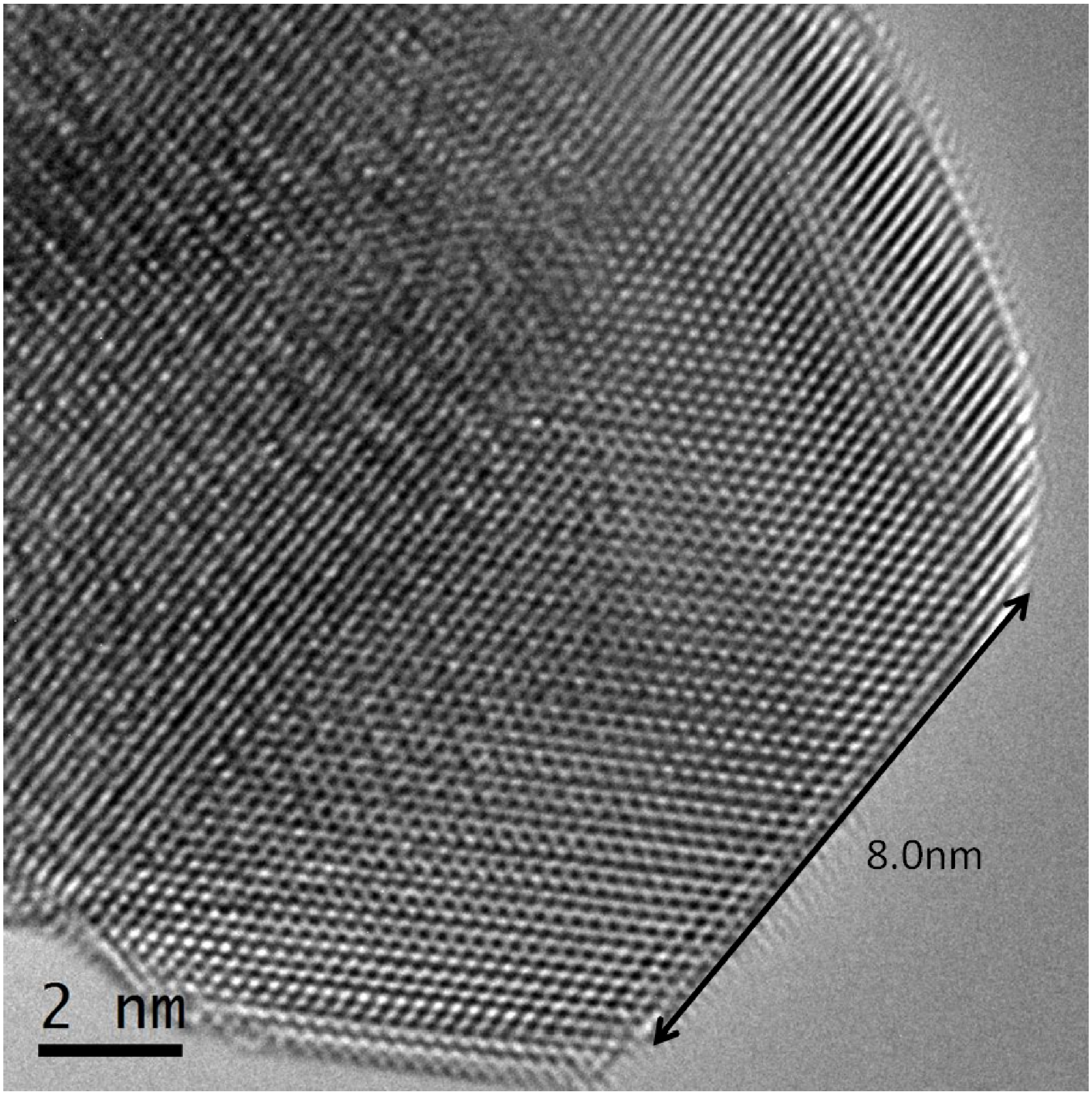

Figure 3.41: Aberration corrected TEM image of the nanoparticle after the probe was translated away from the sample. The length of the first monolayer is also shown by this figure. Compared to Figure 2.33, the first monolayer is longer in this Figure, indicating permanent deformation.

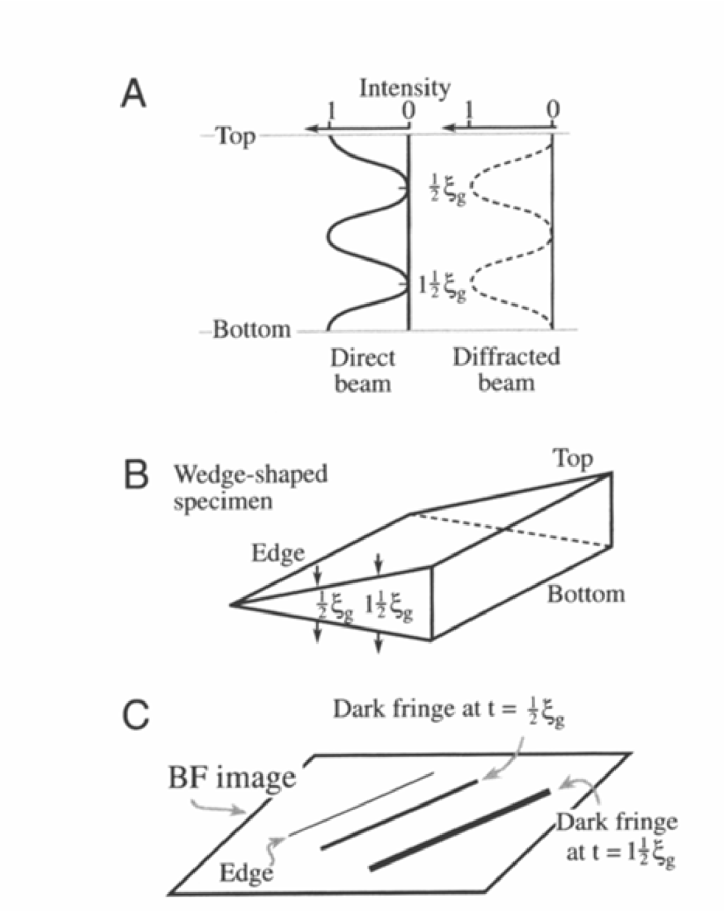

Figure 3.42: Schematic diagram showing the formation of thickness fringes [Williams and Carter]. Figure 3.42A shows who the intensities of the direct beam and the diffracted beam change as a function of material thickness. Figure 3.42B schematically shows a wedge shaped sample and Figure 3.42C shows the changes in contrast caused the changing thickness.

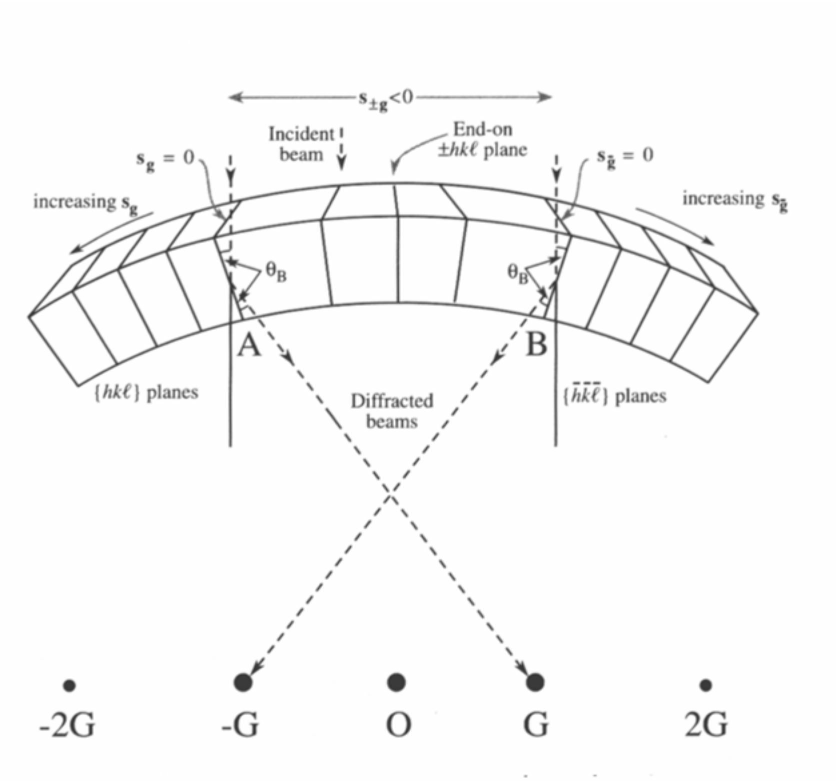

Figure 3.43: Schematic diagram of the formation of bend contours.

[Williams and Carter]

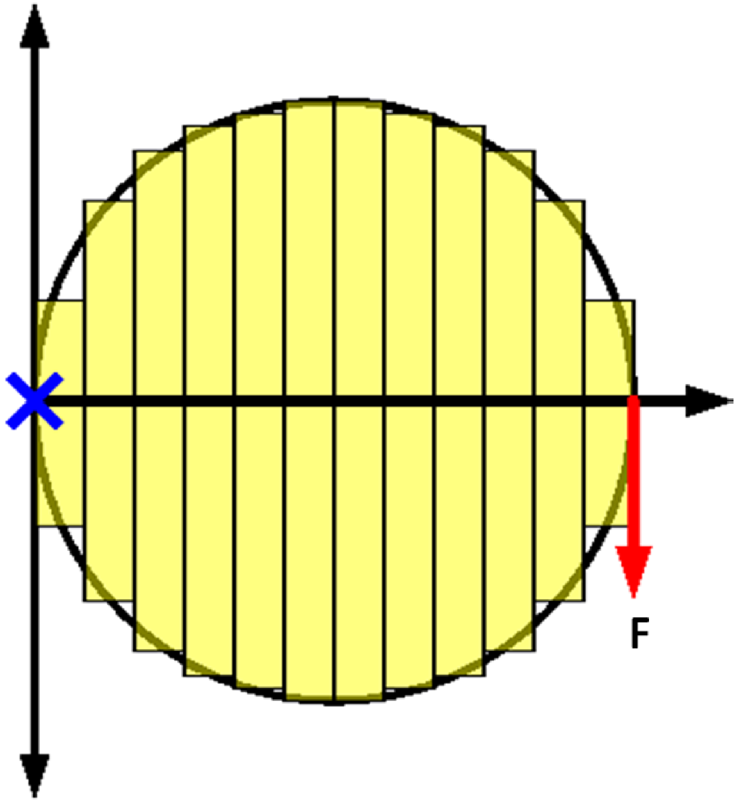

Figure 3.44: A schematic diagram of the numerical model for calculating the bending of a cantilevered sphere. A series of cantilevered disks is considered. The sphere is considered to be fixed at the point marked by the blue x, and the bending force, marked by the blue line, is considered to be collinear with the electron beam.

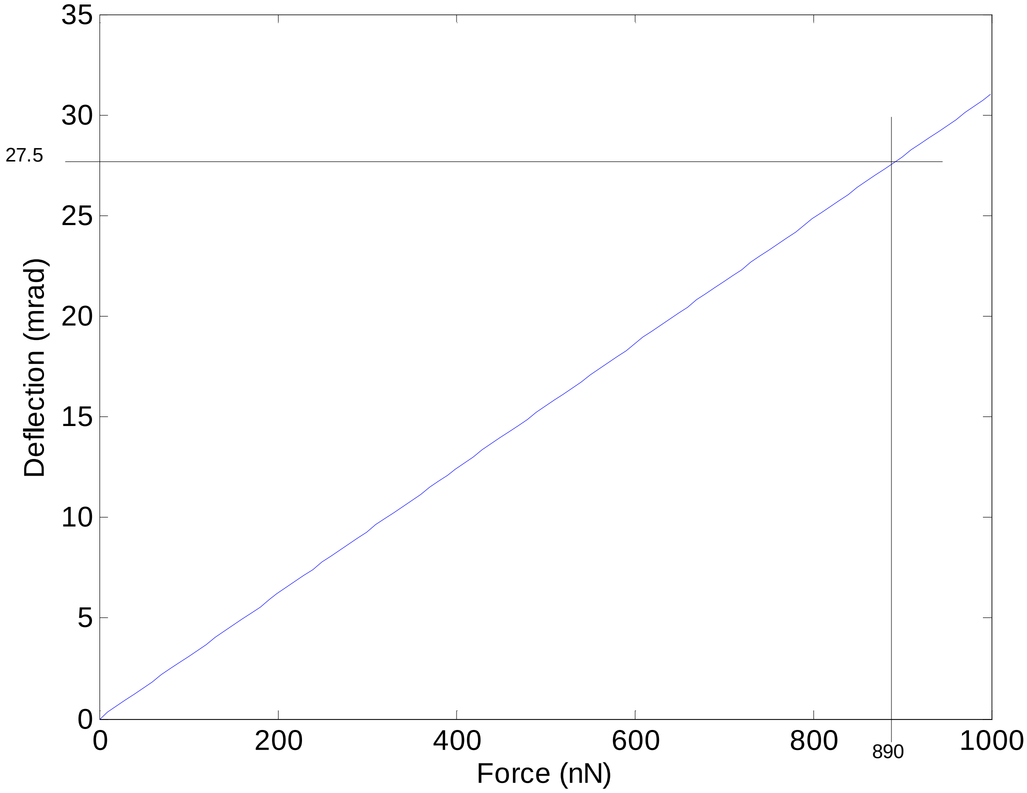

Figure 3.45: Deflection vs. applied force far a cantilevered Ag sphere with a 50nm diameter. The horizontal line indicates the deflection required to form 3 bend contours. The horizontal line is the force required to achieve this deflection.

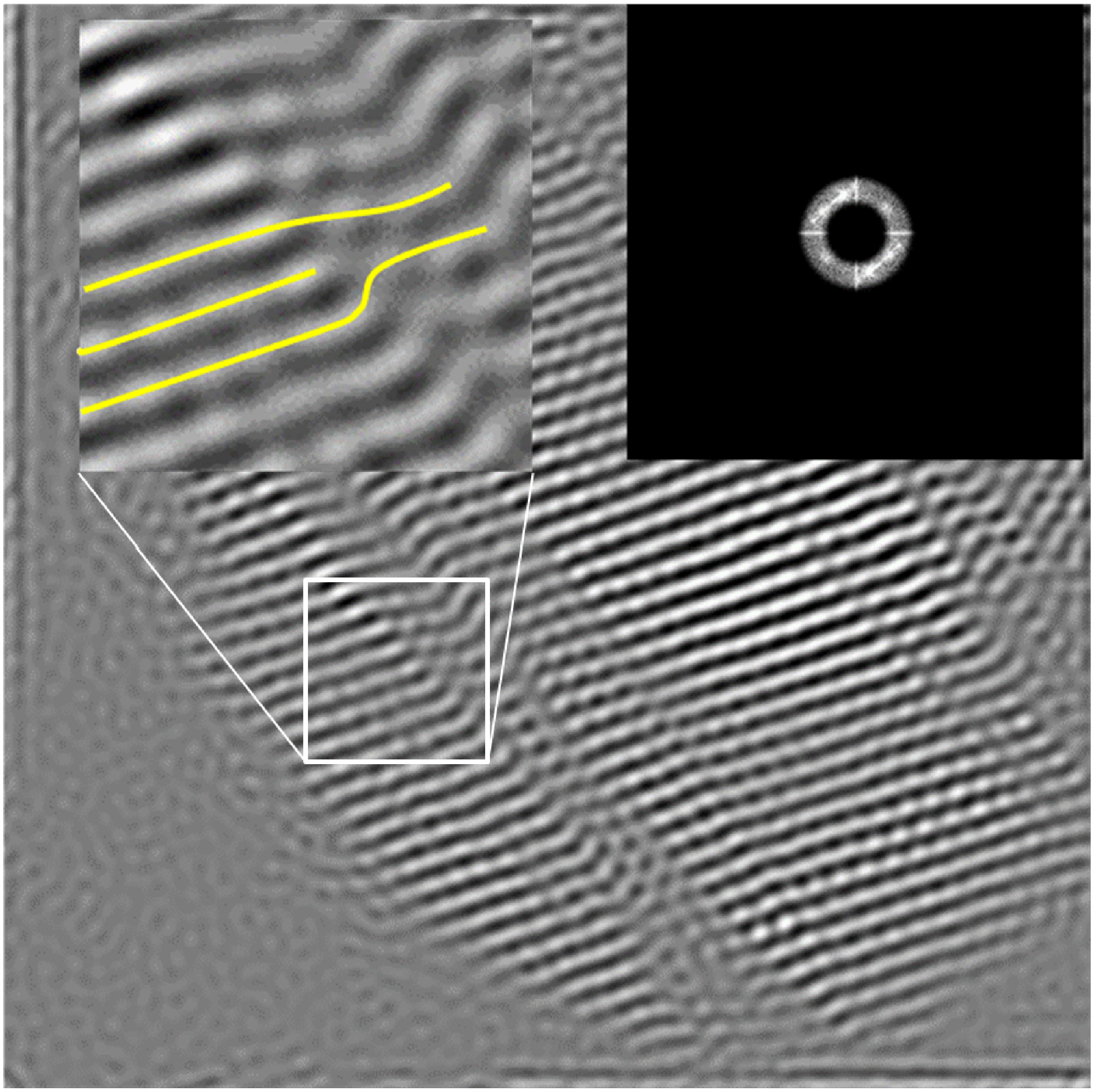

Figure 3.46: Fourier Filtered image of Figure 3.27 made by from the all g vectors with a length corresponding to the (111) planes of Ag. The inset shows the terminating plane associated with the dislocation shown in Figure 3.27.

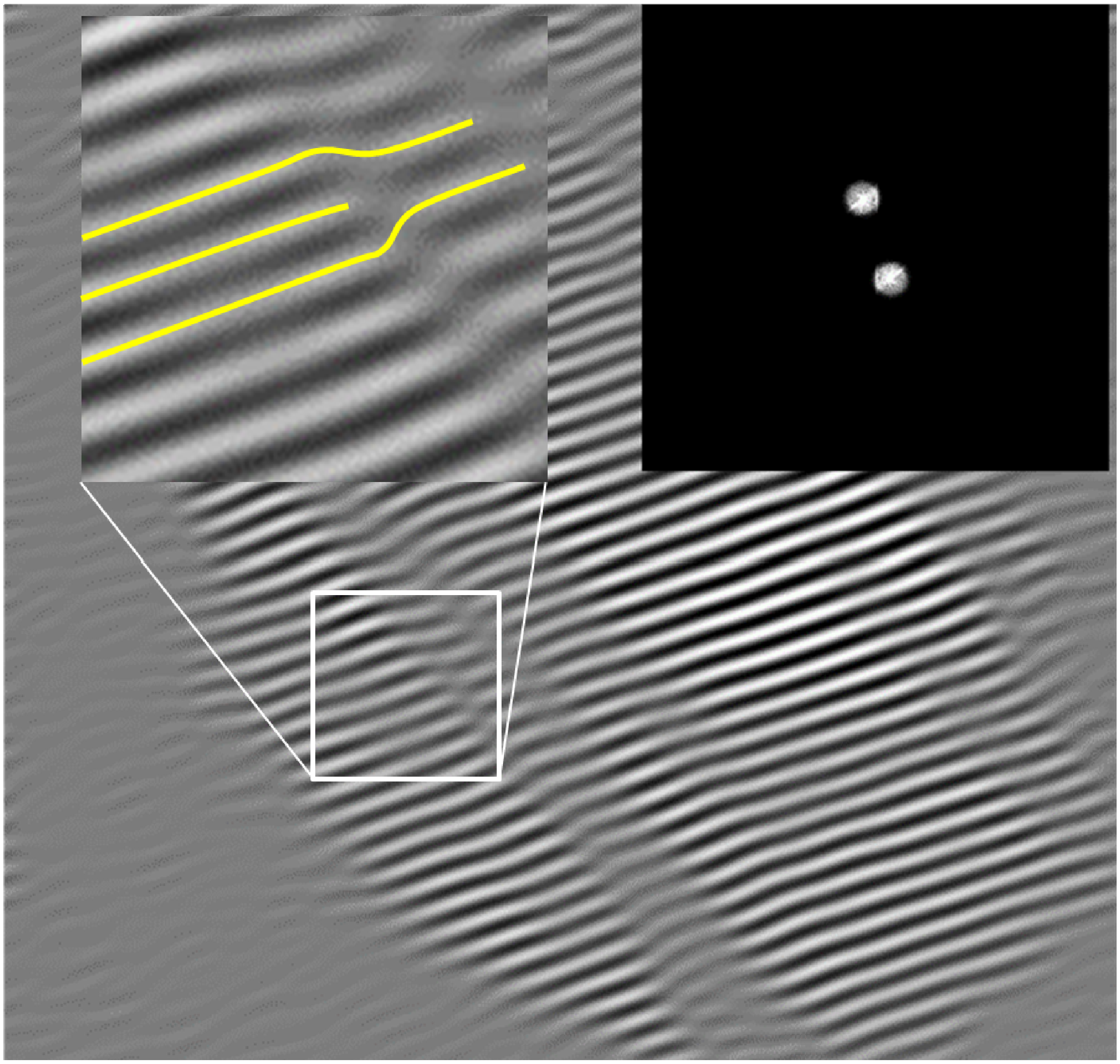

Figure 3.47: A Fourier Filtered image made from Figure 3.27 using only the g vector associated with the prominent (111) lattice fringes from the image. The terminating lattice plane in the inset is still present, confirming the presence of a dislocation.

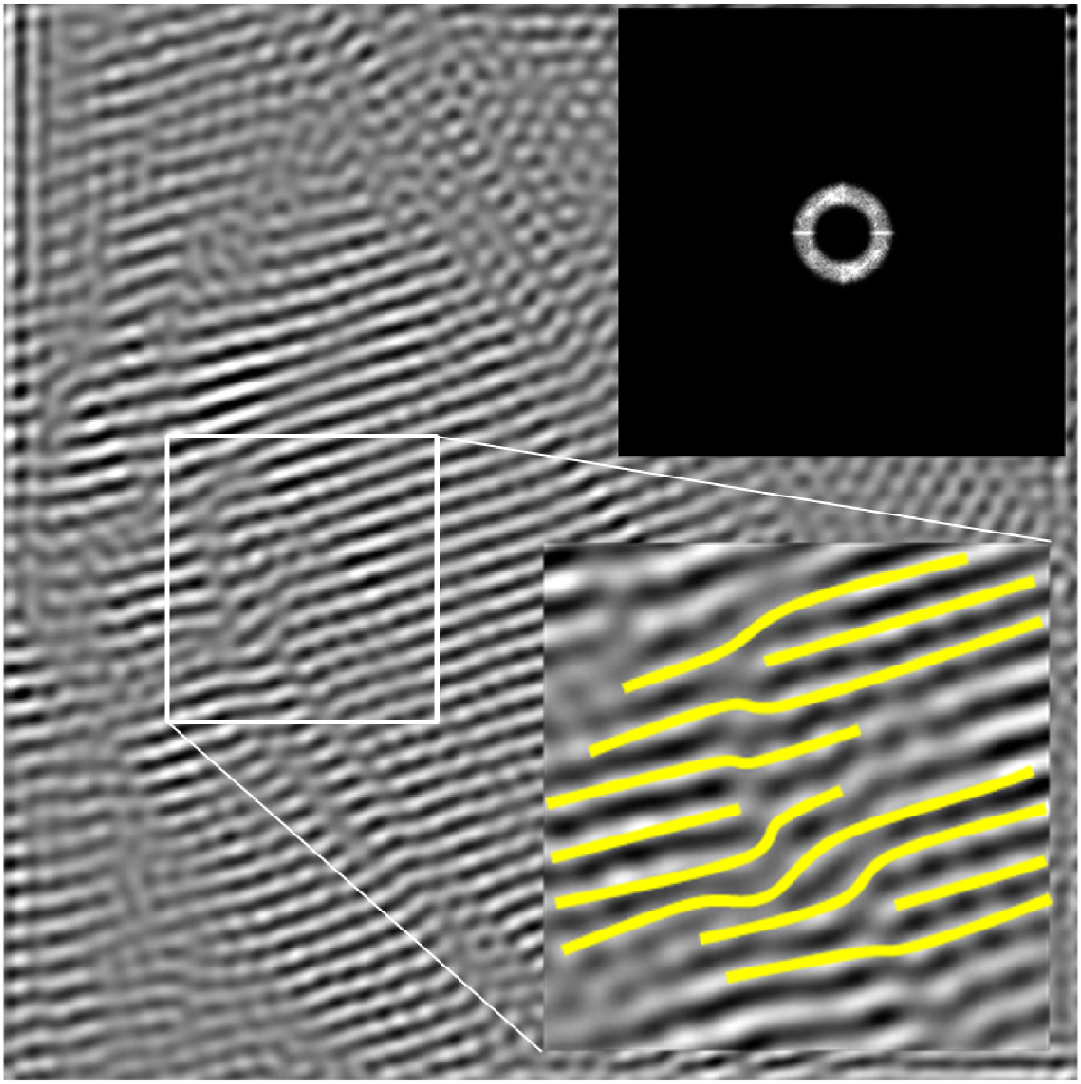

Figure 3.48: A Fourier filtered image made from Figure 3.29 by using all g vectors with a length corresponding to the (111) planes of Ag. Notice that the terminating planes indicated in the inset are still present. Additionally, another plane terminating plane is also seen. The new plane would correspond to a dislocation with an opposite sign as the other two.

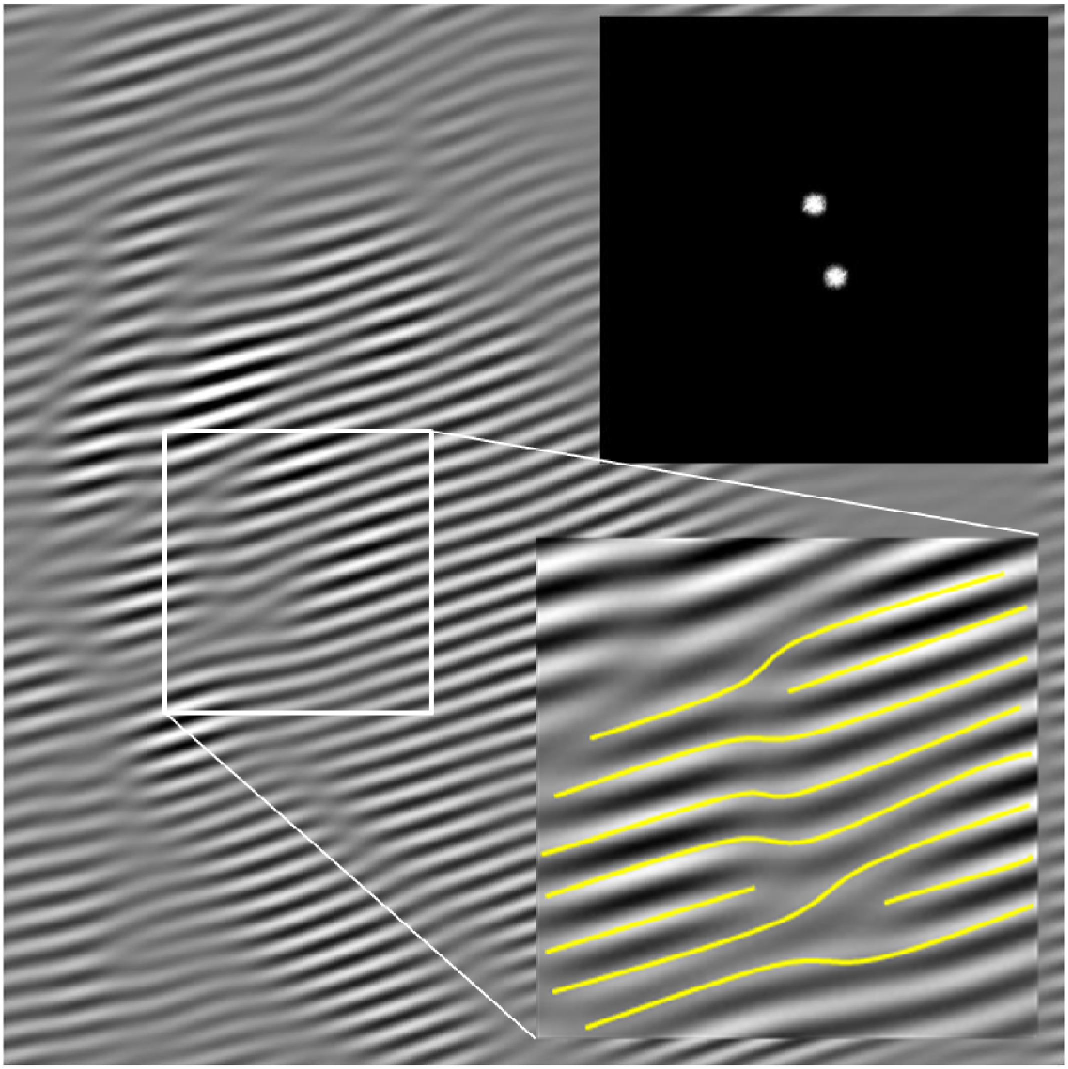

Figure 3.49: A Fourier Filtered image made from figure 3.29 using only the g vector associated with the prominent (111) lattice fringes from the image. Notice, once again the terminating lattice planes that was highlighted in figure 3.29 are still present, but the plane reappears near the edge of the particle. All of the terminating planes are shown in the inset,

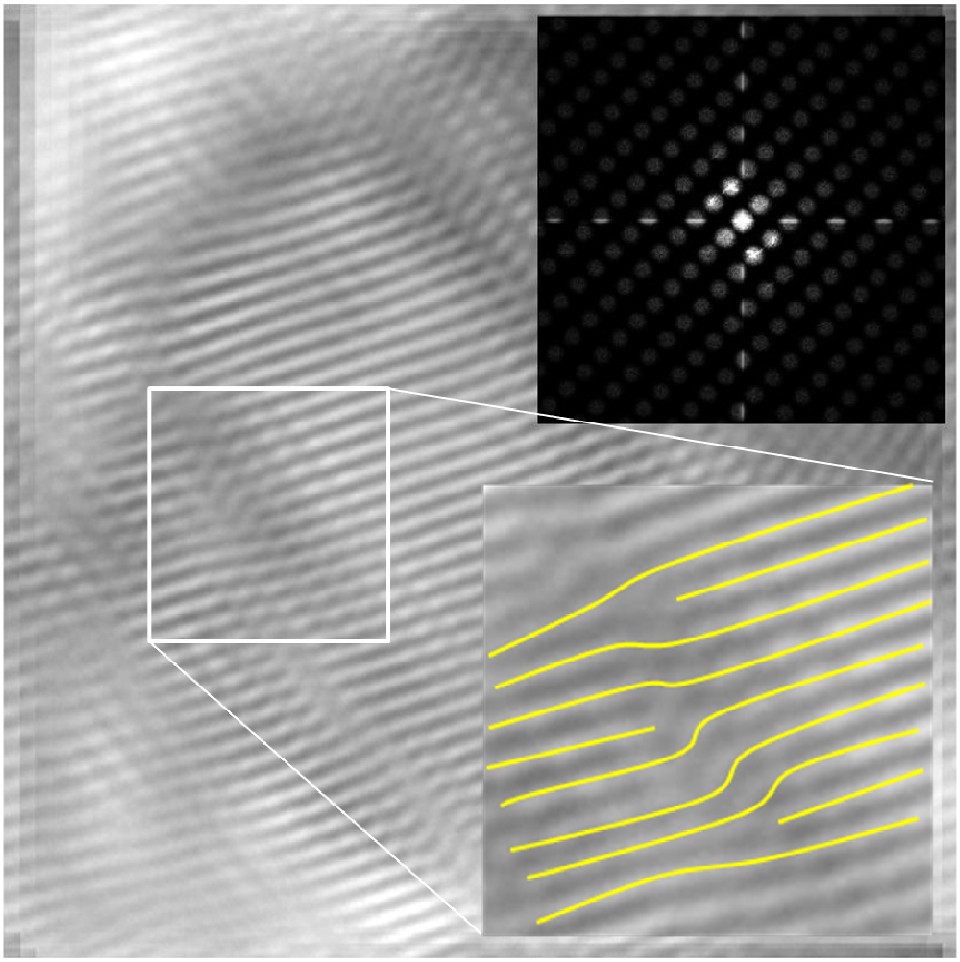

Figure 3.50: A Fourier filtered image formed from image 3.29 using an array of (111) type spots. The terminating planes are shown in the inset. This figure shows three dislocations. If a Burgers circuit were done around two of the dislocations with opposite signs, there would be a zero Burgers vector. This could imply that the terminating fringes were artifacts caused by either change in thickness of Moiré fringing. Regardless, the figure shows the presence of at least one dislocation.

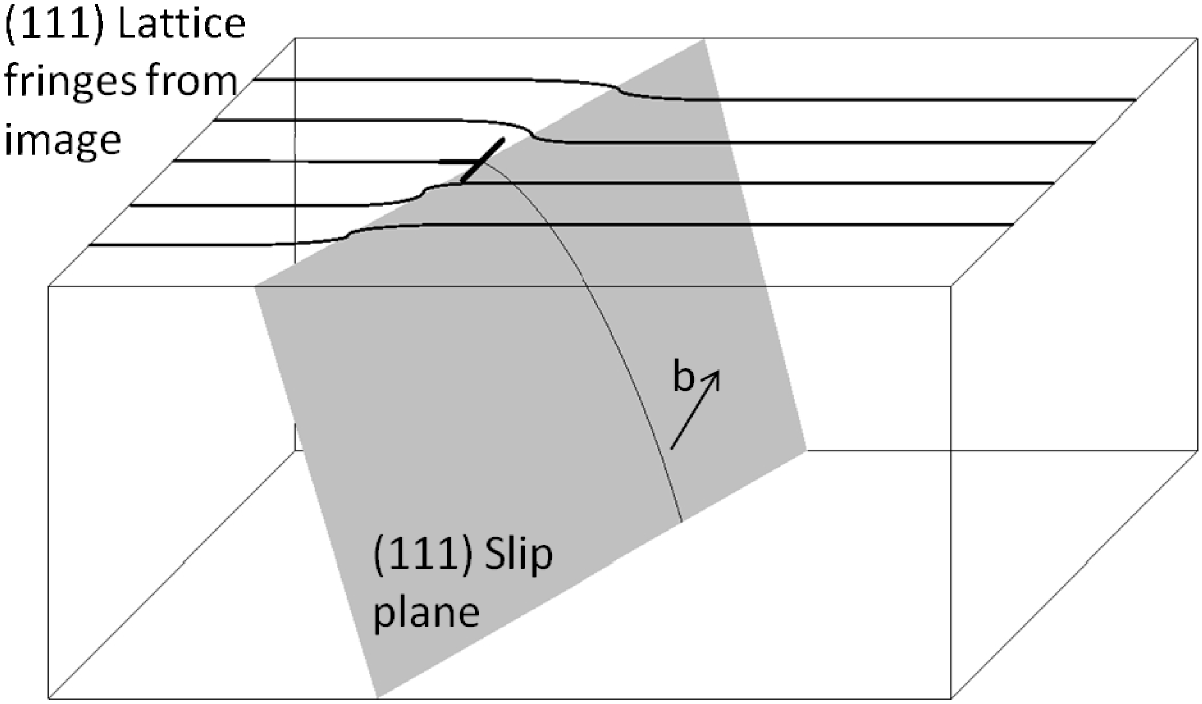

Figure 3.51: A schematic diagram of the relationship between the image and the dislocation in the high resolution nanoindentation experiments. (111) lattice fringes are imaged, but the dislocation exists on a different (111) slip plane at an angle with image's (111) lattice fringes.

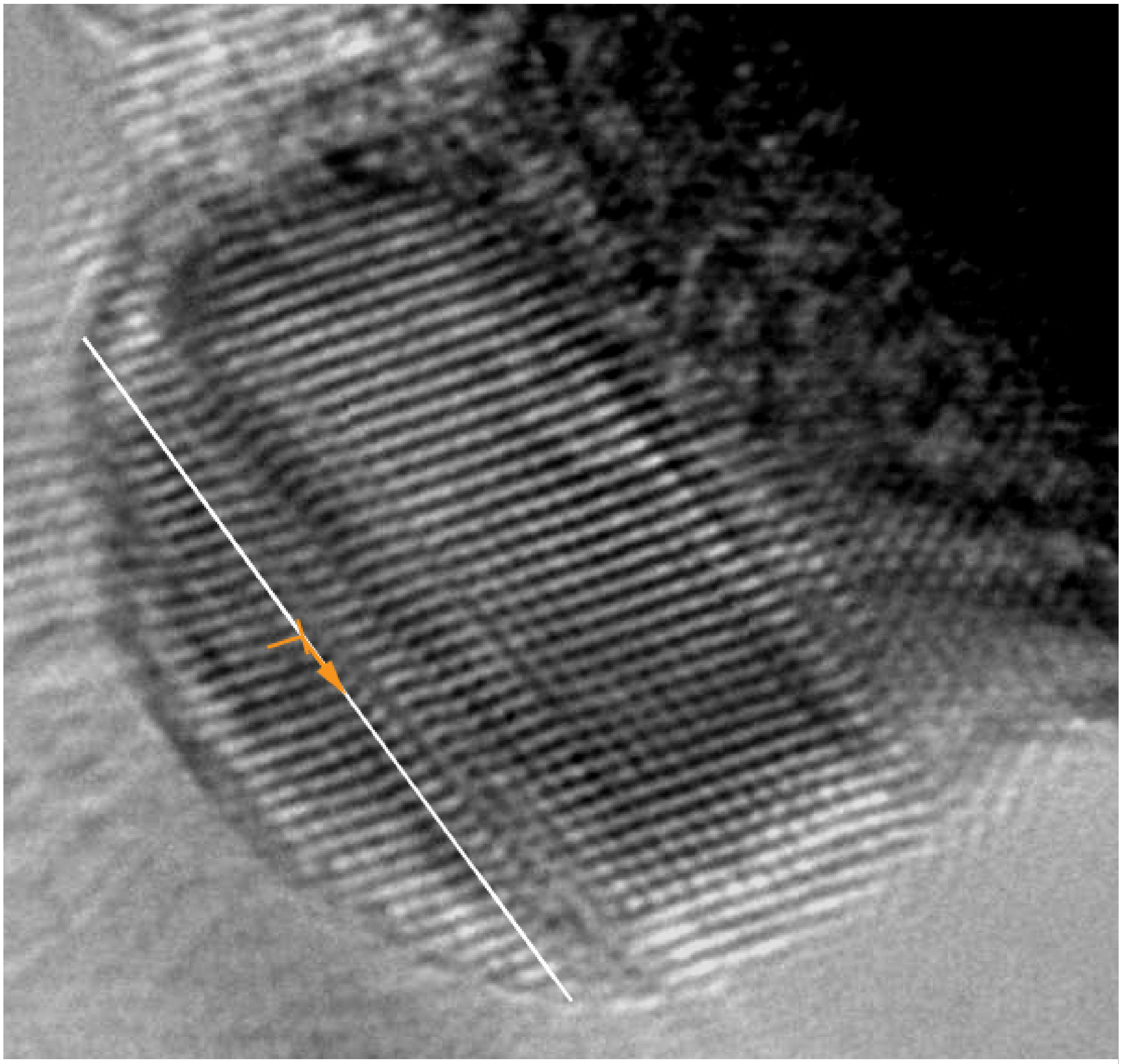

Figure 3.52: TEM image showing the dislocation and its slip plane. Notice that the slip plane is not at a right angle with the lattice fringes.

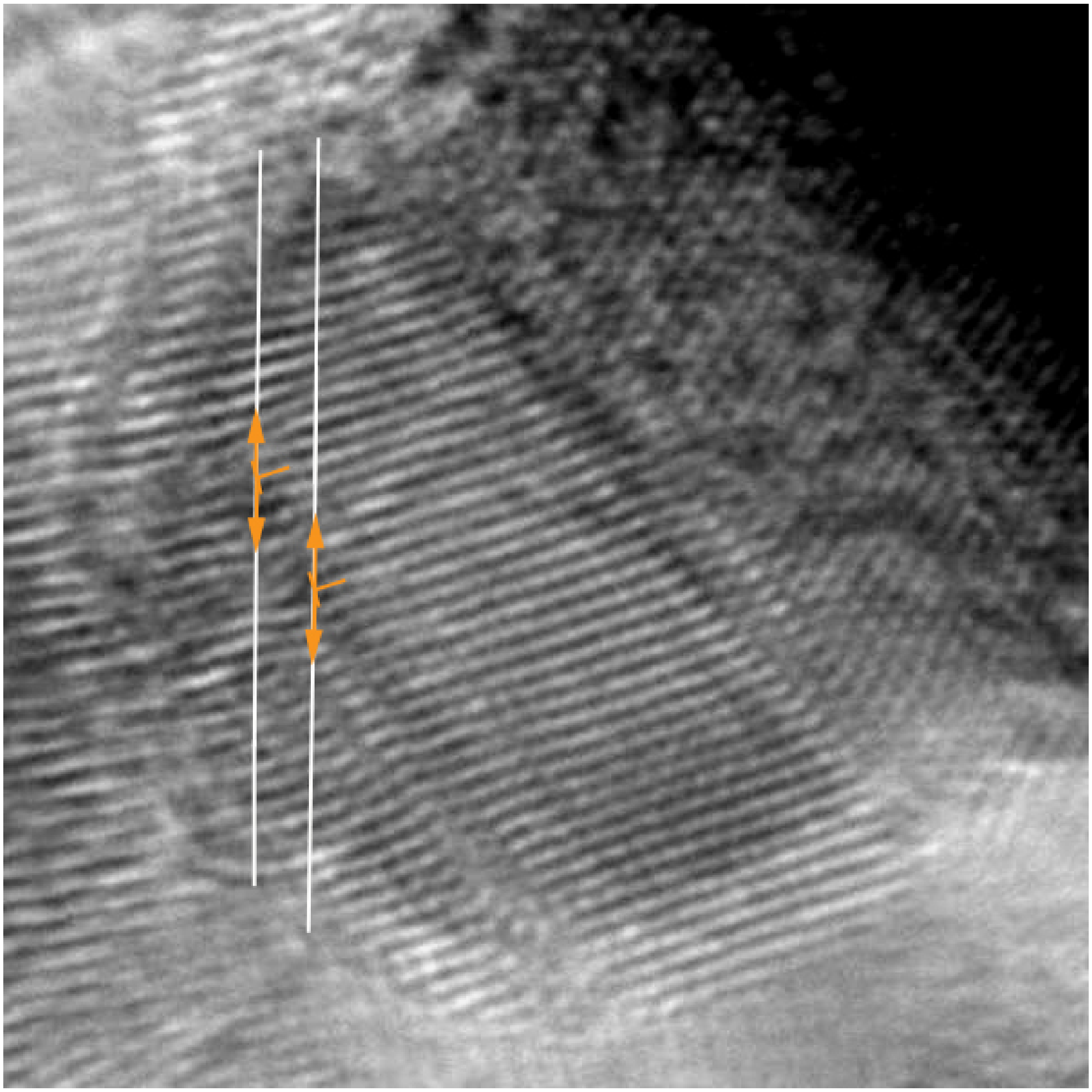

Figure 3.53: TEM image showing the dislocations and their slip planes. Notice that the slip planes are not at a right angle with the lattice fringes.

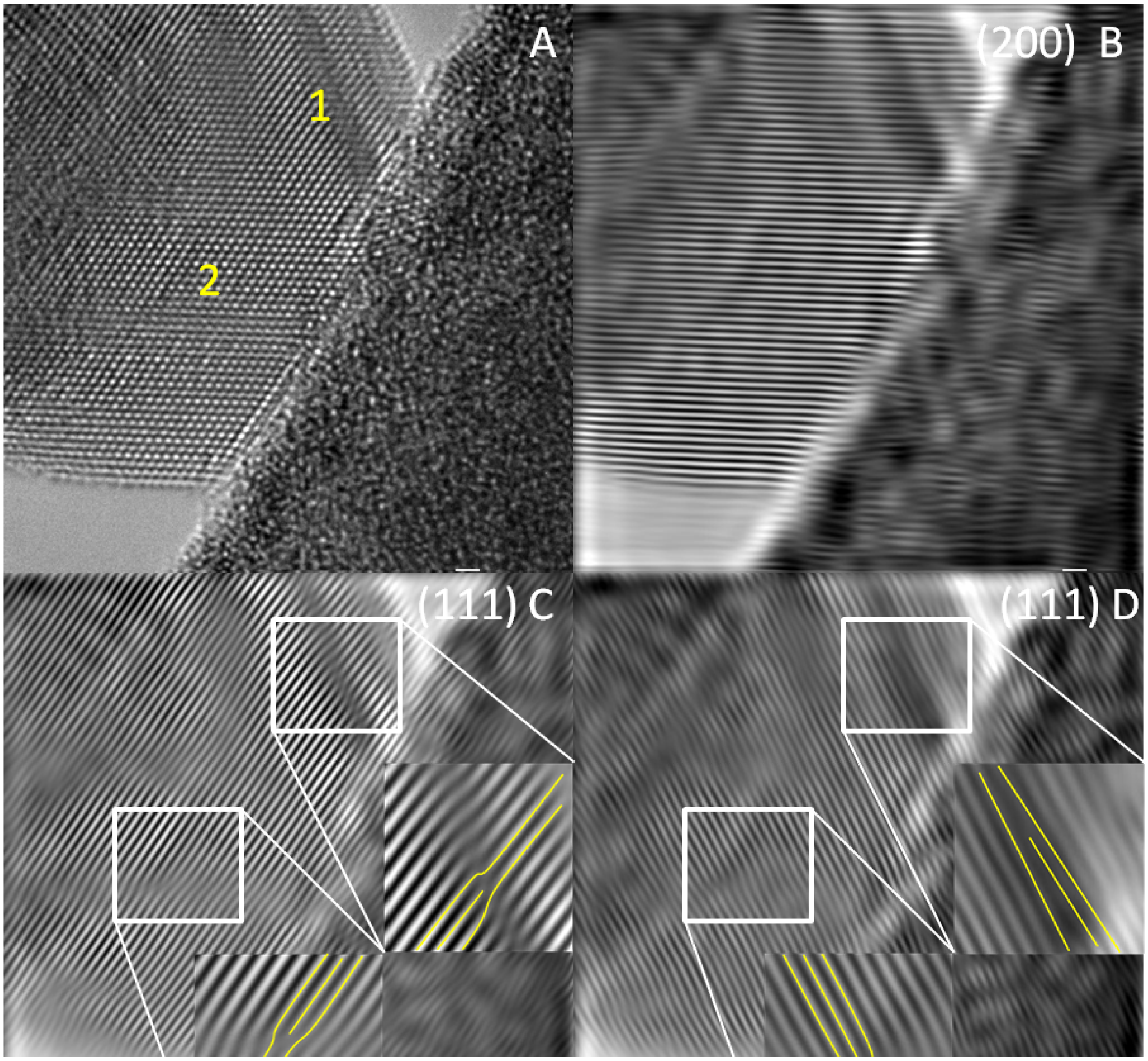

Figure 3.54: Fourier filtered images of figure 3.36. Figure 3.52A is a reproduction of Figure 3.36. Figure 3.54 B is a Fourier filtered image made using the (200) FFT spots and Figure 3.54 C and D are Fourier filtered images made using two different sets of (111) spots. The terminating lattice fringes are shown in the insets.

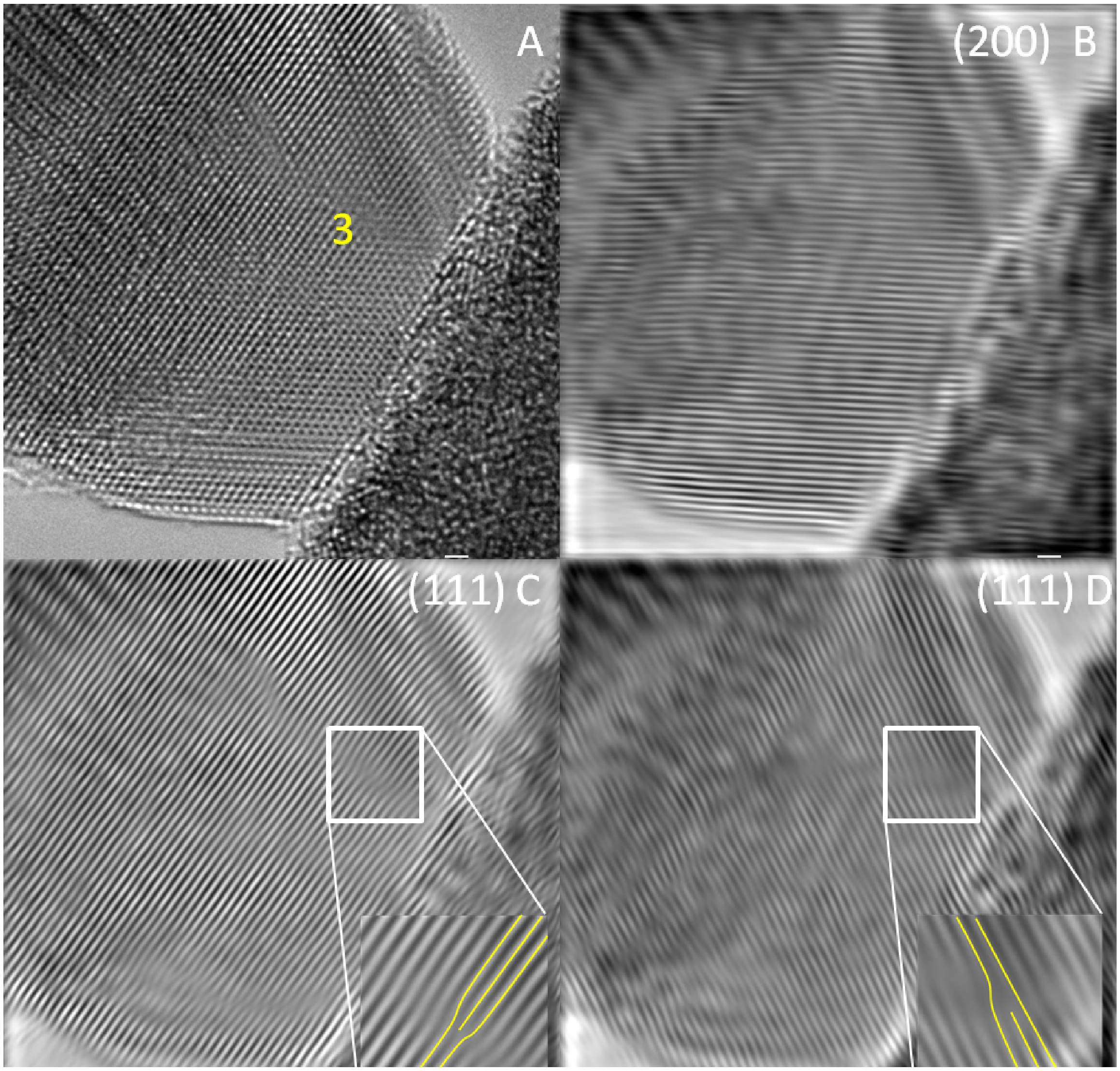

Figure 3.55: Fourier filtered images of figure 3.39. Figure 3.55A is a reproduction of Figure 3.39. Figure 3.55 B is a Fourier filtered image made using the (200) FFT spots and Figure 3.55 C and D are Fourier filtered images made using two different sets of (111) spots. The terminating lattice fringe is shown in the inset.

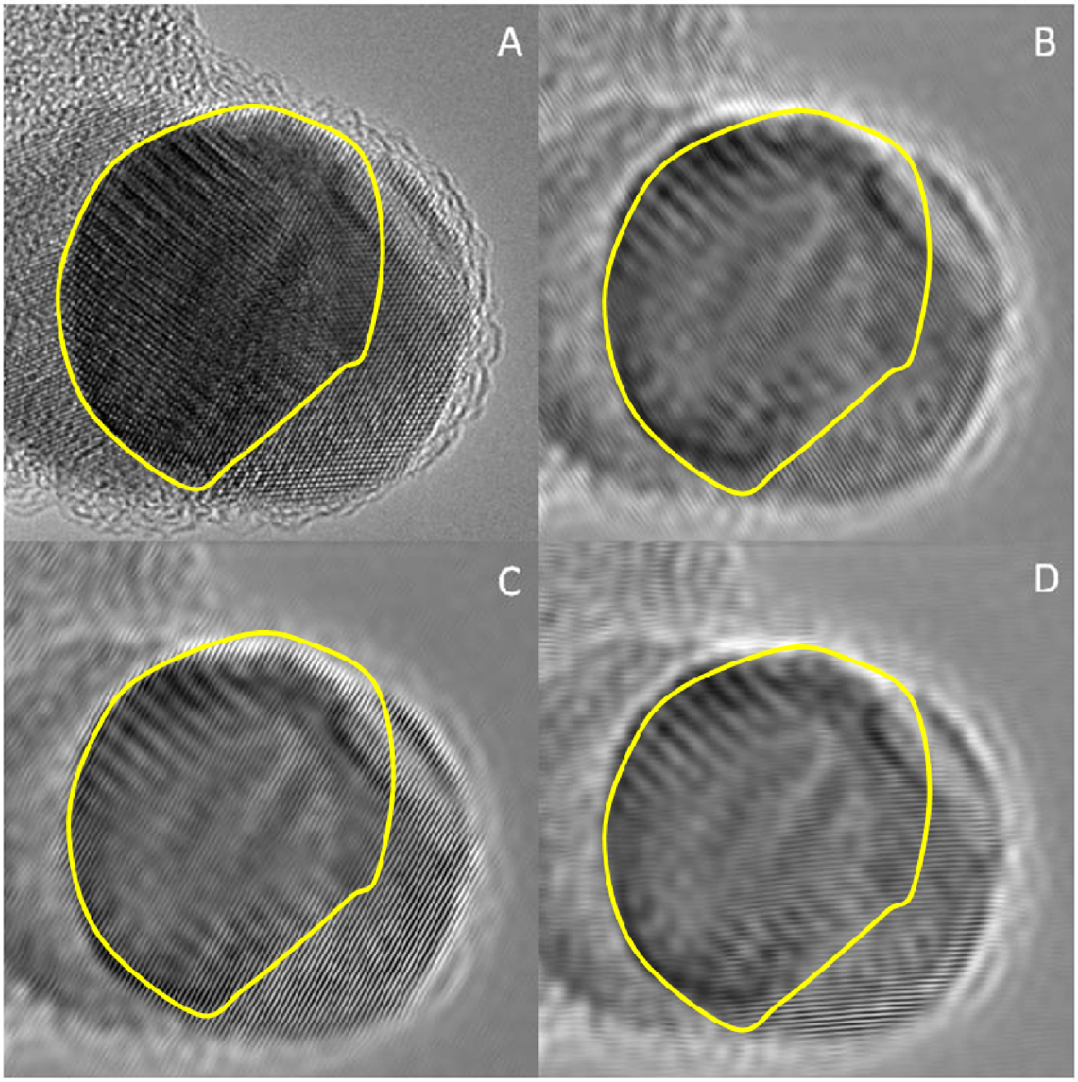

Figure 3.56: Fourier Filtered images from figure 3.32. Figure 3.56A is a reproduction of Figure 3.32. Figure 3.56 B is a Fourier filtered image made using (200) FFT spots and Figure 3.56 C and D are Fourier filtered images made using two different sets of (111) spots. The area where the particles overlap is outlined by the thick yellow line. No terminating lattice fringes are seen in this image, indicating an absence of dislocations

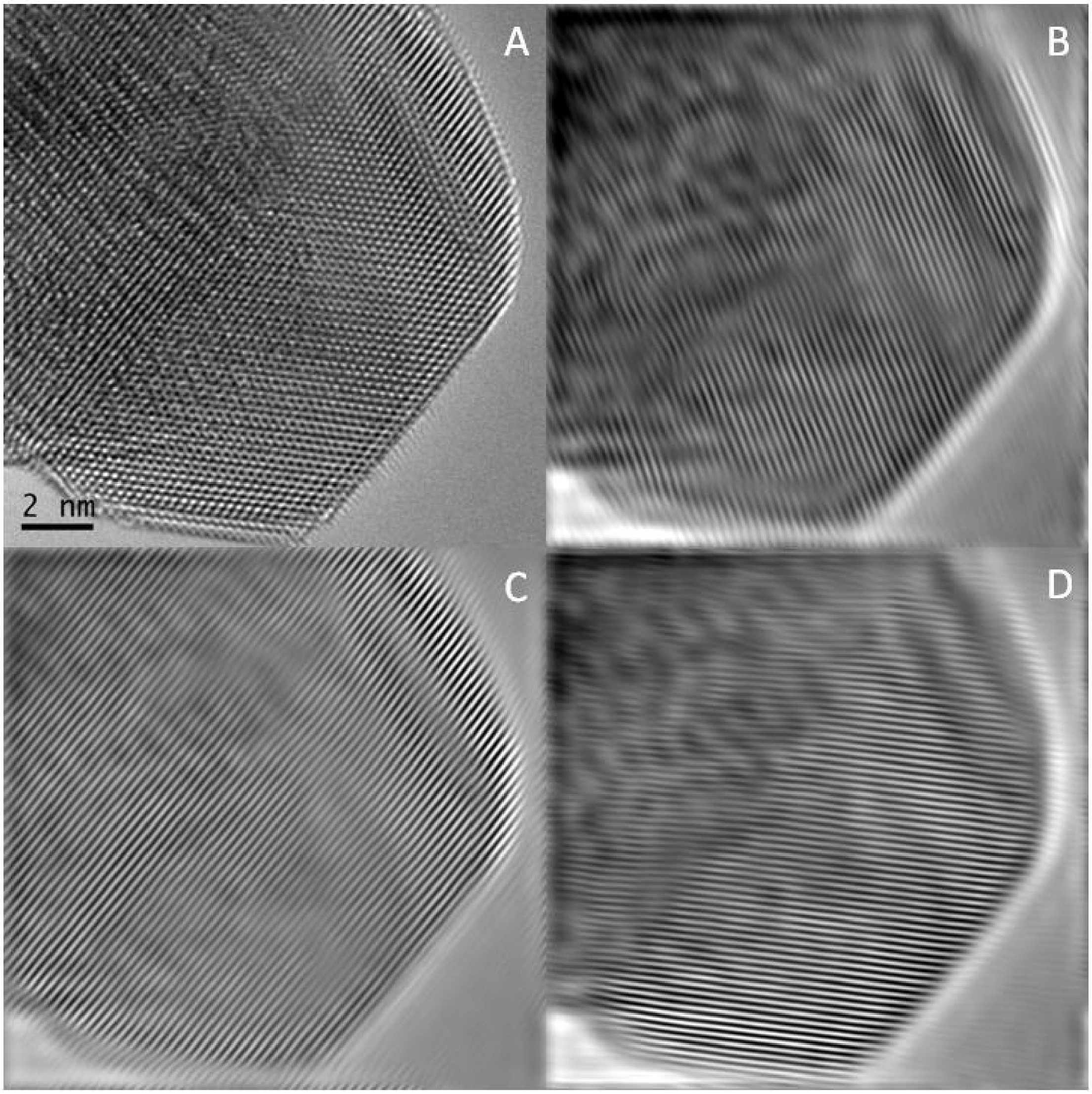

Figure 3.57: Fourier filtered images from figure 3.41Figure 3.57A is a reproduction of Figure 3.41. Figure 3.57 B is a Fourier filtered image made using (200) FFT spots and Figure 3.57 C and D are Fourier filtered images made using two different sets of (111) spots. No terminating lattice fringes are seen in this image, indicating an absence of dislocations.

Table 3.1: The physical parameters used for the dislocation nucleation calculations

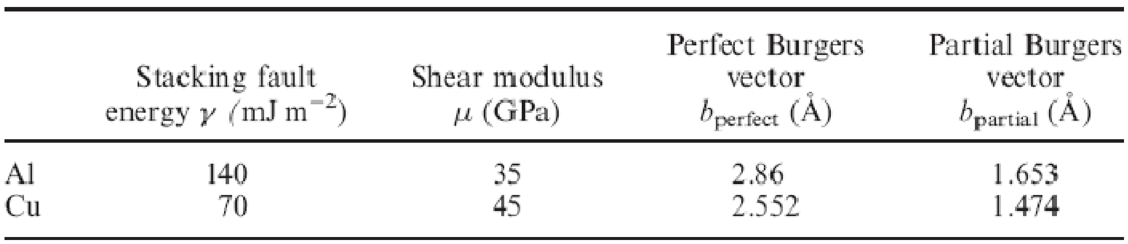

	Stacking fault energy γ (mJ m^{-2})	Shear modulus μ (GPa)	Perfect Burgers vector b_{perfect} (Å)	Partial Burgers vector b_{partial} (Å)
Al	140	35	2.86	1.653
Cu	70	45	2.552	1.474

CHAPTER 4: DEFORMATION IN 2-D AND 3-D NANOMATERIALS

4.1 INTRODUCTION

This chapter will first present a new theoretical model based on a combined dislocation and diffusion mechanism to explain the inverse Hall-Petch effect in 2-D and 3-D nanomaterials. Subsequently, the model will be applied to nanocryastalline Cu and Ni and the results and implications of the model will be discussed.

A new model explaining the IHPE is necessary because recent *in-situ* TEM results have shown evidence of dislocation motion during deformation of nanocrystalline metals [23, 24, 26, 74, 103]. This indicates that dislocations still have an important role in strain accommodation. Additionally, experiments where nanocrystalline materials were deformed at liquid nitrogen temperatures found a much higher post-deformation dislocation density than in nanomaterials deformed at room temperature [101]. The effect of temperature on the dislocation density implies that a diffusion process is contributing to dislocation elimination. Taken together, these results strongly imply that both dislocation motion and diffusion are important to the deformation of 2-D and 3-D nanomaterials.

Many current models consider the dislocation mechanism to be inoperative [29, 62, 63 93] and consider grain boundary shearing process to be the active source of plastic deformation. Some older models consider dislocation motion as the source of plastic deformation, but almost none of them consider diffusion effects [56, 57]. However, Malygin *et al.* [59] published a model that does consider a combined dislocation and diffusion mechanism. Despite this approach, Malygin assumes a dislocation forest cutting model for grain size strengthening. This is problematic because dislocation forests are notable absent from nanocrystalline metals [37, 43, 46]. Therefore, a new combined dislocation/diffusion model that also takes into account the low density of dislocations observed in nanocrystalline metals deformed ex-situ at room temperature is necessary.

4.2 INVERSE HALL-PETCH MODEL

Dislocations are line defects with length l. From an atomistic point of view, this length becomes increasingly important as the material's grain size reaches the nanoscale. In this model we will first assume that the nature of grain boundaries is not scale dependent. In fact, several investigations have revealed that the structure and width of grain boundaries is essentially the same for nanocrystalline materials and coarser-grained materials [111]. In addition, it will be assumed that any grain boundary exhibits a specific probability to absorb a dislocation, on an atom by atom basis, as the dislocation approaches the grain boundary. However, instead of considering the particular crystallography of a grain boundary, the model proposed herein acknowledges the existence of distinct grain-boundary structures by assuming that each grain boundary exhibits its own specific activation energy for dislocation absorption. This assumption will be discussed later in this chapter in greater detail.

Figures 4.1 and 4.2 schematically illustrate the mechanism considered. Figure 4.1 shows the dislocation approaching a grain boundary and Figure 4.2 show the uncorrelated dislocation atom jumps into the grain boundary that leads to dislocation absorption. The proposed mechanism has all of the features required for a physical explanation of the IHPE in particular, the dislocation motion seen in *in-situ* TEM experiments [23, 24, 26, 74, 103] and the fact that retained dislocation density is temperature dependent.

On the basis of Figures 4.1 and 4.2, let us assume that the probability of a dislocation being absorbed by the grain boundary is P_{dis} and the probability of an individual atom from the dislocation half plane making the jump is P_{atom}. In this fashion, a relatively simple analysis using a Bernoulli distribution function can be made. The Bernoulli function is a discrete distribution having two possible outcomes, labeled by n = 0 and n = 1, in which n = 1 (‘‘success’’) occurs with probability p and n = 0 (‘‘failure’’) occurs with probability$(1-p)$, where 0 < p < 1. Thus, p is the probability of an atom successfully jumping into the grain boundary in a single attempt, whereas $(1-p)$ is the probability of an atom failing to make the jump in a single attempt. With this, we can write for P_{dis}, the following expression

$$P_{dis} = P_{atom}^{J} = [1-(1-p)^{N}]^{J} \tag{4.1}$$

where J is the total number of atoms on the dislocation core jumping into the grain boundary. Equation 4.1 assumes that the probability of an atom jumping back into the dislocation after jumping into the dislocation is negligible. A value for J can be determined by multiplying the atomic planar density ρ of the dislocation plane by the length l of the dislocation line and half the height of the grain, as shown by equation 4.2.

$$J = \frac{\rho d^{2}}{2} \tag{4.2}$$

As the length of the dislocation line is proportional to the grain size d, the variable J is thus related to the grain size. N is the number of attempted jumps by dislocation atoms to the grain boundary during an average time $\bar{t}$ between absorption of dislocations. N is defined by the product of the Debye frequency ν and the time$\bar{t}$. Thus, the $(1-p)^{N}$ term in equation 4.1 represents the chance for one atom failing to make the jump after N attempts while the term $1 - (1 - p)^N$ describes the chance of one or more jump attempts succeeding. The probability p is thus a modified Boltzmann factor that represents the chance of an atom's single jump attempt succeeding, when assisted by a shear stress σ. Hence, p is given by

$$p = exp\left[\frac{-(\Delta G + \sigma b^3)}{k_B T}\right] = exp(M) \tag{4.3}$$

where ΔG is the activation energy for atomic migration, b is the Burgers vector, k_B is Boltzmann's constant and T is temperature. M is thus a mobility factor. As we are describing the jump of atoms from the dislocation core to the grain boundary, ΔG is strongly dependent on the specific structure of the grain boundary, thereby implicitly taking into account the crystallographic nature of the grain boundary. Therefore, for a real material, a range of values is expected for ΔG to account for the range of different grain boundary structures that are expected. Considering M, equation 4.1 can be rewritten as

$$P_{dis} = \{1 - [1 - e^M]^N\}^J \tag{4.4}$$

From equation 4.4, immediate physical insight is possible. Because the term in the curly brackets is always less than 1, higher values of J will lower the probability P_{dis} of a dislocation being absorbed by the grain boundary. Hence, the larger the grain size d, the larger the value of J will be, and the lower will be the probability P_{dis}. Physically, the reason for this to occur is that the larger J is the more atoms that must jump into the grain boundary for this dislocation to be absorbed.

On the other hand, the term in the square brackets, which represents the chance of all of an atom's jump attempts failing, is also less than 1. So, as N is increased, the term $[1-p]^N$ decreases and thus the probability P$_{dis}$ increases. The reason for this behavior is due to the fact that N is the number of attempted jumps atoms in the dislocation plane make to the grain boundary during an average time $\bar{t}$ between absorption of dislocations. Hence, as the time $\bar{t}$ increases, N increases and thus the probability P$_{dis}$ of dislocation absorption increases. In other words, this is a question of whether the absorption of dislocations by grain boundaries is fast enough to be relevant at the strain rates the material is subjected to.

Assuming that the strain in the material is accommodated by the motion of dislocations, it is possible to determine the average time $\bar{t}$ that an individual dislocation has to traverse the entire grain in order to match the applied strain rate. The strain associated with the motion of one single dislocation is given by the Burgers vector times the Schmid factor over the grain size. Hence, the N factor can be rewritten as

$$N = t\nu_{Debye} = \frac{\varepsilon_{dis}}{\dot{\varepsilon}}\nu_{Debye} = \frac{b\nu C_{\phi}}{\dot{\varepsilon}d} \tag{4.5}$$

where the symbols have the same meaning as before. As a result, equation 4.4 shows that the probability of dislocation absorption by grain boundaries is strongly dependent on the grain size d and the strain rate$\dot{\varepsilon}$. As the absorption of dislocations by grain boundaries will obviously interfere with grain-boundary strengthening, equation 4.4 predicts that the greater the grain-boundary absorption that can occur, the more deviation from the Hall–Petch behavior (Eq. 2.1) should be expected.

It is now possible to substitute equations 4.2, 4.3 and 4.4 into equation 4.1 to define P_{dis}, as

$$P_{dis} = \left\{ 1 - \left[1 - e^{-\frac{E_i + \sigma b^3}{k_2 T}} \right]^{\frac{b C_\phi v_{Debye}}{\dot{\varepsilon} d}} \right\}^{\rho d^2} \tag{4.6}$$

At this point, the task of establishing a correlation between the probability of dislocations being absorbed by grain boundaries and the classical Hall–Petch equation remains. To start, consider that the leading dislocation in a pile-up of n dislocations experiences a force due to (i) the resolved shear stress, τ, (ii) the other (n-1) dislocations and (iii) a backward force due to the internal stress τ_0 produced by the grain boundary. According to the classical formulation of the Hall–Petch equation, the internal stress τ_0 is considered from the point of view of a rigid grain boundary, where dislocations pile up. This is the case where $P_{dis} = 0$ in equation 4.4. But, what happens when $P_{dis} \neq 0$? In this case, the grain boundary is no longer a rigid barrier and thus the internal stress τ_0 should be reduced to a term τ_0 $(1-P_{dis})$. Assuming that the leading dislocation moves forward towards the grain boundary by a distance δx, the work done by the resolved shear stress can be described by $W_1 = nb\tau\delta x$. Therefore, the motion of the leading dislocation results in an increased interaction with the grain boundary, which can be described by $W_2 = b\tau_0 (1-P_{dis})\delta x$. At equilibrium, $W_1 = W_2$ and, hence, the resolved shear stress acting on the leading dislocation of a pile-up composed of n dislocations equals the backward force due to the internal stress τ_0 produced by the grain boundary. This can be expressed by

$$\tau_0 = \tau_1 = \frac{n\tau}{(1 - P_{dis})} \tag{4.7}$$

where the symbols have the same meaning as before. Assuming $\eta = d\tau/\mu b$ [27, 28], where d is the grain size, τ is the resolved shear stress, μ is the shear modulus and b is the Burgers vector, equation 4.7 can be rewritten as

$$\tau^2 = \frac{\tau_1 \mu b (1 - P_{dis})}{d} \tag{4.8}$$

Considering the Schmid factor $C_{□} = \cos\theta\cos□$, then $\tau = \sigma\cos\theta\cos□$ and $\tau_1 = \theta_1\cos\theta\cos□$, where σ is the applied stress, σ_1 is the critical stress at the leading dislocation to activate a dislocation source on an adjacent grain, θ is the angle between the tensile axis and the normal to the slip plane and □ is the angle between the tensile axis and the slip direction, equation 4.8 assumes the form

$$\sigma = \left[\frac{\sigma_1 \mu b}{cos\theta cos\phi}\right]^{\frac{1}{2}} \left[\frac{1 - P_{dis}}{d}\right]^{\frac{1}{2}} \tag{4.9}$$

Assuming $k = \left[\frac{\sigma_1 \mu b}{cos\theta cos\phi}\right]^{\frac{1}{2}}$, equation 4.9 becomes

$$\sigma = k\left[\frac{1 - P_{dis}}{d}\right]^{\frac{1}{2}} \tag{4.10}$$

which represents the yield strength of a material as a function of grain size and dislocation absorption by grain boundaries, when the lattice friction stress $\sigma_0 = 0$. In the presence of a lattice friction stress, the modified Hall–Petch relation can be expressed as

$$\sigma_y = \sigma_0 + k\left[\frac{1 - P_{dis}}{d}\right]^{\frac{1}{2}} \tag{4.11}$$

This equation describes the yield stress of a material as a function of grain size, taking into account the probability of grain-boundary absorption. Equation 4.11 reverts to the classical Hall–Petch equation when the boundary is rigid and $P_{dis} = 0$. The essential effect of grain-boundary dislocation absorption is to reduce the number of dislocations, n, in the pile-up, which decreases the stress at the leading dislocation. If all moving dislocations are absorbed by the existing grain boundaries ($P_{dis} = 1$), then equation 4.11 is reduced to $\sigma_y = \sigma_0$, i.e., grain boundaries do not play any role in strengthening the material. In addition, as the term P_{dis} is negative in equation 4.11, reducing the Hall–Petch coefficient, k, is simply an inversion of the Hall–Petch relation.

4.3 DISCUSSION

Equation 4.11 can be evaluated for any material at a given temperature and strain rate. For illustration purposes, the case of Ni deformed at room temperature under a strain rate of 10^{-5} s^{-1} is considered. To determine P_{dis}, the resolved shear stress, τ, acting on the dislocations was assumed to be $\tau \approx \tau_0 C_{\square}$ and τ_0 = 21.8 MPa [112]. For the Schmid factor $C_{\square}$, it is assumed that (i) a random orientation of grains with respect to the applied stress axis and (ii) a maximum stress direction on the slip plane. For an FCC material, the maximum angle possible between {111} slip planes is 109.48°, thus giving the average value

$$C_{\phi} \approx \int_{0}^{109/2} cos(\theta) sin(\theta) d\theta = 0.33 \tag{4.12}$$

In addition, the following values were considered, namely b = a/2[110] = 0.258 nm, where a = 0.365 nm is the lattice parameter for Ni, $\nu = 10^{13}$ Hz and ρ = 6.54 atoms/nm for the linear atomic density of the dislocation line in Ni. Finally, ΔG in Eq. 4.3 was assumed to be the activation energy for grain-boundary self-diffusion. This is a reasonable assumption as the absorption of atoms from the dislocation core into a grain boundary is what is considered. For FCC metals, ΔG has been reported to vary within the range 0.6–1.5 eV [113] and thus a variety of activation energies were considered. One other reason to consider a variation in the activation energies is that grain boundaries with specific crystallographic structures will exhibit distinct abilities to absorb dislocations.

Finally, assuming k = 0.158 MPa $m^{1/2}$ for the case of Ni [114], the yield stress σ_y in Eq. 4.9 can be plotted as a function of grain size for various activation energies (Fig. 4.4).

As shown in Fig. 4.4, for specific activation energies, there is a sharp transition at a critical grain size at which the slope of the yield stress vs. $d^{-1/2}$ curve inverts. The critical yield stress (CYS) at which the transition occurs represents the onset of the inverse Hall–Petch behavior. At the highest activation energy examined (1 eV); the inverse Hall–Petch behavior is not expected for Ni, even at unrealistically small grain sizes. On the other hand, for sufficiently small activation energies (0.75 eV), dislocation absorption in Ni is expected to dominate. It is important to note that Figure 4.4 assumes that the entire material is characterized by a single value of ΔG. In a real material, a distribution of ΔG values is expected. This would cause the transition to IHPE behavior to be less sharp.

Equation 4.11 was also evaluated for different strain rates (Figure 4.5). Higher strain rates result in less deviation from the classical Hall–Petch relation, which results in higher CYS. Thus, higher strain rates and higher activation energies have a similar effect on the Hall–Petch behavior. Finally, calculations of equation 4.11 for different temperatures (Figure 4.6), predict that the CYS will be lower for higher temperatures and quite sensitive to temperature changes. Thus, changes in temperature will have the opposite effect on the CYS to changes in activation energy and strain rate.

These predictions are theoretically and experimentally important for several reasons. First, the activation energy, which is typically proportional to the melting temperature, is expected to be different for distinct materials. In fact, calculations of Eq. 4.11 for Al, Cu and Ni reveal that a deviation from the Hall–Petch equation occurs earlier (coarser grain sizes) for Al, followed by Cu and Ni. Moreover, since the activation energy is correlated with grain-boundary structure, knowledge of the grain-boundary distribution becomes important to full understanding of the Hall–Petch behavior. Table 4.1 lists several different FCC metals, their melting points, their activation energies of grain boundary self diffusion, and whether the model predicts the IHPE for them at room temperature. The IHPE is predicted for all the FCC materials considered besides Ni.

The model's second prediction is that the CYS depends significantly on strain rate, which confirms previous research [114-119]. This result is not surprising. As the strain rate is increased, more dislocations impinge on the grain boundaries per unit time. Therefore, less time is available for dislocations to be absorbed, leading to higher CYS at faster strain rates.

The third important prediction is that the CYS is very sensitive to temperature changes. As the temperature is increased, the probability for dislocation absorption increases, leading to stronger deviations from the Hall–Petch relation. Although work on the effect of temperature on the yield strength of nanocrystalline materials is sparse [114, 116], the model suggests that experiments of this nature could help us understand the mechanisms of deformation in nanocrystalline materials.

In order to properly to consider and confirm the results of the model, it is important to evaluate how the model fits the experimental data available in the literature. In doing so, a few issues arise. First, as tensile tests in nanocrystalline materials are difficult to perform, strain rates are frequently not recorded. This is problematic, as the strain rate is a very important parameter in the model described herein, while fitting the experimental data becomes very difficult if it is unknown.

Second, the model assumes discrete values for the activation energy (grain-boundary self-diffusion) and for the grain size of the material. Yet, in real polycrystalline materials, a spread in activation energies (dictated by a distribution in grain-boundary structures) and a spread in available grain sizes is expected. Quantifying the effects of this spreading effect is not trivial and should be examined in future work.

Third, the published data lack agreement due to the wide variety of experimental conditions employed, namely the use of different nanocrystalline materials, distinct methods of preparation (electrodeposited, severely deformed, powder compacted) and the use of either tensile tests under various strain rates and/or hardness tests.

An example of the variation in the Hall–Petch results for Ni using both tensile and hardness data is shown in Fig. 4.7. Although several studies claim evidence that either supports the classical [48,49, 54] or the inverse Hall–Petch behavior [29, 51 52, 69], when the data for nanocrystalline Ni are viewed as a whole it becomes unclear whether it exhibits the IHPE.

According to our model, a lack of inverse Hall–Petch behavior in Ni would not be surprising. In fact, due to the high melting temperature of Ni and consequent high activation energy, we could expect it effectively to halt grain-boundary absorption of dislocations at reasonable strain rates. However, as mentioned above, polycrystalline materials exhibit a distribution of grain sizes and grain boundary structures, which may lead to some form of deviation from the classical Hall–Petch relationship.

The model also suggests that the variation of results, such as those in Fig. 4.7, may differ due to differences in experimental conditions. If the strain rates used in the experiments differed significantly, or different methods for producing nanocrystalline materials lead to dissimilar grain-boundary distributions and grain size distributions, this in turn could result in distinct abilities for absorbing dislocations.

In the context of this discussion, it is valuable to consider the expected behavior of nanocrystalline copper, which has been widely investigated in the open literature [29-35, 38, 39, 41,44, 47, 99], According to the model outlined above, copper would be more likely to exhibit an inverse Hall–Petch effect and/or exhibit a lower CYS than nickel. This is because the activation energy for dislocation absorption by grain boundaries for copper is lower than that of nickel. However, upon examination of the experimental results obtained for nanocrystalline copper (Fig. 4.8); the results reported are even more difficult to interpret than the results for nickel. As shown in Fig. 4.8, the two sets of data reported by Sanders *et al*. [8] appear to support the IHPE for a critical grain size of ~16 nm. On the other hand, the remainder of the data combined is highly inconclusive.

There are several possible explanations for this. It is possible that the samples indicating an IHPE were flawed in some way, for instance incomplete densification or the presence of an additional amorphous phase. It is also possible that, due to differences in the microstructure, some of the materials exhibited IHPE behavior while others did not. The theory presented above can rationalize this anomaly if the samples can be shown as having grain boundaries with substantially different activation energies of absorption.

Overall, the data obtained from individual research groups and shown in Fig. 4.8 seem to support the IHPE. However, when the data from single research groups are combined and viewed as a whole, the result is still ambiguous.

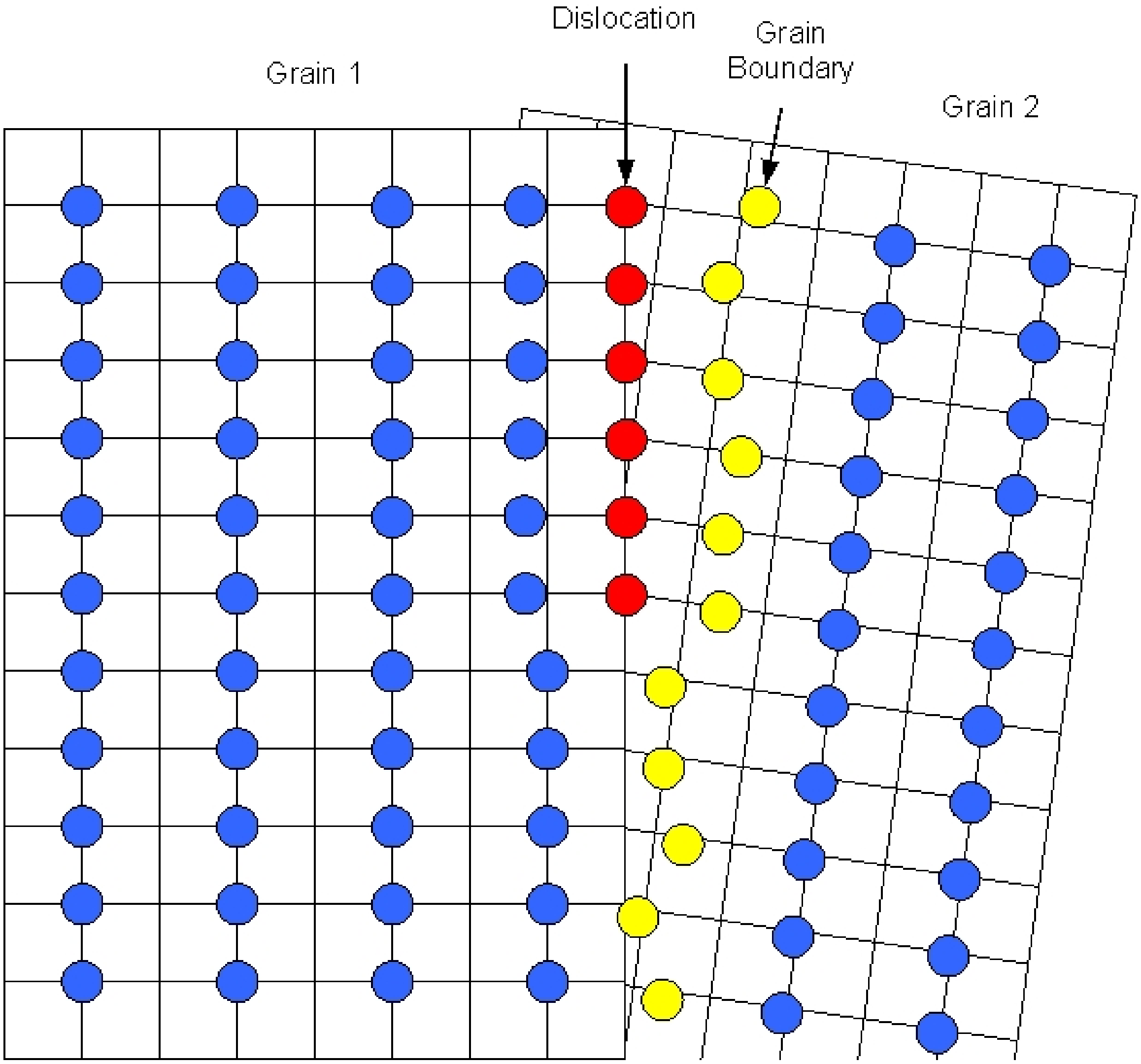

Figure 4.1: A schematic diagram of a single edge dislocation approaching a grain boundary. Notice that the dislocation half plane has a certain height.

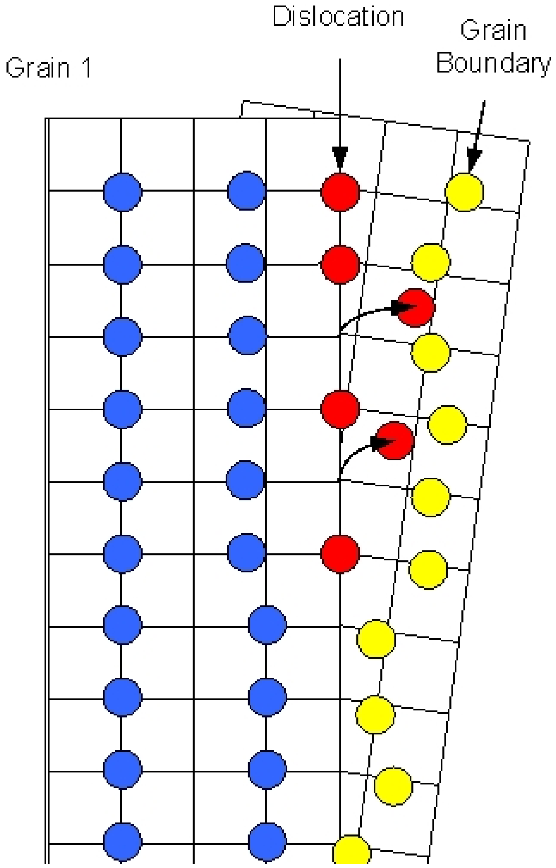

Figure 4.2: A schematic diagram of the uncorrelated atomic jumps of dislocation atoms into the grain boundary.

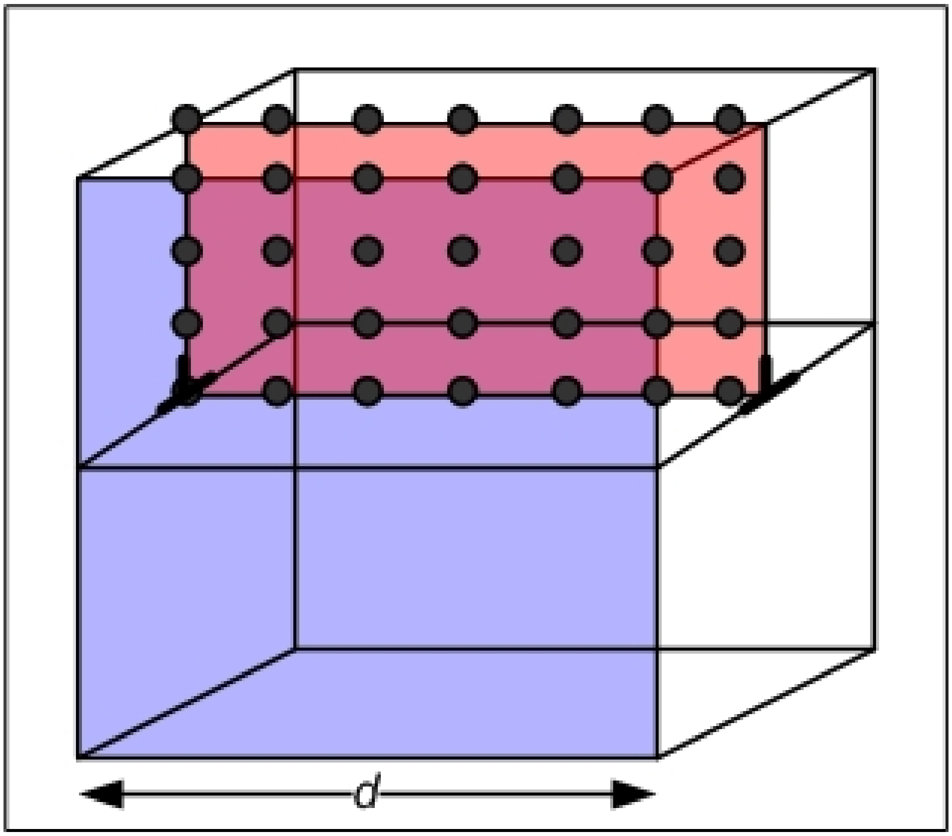

Figure 4.3: A schematic diagram of the geometry considered for the IHPE model. Notice that the number of atoms in the dislocation depends on the grains size.

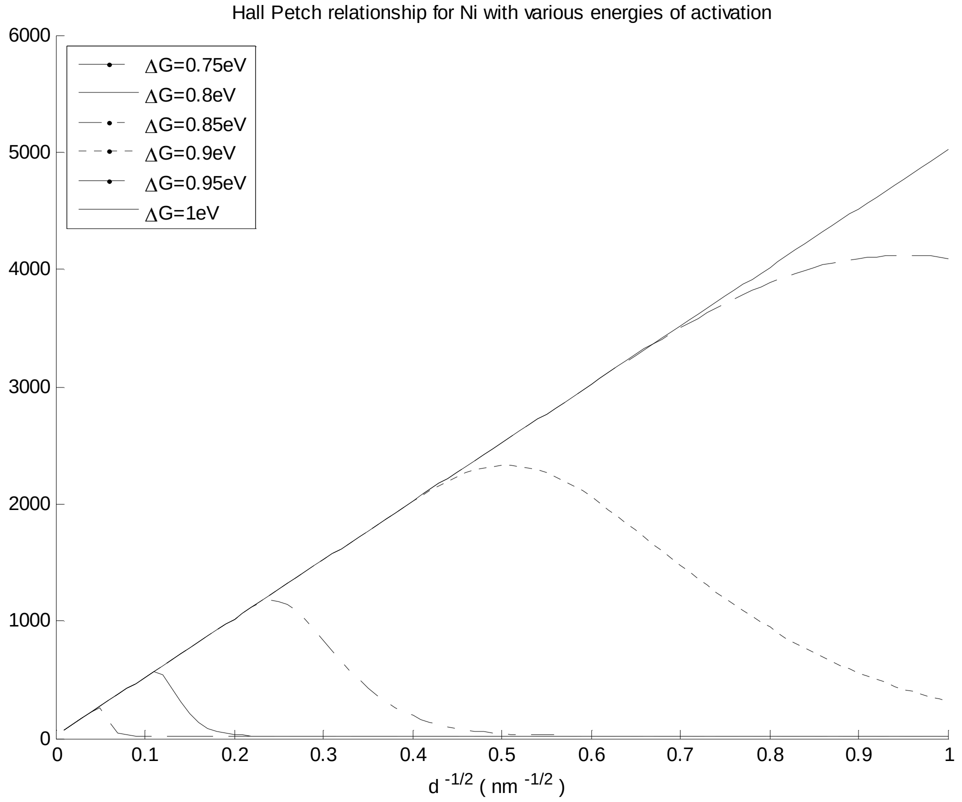

Figure 4.4: A plot of Yield stress vs. d$^{-1/2}$ for Ni, using various activation energies for an atom jumping into the grain boundary. For Nickel, the real value for this activation energy is close to 1eV.

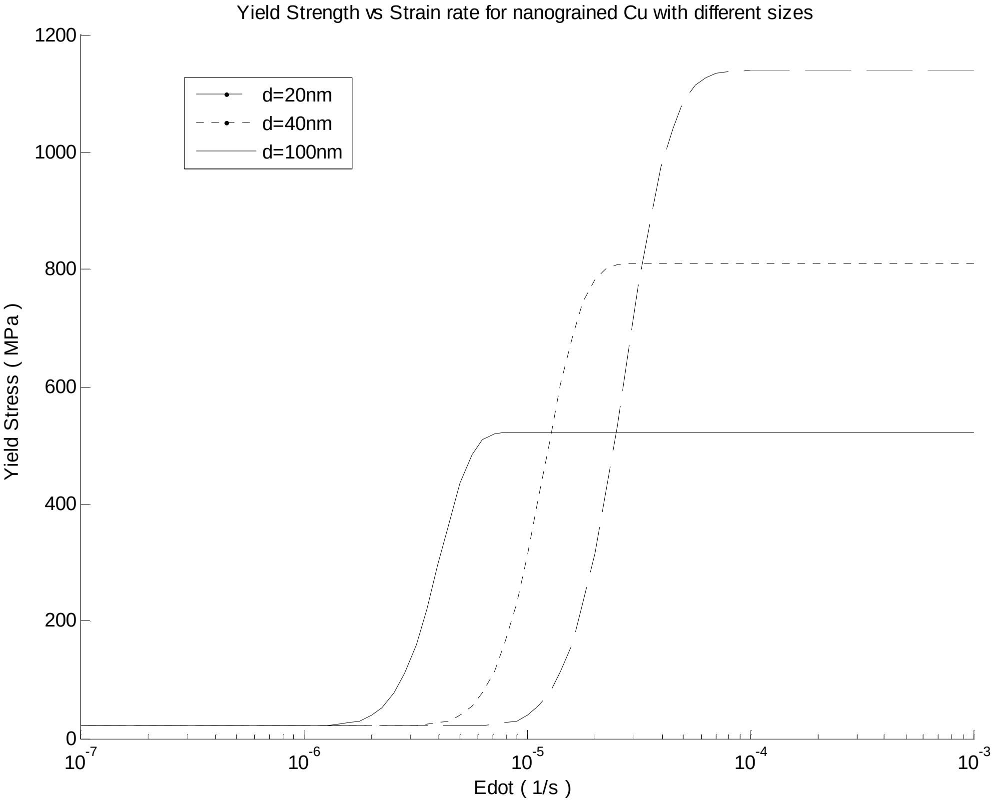

Figure 4.5: Yield stress vs. strain rate for materials with different nanocrystalline grain sizes. The increase in yield stress is due to the re-activation of the normal Hall-Petch effect due to decreasing times allowed for dislocation absorption.

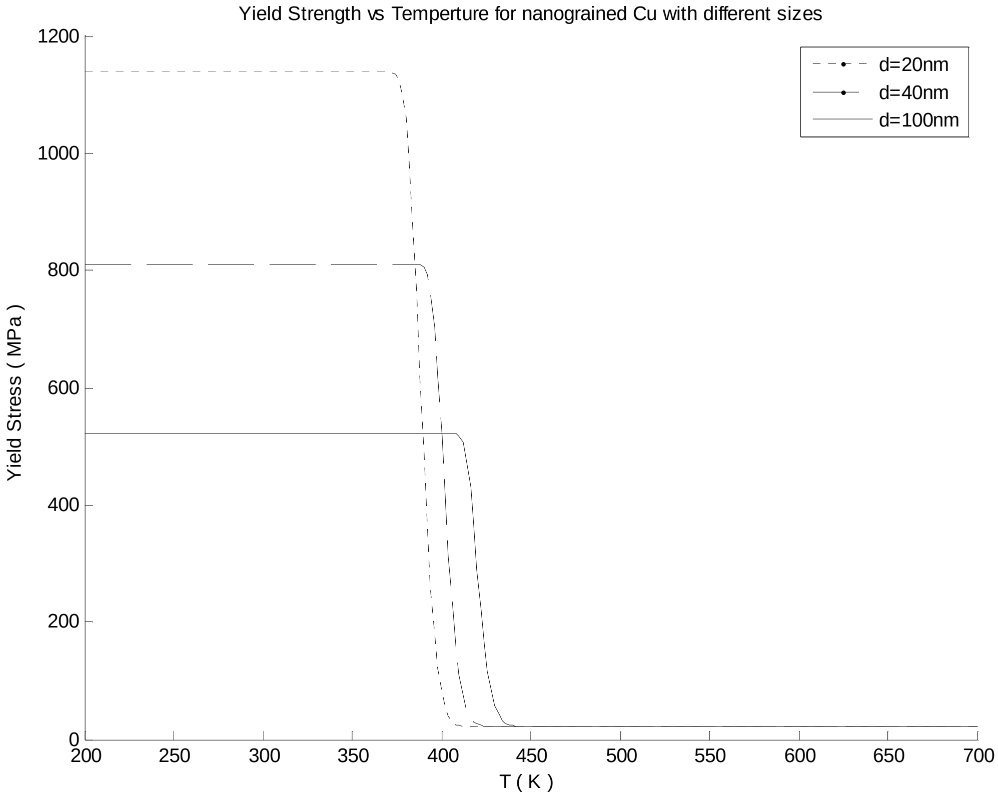

Figure 4.6: Yield stress versus temperature for several different grain sizes. The rapid reduction of strength is caused by the activation of the IHPE due to increasing atomic mobility.

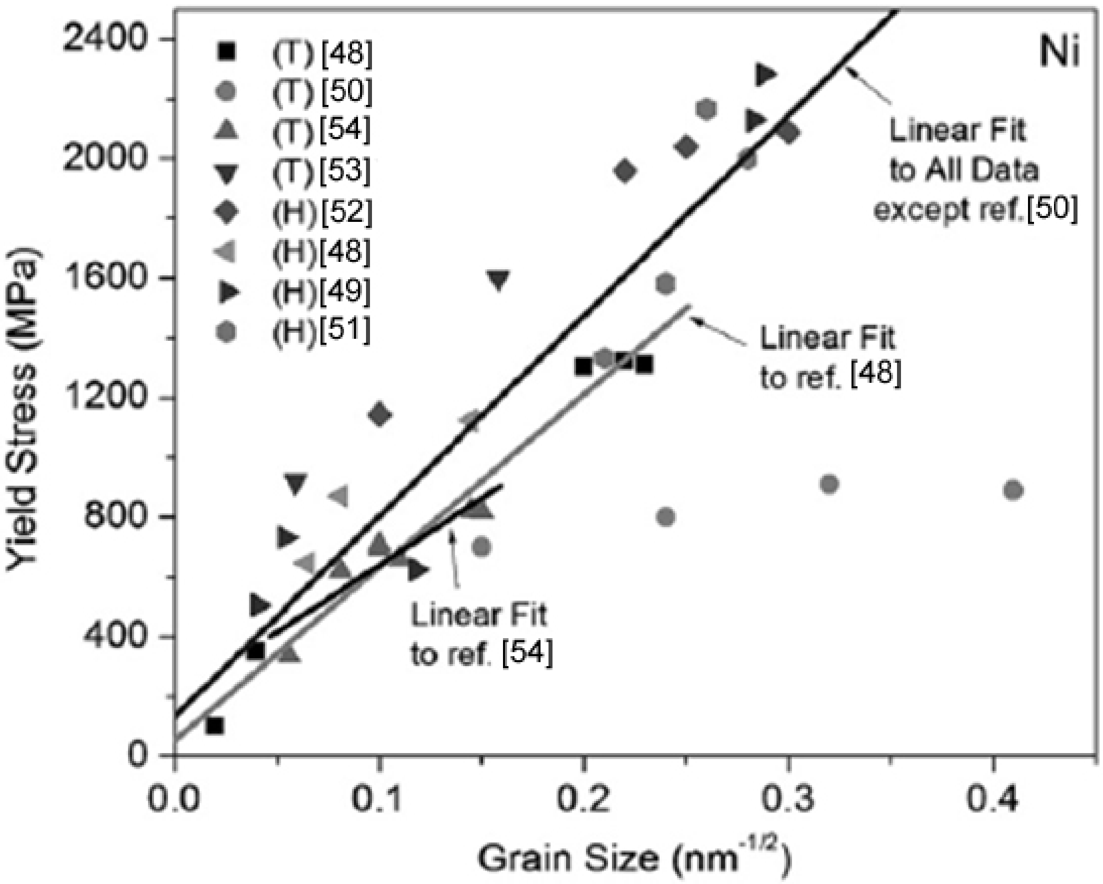

Figure 4.7: A plot of the reported yield strength vs grain size for Ni. The data points are from the literature. Notice how well straight lines fit the data, implying absence of the IHPE.

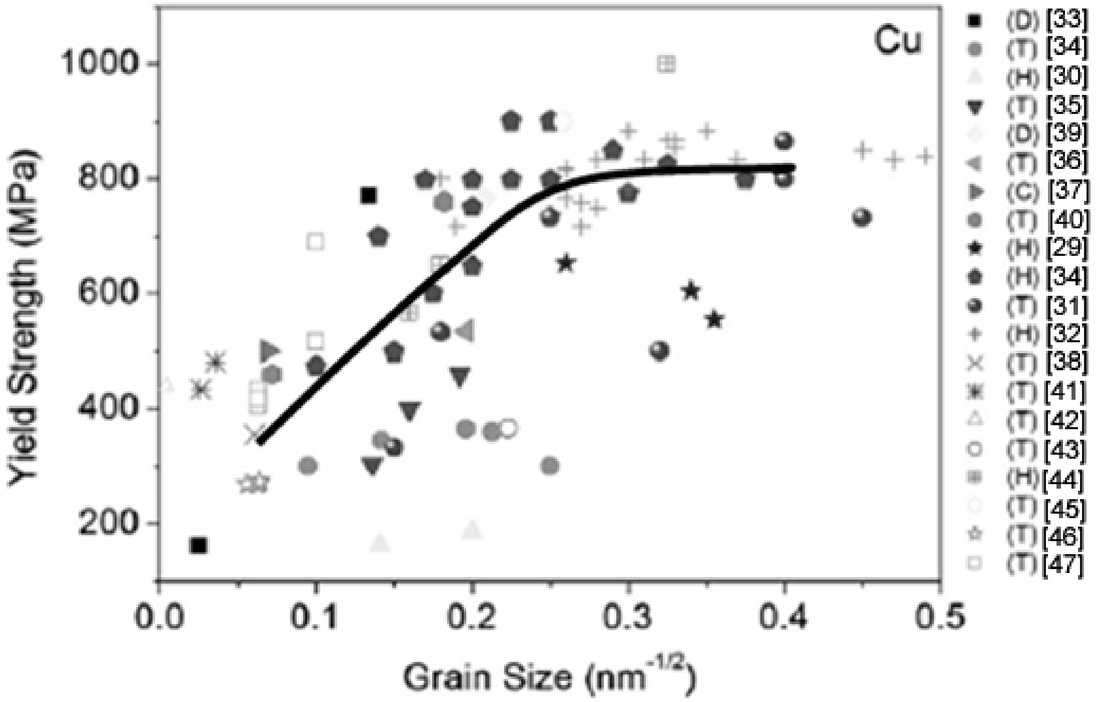

Figure 4.8: A plot of the reported yield strength vs grain size for Cu. The data points are from the literature. The curve was drawn free-hand, and implies the presence of the IHPE.

Table 4.1: Melting temperature, activation energy for self diffusion and prediction of IHPE behavior for several metals at room temperature and reasonable strain rates.

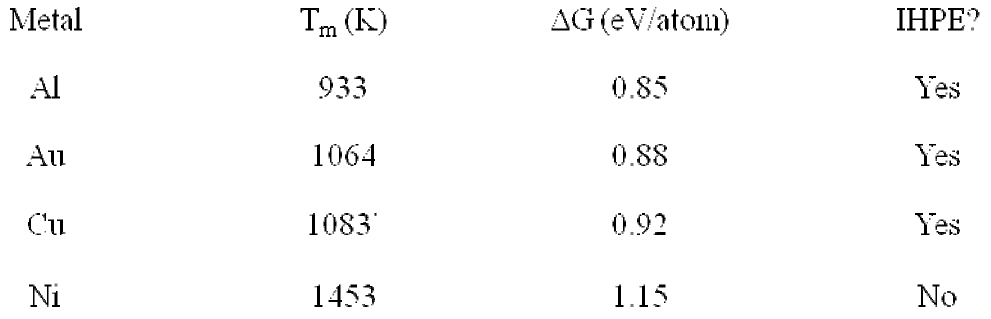

Metal	T_m (K)	ΔG (eV/atom)	IHPE?
Al	933	0.85	Yes
Au	1064	0.88	Yes
Cu	1083	0.92	Yes
Ni	1453	1.15	No

CHAPTER 5: CONCLUSIONS AND FUTURE WORK

5.1 CONCLUSIONS

This dissertation studied the deformation in defect behavior of 0-D to 3-D nanomaterials using theoretical modeling and *in-situ* TEM nanocompression experiments. From this work, the following conclusions can be made.

1. In 0-D and 1-D nanomaterials, dislocations can exist, but they are unstable. The theoretical model developed in this dissertation show that a dislocation may nucleate heterogeneously at the nanoparticle's surface under reasonable applied stresses. However, upon dislocation nucleation, the presence of the nearby surfaces subject the dislocation to spontaneous stresses, which tend to eject the dislocation toward the free surfaces. This mechanism was observed in all the various nanocompression experiments performed in this dissertation.

2. Twins are observed in nanoparticles even when the material has a high SFE because Shockley partial dislocations are energetically more stable at the nanoscale. This is confirmed by the Gibbs free energies for nucleation of perfect or partial dislocations in Cu and Al nanomaterials. In particular, the Gibbs free energy of formation for partial dislocations rapidly decreases as the size of the nanoparticle is reduced, especially in high SFE materials, such as Al. This indicates a strong size effect on the stabilization of twins.

3. The inverse Hall-Petch effect is caused by a high probability for dislocation absorption by the grain boundaries, as crystal size is reduced. This is supported by the theoretical model developed in this dissertation and a further comparison of the model with the experimental data from literature. The dislocation absorption model predicts also strong strain rate and temperature dependence for the inverse Hall-Petch effect.

5.2 FUTURE WORK

Considering the results of this dissertation, the following experiments would further increase the understanding of deformation and defects of nanomaterials: 1) development of a computational model to assess the formation bend contours in Hertzian contact, 2) *In-situ* TEM nanoindentation experiment on 1-D nanomaterials, 3) further simplification of the IHPE model presented Chapter 3, and 4) IHPE testing as a function of strain rate and temperature.

Regarding the formation of bend contours in nanocompression, a computational finite element model evaluating the rotations of the lattice planes during Hertzian contact should be made. It is possible that these rotations could cause bend contours, but the problem is extremely difficult to solve analytically. An understanding of how much stress and stain would be required to activate this contrast mechanism would be very useful.

It is also critical to understand the link between deformation in 0-D and 1-D nanomaterials. Specifically, 1-D nanomaterials with diameters below 100nm must be tested by *in-situ* TEM. This is a very difficult experiment because of a multitude of specimen-probe alignment issues, and sample fabrication issues. This proposed experiment could show the origins of dislocations in 1-D nanomaterials and help us understand when Frank-Read sources cease operating.

In addition, a simplification of the equation for P_{dis} would be an excellent area for future work. It is possible to use algebraic substitution to simplify the equation for P_{dis} by replacing binomial distributions with Poison distributions, along with some other algebraic manipulations. This could make the formulas for the yield stress easier to use, and therefore more useful.

Additionally, experimental work could be done to analyze the IHPE as a function of strain rate and temperature. Very little work has been done in this area, and understanding how the IHPE behavior is affected by changes in temperature and strain rate is absolutely vital to obtaining a deeper understanding of the mechanisms that cause the IHPE. Even nanoindentation tests on nanocrystalline materials at different temperatures could help us learn much more about the IHPE.

REFERENCES

1. Gryaznov VG, Polonsky IA, Romanov AE, Trusov LI, “ Size effects of dislocation stability in nanocrystals,” Physical Review B, 1991;44:42

2. Wu Y, Takeguchi M, Chen Q, Furuya K,” Defects and their movement in Pb and Ge nanocrystal characterized by ultra-high vacuum high resolution transmission electron microscope,” Applied Surface Science, 2000;159-156:p486

3. M. Rose, A. Balogh and H. Hahn, Mat. Sci. Forum. 1997; 248-249: 213

4. N. Nita, R. Schaeublin, M. Victoria, J. Nucl. Mater. 2001;329:953-957

5. Y. Chimi, A. Iwase, N. Isikawa, M. Kobiyama, T. Inami, S. Okuda, J Nucl. Mat. 2001; 297:355

6. Ben-David, T. *et al*. Correlated Orientations in Nanocrystal Fluctuations. *Phys. Rev. Lett.* 1997;78: 2585

7. Chen Mw, Ma E, Hemker KJ, Shen H, Wang Y, Cheng X, Science 2003;300(5623):1275-7

8. Liao XZ, Zhao YH, Srinivasan SG, Zhu YT, *et al.* Applied Physics Letters 2004;84(4):592-4

9. Zhu YT, Liao XZ, Srinivasan SG, Zhao YH, Baskes MI, Zhou F, *et al.*, Applied Physics Letters, 2004:85(21):5049

10. J. Deenan, WM Mook, A Minor, WW Gerberich, CB Carter, *In-situ* deformation of Si nanospheres, J Mater Sci, 2006;41:4477

11. M.D. Uchic, D. M. Dimiduk, J. N. Florando, W.D. Nix, "Sample Dimensions Influence Strength and Crystal Plasticity," Science, 2004;305:986

12. D.M. Dimiduk, M.D. Uchic, T.A. Parthasarathy, "Size affected single-slip behavior of pure nickel microcrystals ," Acta Materialia, 2005:53;4065,

13. B.E Schuster, Q. Wei, H. Zhang, K.T. Ramesh, "Microcompression of nanocrystalline Nickel," Applied Physics Letters, 2006:88;103112

14. C.A Volkert, E.T. Lilleodden, "Size effects in the deformation of sub-micron Au columns," Philosophical Magazine, 2006;86:5567

15. H Bei, S Shim, EP George, MK Miller, EG Herbert, GM Pharr, "Compressive strength of molybdenum alloy micropillars prepared using a new technique," Scripta Materialia, 2007;57:397

16. V.S. Deshpande, A. Needleman, E. van der Giessen, “Plasticity size effects in tension and compression of single crystals,” Journal of the Mechanics and Physics of Solids, 2005;53;2661

17. T.A. Parathasarathy, S.I. Rao, D.M. Dimiduk, M.D. Uchic, D.R. Trinkle, “Contribution to size effect of yield strength from the stochastics of dislocation source lengths in finite samples,” Scripta Materialia, 2006;56:313

18. T. Ohashi, M. Kawamukai, H. Zbib, “A multiscale approach for modeling scale-dependent yield stress in polycrystalline metals,” International Journal of Plasticity, 2007;23:897

19. Y. Guo, Z. Zhuang, X.Y. Li, Z. Chen, “An investigation of the combined size and rate effects on mechanical responses of FCC metals,” International Journal of Solids and Structures, 2007;44:1180,

20. Milligan WW, Hackne SA, Ke M, Aifantis EC. *In-situ* studies of deformation and fracture in nanophase materials. Nanostruct Mater 1993;2:267–76.

21. Kumar KS, Suresh S, Chisholm MF, Horton JA, Wang P. Deformation of electrodeposited nanocrystalline nickel. Acta Mater 2003;51:397–405.

22. Shan Zhiwei, Stach EA, Wiezorek JMK, Knapp JA, Follstaedt DM, Mao SX. Grain boundary mediated plasticity in nanocrystalline nickel. Science 2004;305:654–7.

23. Hattar K, Han J, Saif MTA, Robertson IM. *In-situ* transmission electron microscopy observations of toughening mechanisms in ultrafine grained columnar aluminum thin films. J Mater Res 2005;20:1869–77.

24. Hugo RC, Kung HH, Weertman JR, Mitra R, Knapp JA, Follstaedt DM. *In-situ* TEM tensile testing of DC magnetron sputtered and pulsed laser deposited Ni thin films. Acta Mater 2003;51:1937.

25. Haque MA, Saif MTA. *In-situ* tensile testing of nanoscale freestanding thin films inside a transmission electron microscope. J Mater Res 2005;20:1769–77.

26. Youngdahl CJ, Weertman JR, Hugo RC, Kung HH. Deformation behaviour in nanocrystalline copper. Scr Mater 2001;44:475–1478.

27. Hall EO. The deformation and aging of mild steel. Proc Phys Soc London B 1951;64:747.

28. Petch NJ. The cleavage strength of polycrystals. J Iron Steel Inst 1953;25:174.

29. Chokshi AH, Rosen A, Karch J, Gleiter H. On the validity of the Hall–Petch relationship in nanocrystalline materials'. Scr Metall 1989;23:1679.

30. Nieman GW, Weertman JR, Siegel RW. Microhardness of nanocrystalline palladium and copper produced by inert-gas condensation. Scr Metall 1989;23:2013.

31. Nieman GW, Weertman JR, Siegel RW. Mechanical behavior of nanocrystalline Cu and Pd. J Mater Res 1991;6:1012.

32. Fougere GE, Weertman JR, Siegel RW, Kim S. Grain-size dependent hardening and softening of nanocrystalline Cu and Pd. Scr Metall Mater 1992;26:1879.

33. Gertsman VY, Hoffmann M, Gleiter H, Dirringer R. Grain size dependence of yield of copper. Acta Mater 1994;42:3539.

34. Sanders PG, Eastman JA, Weertman JR. Elastic and tensile behavior of nanocrystalline copper and palladium. Acta Mater 1997;10:4019

35. Iyer SR, Frey CA, Sastry SML, Waller BE, Buhro WE. Mater Sci Eng A 1999;264:210.

36. Youssef KM, Scattergood R, Murty KL, Koch CC. Ultratough nanocrystalline copper with a narrow size distribution. Appl Phys Lett 2004;85:929.

37. Legros M, Elliot BR, Rittner MN, Weertman JR, Hemker KJ. Microsample tensile testing of nanocrystalline metals. Philos Mag A 2000;80:1017.

38. Huang HB, Spaepen F. Tensile testing of free-standing Cu, Ag and Al thin films and Ag/Cu multilayers. Acta Mater 2000;48:3261.

39. Valiev Z, Kozolv E, Ivanov YF, Lian J, Nazarov AA, Baudelet R. Deformation behavior of ultra-fine-grained copper. Acta Mater 1994;42:2467.

40. Wang YM, Wang K, Pan D, Lu K, Hemker KJ, Ma E. Microsample tensile testing of nanocrystalline copper. Scr Mater 2003;48:1581.

41. Merz MD, Dahlgren SD. Tensile-strength and work-hardening of ultrafine-grained high-purity copper. J Appl Phys 1975;46:3235

42. Embury DJ, Lahaie JD. In: Natasi M *et al.*, editors. Mechanical properties and deformation behavior of materials having ultrafine microstructure. Dordrecht: Kluwer; 1993.

43. Lu L, Sui ML, Lu K. Superplastic extensibility of nanocrystalline copper at room temperature. Science 2000;287:1463.

44. Chen J, Lu L, Lu K. Hardness and strain rate sensitivity of nanocrystalline Cu. Scr Mater 2006;54:1913.

45. Lu L, Shen Y, Chen X, Qian L, Lu K. Ultrahigh strength and high electrical conductivity in copper. Science 2004;304:422.

46. Ebrahimi F, Zhai Q, Kong D. Deformation and fracture of electrodeposited copper. Scr Mater 1998;39:315.

47. Haouaoui M, Karaman I, Maier HJ, Hartwig KT. Microstructure evolution and mechanical behavior of bulk copper obtained byconsolidation of micro- and nanopowders using equal-channel angular extrusion. Metall Mater Trans A 2004;35:2935

48. Xiao C, Mirshams RA, Whang SH, Yin WM. Tensile behavior and fracture in nickel and carbon doped nanocrystalline nickel. Mater Sci Eng A 2001;301:35.

49. Hughes GD, Smith SD, Pande CS, Johnson HR, Armstrong RW. Hall–Petch strengthening for the microhardness of twelve nanometer grain diameter electrodeposited nickel. Scr Metall 1986;20:93.

50. Wang N, Wang Z, Aust KT, Erb U. Room temperature creep behavior of nanocrystalline nickel produced by an electrodeposition technique. Mater Sci Eng A 1997;237:150.

51. Schuh CA, Nieh TG, Yamasaki T. Hall–Petch breakdown manifested in abrasive wear resistance of nanocrystalline nickel. Scr Mater 2002;46:735.

52. El-Sherik AM, Erb U, Palumbo G, Aust KT. Deviations from Hall–Petch behavior in as-prepared nanocrystalline nickel. Scr Mater 1992;27:1185.

53. Schwaiger R, Moser B, Dao M, Chollacoop N, Suresh S. Some critical experiments on the strain-rate sensitivity of nanocrystalline nickel. Acta Mater 2003;51:5159.

54. Ebrahimi F, Bourne GR, Kelly MS, Matthews TE. Mechanical properties of nanocrystalline nickel produced by electrodeposition. Nanostruct Mater 1999;11:343

55. Giga A, Kimoto Y, Takigawa Y, Higashi K. Demonstration of an inverse Hall–Petch relationship in electrodeposited nanocrystalline Ni–W alloys through tensile testing. Scr Mater 2006;55:143.

56. Nieh TG, Wadsworth J. Hall–Petch relation in nanocrystalline Solids. Scr Metall Mater 1991;25:955.

57. Scattergood RO, Koch CC. A modified-model for Hall–Petch behavior in nanocrystalline materials. Scr Metall Mater 1992;27: 1195.

58. Lian B Buadelet, Nazarov A. Model for the prediction of the mechanical behavior of nanocrystalline materials. Mater Sci Eng A 1993;172:23.

59. Malygin GA. Breakdown of the Hall–Petch law in micro- and nanocrystalline metals. Phys Solid State 1995;37:1248.

60. Yamakov V, Wolf D, Phillpot SR, Muckherjee AK. Dislocation processes in the deformation of nanocrystalline aluminium by molecular-dynamics simulation. Nat Mater 2002;1:1.

61. Schiotz J, Jacobsen K. A maximum strength of nanocrystalline copper. Science 2003;301:1357.

62. Masamura RA, Hazzledine PM, Liaw PK, Lavernia EJ. Yield stress of fine grained materials. Acta Metall 1998;13:4527.

63. Conrad H, Narayan J. On the grain size softening in nanocrystalline materials. Scr Mater 2000;42:1025.

64. Van Swygenhoven H, Spaczer M, Caro A. Microscopic description of plasticity in computer generated metallic nanophase samples: a comparison between Cu and Ni. Acta Mater 1999;47:3117.

65. Takeuchi S. The mechanism of the inverse Hall–Petch relation in nanocrystals. Scr Mater 2001;44:1483.

66. Yamakov V, Wolf D, Salazar M, Phillpot SR, Gleiter H. Deformation mechanism crossover and mechanical behavior in nanocrystalline materials. Philos Mag Lett 2003;83:385.

67. Yamakov V, Wolf D, Phillpot SR, Mukherjee AK, Gleiter H. Deformation-mechanism map for nanocrystalline metals by molecular dynamics simulation. Nat Mater 2004;3:43.

68. Lu K, Sui ML. An explanation of the Hall–Petch law in micro and nanocrystalline materials. Scr Mater 1993;28:1465.

69. Wang Ning, Wang Zhirui, Aust T, Erb U. Effect of grain size on the mechanical properties of nanocrystalline materials. Acta Metall Mater 1995;43:519–23.

70. Konstantinidis DA, Aifantis EC. On the anomalous hardness of nanocrystalline materials. Nanostruct Mater 1998;10:1111.

71. Song HW, Guo SR, Hu ZQ. A coherent polycrystal model for the inverse Hall–Petch relation in nanocrystalline materials. Nanostruct Mater 1999;11:203.

72. Fan GJ, Choo H, Liaw PK, Lavernia EJ. A model for the inverse Hall–Petch relation of nanocrystalline materials. Mater Sci Eng A 2005;409:248.

73. Chattopadhyay PP, Pabi SK, Manna I. On the inverse Hall–Petch relationship in nanocrystalline materials. Z Metall 2000;91:1049.
Koch CC, Narayan J. The inverse Hall–Petch effect – fact or artifact. Mater Res Soc Symp 2001;634:B5.1.1.

74. Kumar KS, Van Swygenhoven H, Suresh S. Mechanical behavior of nanocrystalline metals and alloys. Acta Mater 2003;51:5743.

75. Zhu YT, Langdon TG. Influence of grain size on deformation mechanisms: an extension to nanocrystalline materials. Mater Sci Eng A 2005;409:234.

76. Wolf D, Yamakov V, Phillpot SR, Mukherjee AK, Gleiter H. Deformation of nanocrystalline materials by molecular dynamics simulation: relationship to experiments. Acta Mater 2005;53:1.

77. Meyers MA, Mishra A, Benson DJ. Mechanical properties of nanocrystalline materials. Progr Mater Sci 2006;51:427.

78. J Tru*keV*ich, PC Stevenson, J Hiller, "A study of Nucleation and Growth Processes in the Syndissertation of Colloidal Gold," Discussions of the Faraday Society, 1951;11:55

79. CG Granquist, RA Burhman, Ultraine metal particles, Journal of Applied Physics, 1976:47;2200

80. C Herring JK Galt, "Elastic and Plastic Properties of Very Small Metal Specimens , Physical Review 1952;85:1060

81. RL Mehan, JA Herzog, Mechanical Properties of Whiskers, Whisker Technology, Wiley and Sons, New York, p. 157, 1970.

82. Ino S, "Epitaxial growth of metals on rocksalt faces cleaved in vacuum. II. Orientation and structure of gold particles formed at ultrahigh vacuum," J. Phys Soc. Japan1966;21:346

83. Ino S, Ogawa S, "Multiply twinned particles at earlier stages of gold film formation on alkalihalide crystals," J. Phys. Soc. Japan 1967; 22:1365

84. Yagi K, Takayanagi K, Kobayashi K, Honjo G, "*In-situ* observation of growth processes of multiply twinned particles," J. Crystal Growth 1975;28:117

85. Marks LD, Smith DJ, "High resolution studies of small particles of gold and silver," J. Crystal Growth 1981;54:425

86. Johnson CL, Snoek E, Ezcurdia M, Rodriguez-Gonzales B, Pastoriza-Santos I, Liz-Marzan LM, Hytch MJ, "Effects of elastic anisotropy on strain distributions in decahedral gold nanoparticles," Nature Materials 2008; 7:120

87. Yang CY, “Crystallography of decahedral and icosahedral particles I. Geometry of twinning,” J. Crystal Growth 1979; 47: 274

88. Yang Cy, Yacaman MJ, Heineman K, “Crystallography of decahedral and icosahedral Particles II. High symmetry orientations,” J. Crystal Growth 1979; 47:283

89. Howie A, Marks LD, “Elastic strains and energy balances in multiply twinned particles,” Phil. Mag. A 1984; 49:95

90. V. Volterra: *Ann. Ecole Norm. Super. Paris*, 1907, vol. 24, p. 400.

91. H Ohtsuka, K. Hojou, H. Maeta, H. Sugai, H. Yamamoto, “Radiation defects in nano-structured materials,” Eur. Phys. J. D 2001;16:309.

92. J.D. Nowak, W.M. Mook, A.M. Minor, W.W. Gerberich, C.B. Carter, “Fracturing a nanoparticle, ” Philosophical Magazine 2007;87:29

93. J.R. Greer, W.C. Oliver, W.D. Nix, “Size Dependence of mechanical properties of gold at the micron scale in the absence of strain gradients,” Acta Materialia 2005;53:1821

94. J.R. Greer, W.D. Nix, “Nanoscale gold pillars strengthened through dislocation starvation,” Physical Review B 2006;73:245410

95. D Kiener, C Motz, M Rester, M Jenko, G Dehm, “FIB damage of Cu and possible consequences for miniaturized mechanical tests,” Materials Science and Engineering A 2007;459:262

96. H. Tang, K.W. Scharz, H.D. Espinoza, “Dislocation escape-related size effects in single-crystal micropillars under uniaxial compression,” Acta Materialia 2007;55:1607

97. E. Rabkin, D.J. Srolovitz, “Onset of Plasticity in Gold Nanopillar Compression,” Nanoletters 2007;7:101

98. Zepeda-Ruiz LA, Sadigh B., Biener J., “Mechanical response of Freestanding Au pillars under compression,” Applied Physics Letters 2007;91:101907

99. Hansen N, Ralph B. The strain and grain-size dependence of the flow stress of copper. Acta Metall 1982;30:411.

100. Lu K, Wei WD, Wang JT, “Microhardness and fracture properties of nanocrystalline Ni-P alloy,” Scripta Metallurgica et Materialia 1990;24:2319

101. X Wu, YT Xhu, MW Chen, E Ma, ”Twinning and stacking fault formation during tensile deformation of nanocrystalline Ni,” Scripta Materialia 2006;54:1685

102. Ke M, Hackney SA, Milligan WW, Aifantis EC, “Observation and measurement of grain rotation and plastic strain in nanostructured metal films,” Nanostructured Materials 1995; 5:689

103. R. Mitra, W-A. Chiou, J.R. Weertman, “*In-situ* study of deformation mechanisms in sputtered free-standing nanocrystalline nickel films,” Journal of Materials Research 2004;19:1029

104. A.M.Minor, S.A. Syed Asif, Z. Shan, E.A. Stach, E. Cyrankowski, T.J. Wyrobek, O.L. Warren, “A new view of the onset of plasticity during the nanoindentation of aluminum,” Nature Materials 2006;5:697,

105. J.P. Hirth and J. Lothe, Theory of Dislocations, 2nd ed., John Wiley & Sons, New York, 1982

106. Isrealachvili JN, Intermolecular and Surface Forces: With Applications to Colloidal and Biological Systems, Academic Press, London 1984

107. Robertson IM, Beaudoin A, Al-Fadhalah K, Chun-Ming L, Robach J, Wirth BD, Arsenlis A, Ahn D, Sofronis P, “Dislocation-obstacle interactions: Dynamic experiments to continuum modeling,” Mat. Sci. Eng. A 2005:400-401; 245

108. Al-Fadhalah K, Li C-M, Beaudoin AJ, Korzekwa DA, Robertson IM, "Microplastic processes in pure Ag with mesoscale annealing twins," Acta Mat., 56, 5764, (2008)

109. V Bata E V Pereloma, "An alternative physical explanation of the Hall–Petch relation," 52, 657, (2003)

110. Pan D, Kuwano S, Fujita T, Chem MW, "Ultra-large room-temperature compressive plasticity of a nanocrystalline metal," Nanoletters, 7, 2108, (2007)

111. Siegel RW, Thomas GJ, "Grain boundaries in nanophase materials,"Ultramicroscopy 1992;46:376.

112. Thompson AW, "Yielding in nickel as a function of grain or cell size," Acta Materialia, 23, 1337, (1975)

113. Mehrer H, editor. Diffusion in solid metals and alloys. Series: Landolt-Bornstien: Numerical data and functional relationships in science and technology, Group 3, Condensed matter, vol. 26. Berlin: Springer Verlag; 1990.

114. Gray GT, Lowe TC, Cady CM, Valiev RZ, Aleksandrov IV, "Influence of strain rate and temperature on the mechanical response of ultra-fined grained Cu, Ni and Al–4Cu–0.5Zr," Nanostructured Materials, 9, 477, (1997).

115. Lu L, Li S, Lu K, “An abnormal strain rate effect on tensile behavior in nanocrystalline copper,” Scripta Materialia, 45, 1163, (2001).

116. Dalla Torre F, Van Swygenhoven H, Victoria M, “Nanocrystalline electrodeposited Ni: microstructure and tensile properties,” Acta Materialia, 50, 3957 (2002).

117. Schwaiger R, Moser B, Dao M, Chollacoop N, Suresh S, “Some critical experiments on the strain-rate sensitivity of nanocrystalline nickel,” Acta Materialia, 51, 5159, (2003).

118. Wei Q, Cheng S, Ramesh KT, Ma E, “Effect of nanocrystalline and ultrafine grain sizes on the strain rate sensitivity and activation volume: FCC versus BCC metals,” Mater Science and Engineering A, 318, 71, 2004.

119. May J, Hoppel HW, Goken M, “Strain rate sensitivity of ultrafinegrained aluminum processed by severe plastic deformation,” Scripta Materialia, 53, 189, (2005).

120. Imura T, Ishihara M., “Yield Stress in Silver and Silver-Tin Dilute Alloy Single Crystals,” J. Phys. Soc. Japan, 1997;31:304

VITA

Christopher Earl Carlton was born in Austin, Texas on November 21st 1981, the eldest of two siblings. He attended High School at the Lyndon Baines Johnson Science Academy in Austin were he participated in Varsity sports and earned college credit before graduating in the year 2000. From High School, he entered directly into college, staying in his hometown of Austin to attend the University of Texas. He received his Bachelor of Science (BS) in Mechanical Engineering.

After receiving his BS in Mechanical Engineering, was admitted into the TMI at the University of Texas were he begin seeking a Doctorate of Philosophy (PhD) in Materials Science and Engineering under Dr. Paulo J. Ferreira. He received a Virginia and Ernest Cockrell Jr. Fellowship for his graduate studies. While seeking his PhD at the University of Texas, Christopher received the Materials Research Society silver award in 2007, the Texas Society for Microscopy Materials Division student presentation Award in 2007 and 2008, and the Harris L. Marcus Endowed Graduate Fellowship. During this time he worked as a Teaching Assistant for ME136L Materials Processing Laboratory.

He was recently married to his wife Staci Elaine Podjan last December.

Permanent Address: 4902 Buckskin Pass,
Austin TX, 78745

This dissertation was typed by the author.